STRESS-DRIVEN PATTERN FORMATION IN LIVING AND NON-LIVING MATTER

AMALIE CHRISTENSEN

This thesis has been submitted to the PhD School of The Faculty of Science, University of Copenhagen

Supervisor: Joachim Mathiesen
Niels Bohr Institute
University of Copenhagen

January 2017

ABSTRACT

Spatial pattern formation is abundant in nature and occurs in both living and non-living matter. Familiar examples include sand ripples, river deltas, zebra fur and snail shells. In this thesis, we focus on patterns induced by mechanical stress, and develop continuum theories for three systems undergoing pattern formation on widely different length scales. On the largest scale of several meters, we model columnar jointing of igneous rock. Using analytical calculations and numerical simulations, we derive a scaling function, which quantitatively relates the column diameter to material parameters and cooling conditions. On the scale of micrometers, we model breast cancer tissue as a viscoelastic active fluid. The model captures experimentally observed statistical characteristics as well as the cell division process, and hints at substrate friction being important for cell speed distributions. On the smallest scale of nanometers, we study thin films of block copolymers, which have potential applications as self-organizing templates for microelectronics. By performing a thin-shell expansion of a well-known model for block copolymers, we develop an effective model for the impact of curvature on pattern formation and ordering kinetics in a thin curved film.

RESUME

Naturen er rig på spektakulære mønstre i både levende organismer og ikke-levende materialer. Velkendte eksempler inkluderer sandkrusninger, floddeltaer, zebrapels og sneglehuse.

I denne afhandling, fokuserer vi på mønstre induceret af mekanisk stress og udvikler kontinuumsteorier for tre forskellige systemer, der danner mønstre på vidt forskellige længdeskalaer. På meterskala modellerer vi søjleforkløftninger i magmatiske bjergarter. Ved hjælp af analytiske beregninger og numeriske simulationer udleder vi en skaleringsfunktion, der kvantitativt relaterer søjlediameteren til materialeparametre og kølingsbetingelser.

På mikrometerskala modellerer vi brystkræftcellevæv som en viskoelastisk aktiv væske. Den foreslåede model er i stand til at beskrive de eksperimentelt observerede statistiske karakteristika såvel som celledelingsprocessen. Modellen antyder, at friktionen mellem celler og underlag er vigtig for at kunne beskrive cellernes fartfordeling.

På nanometerskala studerer vi tynde film af blok copolymerer. Disse film har potentiale som selvorganiserende skabeloner for mikroelektronik. Ved at ekspandere en velkendt model for blok copolymerer i filmtykkelsen divideret med den karakteristiske krumningslængde, udleder vi en effektiv to-dimensionel model, der beskriver hvordan filmens krumning influerer mønsterdannelse og dynamikken af defekter.

PUBLICATIONS

[1] Amalie Christensen, Christophe Raufaste, Marek Misztal, Frank Celestini, Maria Guidi, Clive Ellegaard, and Joachim Mathiesen. "Scale selection in columnar jointing: Insights from experiments on cooling stearic acid and numerical simulations." In: *Journal of Geophysical Research: Solid Earth* (2016).

[2] Ann-Katrine Vransøe West, Lena Wullkopf, Amalie Christensen, Natascha Leijnse, Jens Tarp, Joachim Mathiesen, Janine Terra Erler, and Lene Broeng Oddershede. "Dynamics of cancerous tissue correlates with invasiveness." In: *Scientific Reports* (2017).

[3] Amalie Christensen, Ann-Katrine Vransøe West, Lena Wullkopf, Janine Terra Erler, Lene Broeng Oddershede, and Joachim Mathiesen. "Quantifying Cell Motility and Division Processes in Tissue by a Mechanical Continuum Model." In: *Under review in PLOS Computational Biology* (2017).

CONTENTS

1

INTRODUCTION & OBJECTIVES

This thesis covers three largely separate projects concerning the physics of both living and non-living matter on length scales ranging from nanometers for polymers over micrometers for breast cancer cells to several meters for geological systems (Figure 1.1). Though separate, the projects evolve around two common themes: pattern formation and quantitative modeling of experiments.

(a) *Columnar joints [4].* Topic considered in Chapter 2 and publication [1].

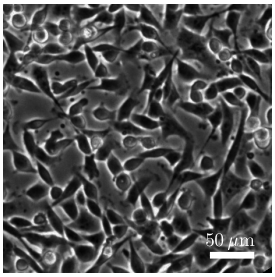

(b) *Cancer cells [5].* Topic considered in Chapter 3 and publications [2, 3].

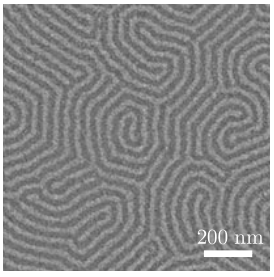

(c) *Block copolymers [6].* Topic considered in Chapter 4. Not yet published.

Figure 1.1: **The topics covered in this PhD thesis** range from length scales of meters for columnar jointing (a) over micrometers for breast cancer cells (b) to nanometers for block copolymers (c).

On the largest scales, we will consider columnar jointing - the spectacular geometric patterns formed during cooling of igneous bodies such as lava lakes (Figure 1.1a). Several outstanding questions exist regarding this almost man-made looking phenomena, but we will focus on how a single length scale, the column diameter, is selected and develop a quantitative model for this selection process. This model will allow us to relate the column diameter to measurable material properties and cooling conditions.

On the scale of micrometers, relevant for human and murine cells, we focus on the collective motion of breast cancer cells (Figure 1.1b). Though chemical signaling pathways are important for cancer cell migration, we focus on the mechanical aspects. Inspired by viscoelastic fluids, we develop a model for cancer cell migration, to understand which features of the cell dynamics can be described by a purely mechanical framework.

On the nanometer scale of block copolymers, we focus on the striped texture formed by phase separation of immiscible blocks (Figure 1.1c). As films of these copolymer textures can be used as templates for e.g.

microelectronics, we are interested in how curvature effectively acts as an ordering field and controls the defect distribution in the resulting patterns. This question is approached using a phenomenological free energy model for block copolymers, and studying the thin film expansion of this model. We note, that the chapter on textures in block copolymers is ongoing work, and does not yet exist in a manuscript form.

All three projects have been approached using continuum field models. Either in the form of classical continuum mechanics or via phenomenological models, where the free energy is expanded in a relevant order parameter. The continuum approach has the advantage of allowing a large number of individual, locally interacting constituents to be considered due to the coarse graining. Furthermore, the continuum approach allows certain analytical calculations to be performed. The developed continuum models were supplemented with numerical implementations to validate the models and to assess how the models behave in regimes that are not analytically accessible.

This thesis is a synopsis and intended as a summary, drawing up the big lines. Many details and calculations are not included in the thesis, but are available in the manuscripts listed under Publications and their appendices. We note, that many figures in this thesis are reproductions of figures in these manuscripts. The thesis is divided into three chapters, each covering a separate research project as visualized by Figure 1.1. Each chapter contains an introduction to the problem, a discussion of the project results and outlines future research directions. Concluding remarks and a general summary are given in Chapter 5.

2

SCALE SELECTION IN COLUMNAR JOINTING

Columnar joints are spectacular geometrical patterns of polygonal fracture networks found across the world, typically in areas with rocks of volcanic origin (Figure 2.1a-2.1c). This almost man-made look of polygonal columns have historically inspired names such as Devil's postpile and Giant's Causeway for columnar jointed sites, but today it is clear that columnar joints are a naturally occurring phenomena.

(a) *Columnar jointing in basalt.* Svartifoss, Iceland. [7]

(b) *Columnar jointing in volcanic tuffs.* Hong Kong area, China. [8]

(c) *Polygonal fracture patterns.* Top view of basaltic columnar joints at Giant's Causeway, Ireland. [4]

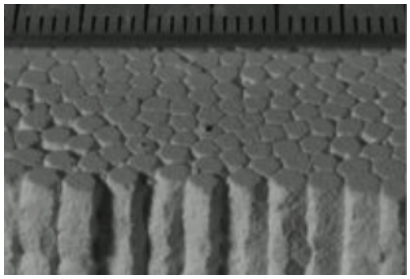

(d) *Columnar jointing in corn starch.* The process is driven by contraction due to dessication, not cooling. [9]

Figure 2.1: **Examples of columnar jointing.** The columns are formed by a fracture network caused by contraction induced stress.

The process of columnar jointing is driven by stress caused by thermal contraction. As an initial uncracked igneous body cools, it also contracts, and any non-uniform contraction will generate stress in the material. For igneous bodies there is a temperature gradient between the hot interior and the cooler surroundings, leading to non-uniform contraction. Igneous rock is in general glassy, and above the glass transition temperature, the rock is able to viscously dissipate the generated stress. However, below the glass transition temperature, stress starts to accumulate, eventually leading to fractures. With time, the glass transition temperature isotherm propagates towards the hot in-

terior of the rock body, dragging with it the front of fractures. As the fracture front propagates, it self-organizes into a mostly hexagonal state, to minimize the fracture surface area created, thus dividing the igneous rock into hexagonal columns (Figure 2.1c). We will consider columnar jointed systems, where the crack front is a plane network propagating normal to the cooling surfaces as in Figure 2.1 and Figure 2.2a. However, columnar jointing also occurs in other geometries, such as approximately ellipsoidal low-volume flows, where the columns will form perpendicular to the cooling surface and the crack front network will be an approximately ellipsoidal surface [10].

In nature, columnar joints are found with diameters ranging between a few centimeters and several meters, with column heights of up to 30 meters. Commonly, the diameter is constant over a significant part of the column height. These regular columns tend to have between 5 and 7 edges, even though columns with between 3 and 8 edges have been observed as well [11–13]. The region of regular columns (termed collonade) can be intersected by a highly disorganized region (termed entablature) as illustrated in Figure 2.2a. The entablature consists of curvy, smaller columns.

Two length scales can be obtained from field studies of columnar joints. The column diameter ℓ and the distance between striation marks s. Striation marks are linear bands running around the columns as illustrated in Figure 2.2b, oriented perpendicular to the crack propagation direction. Striations form by a stepwise crack advance, with each new striation mark indicating one crack advance event. The distance s between two striation marks therefore corresponds to the crack advance length [14].

Several questions regarding columnar jointing remain partially unanswered. The maturation process, leading from the initial hierarchical crack network at a cooling surface dominated by 90 degrees crack intersections, to the hexagonal crack network in the interior of the jointed rock dominated by 120 degrees crack intersections, is for instance not completely understood, though several works on the subject exist [15–18]. It is also not clear, how and under which circumstances entablature is formed. Flooding events have been proposed as the cause [19] but also a dynamical instability of the crack front could be a candidate [20]. How the characteristic length scale of the fracture network, and thus the column diameter is selected, is yet another question.

In Christensen et al. [1] we focused on the selection of a characteristic length scale, and performed a comprehensive study of columnar jointing based on:

1. *A continuum model of columnar jointing*. We showed that the column diameter is a non-trivial function of the material properties and the cooling conditions, and determined this function analytically.

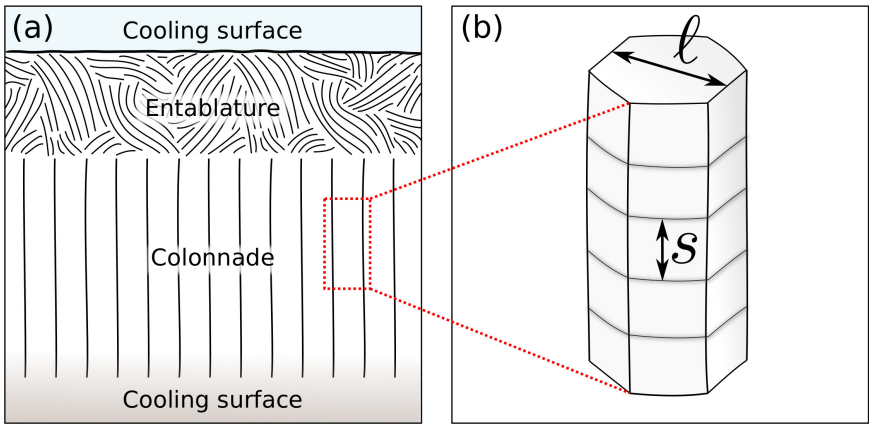

Figure 2.2: **Columnar joint architecture,** and terminology employed in this section. *(a) Sketch of a columnar jointed basalt flow.* The flow is imagined to be cooled by air from the top and by the ground from below. The region termed colonnade consists of polygonal columns with approximately the same diameter. The column diameter ℓ is constant over the height of the colonnade. The entablature is an unstructured region of smaller, curvy columns. *(b) Sketch of a single column.* The crack front dividing the material into columns propagate in incremental steps. The termination of the crack front propagation after each incremental advance leaves striations on the faces of the columns, here indicated by gray lines.

2. *Numerical simulations*. Both discrete element and finite element simulations of columnar jointing were performed.

3. *A novel experimental model system*. We proposed cooling stearic acid as a model system, suitable for lab experiments mimicking igneous columnar jointing.

This chapter will focus on the continuum model for columnar jointing and how the column diameter can be related to material properties and cooling conditions.

2.1 THE INTERNAL STRESS OF THE COOLING MATERIAL

As columnar joints are caused by fracturing, a key quantity in describing columnar jointing is the internal stress of the material generated by the material's anisotropic contraction upon cooling. In a linear approximation, the internal stress will be proportional to $E\beta/(1-\nu_{pois})$, where E is the Young modulus, $\beta = \alpha_T \Delta T$ the contraction, α_T the coefficient of linear thermal expansion, ΔT a temperature change and ν_{pois} the Poisson ratio.

If the contraction of the material β happens over a length scale w, then the internal stress vanishes in the limit of large w and increases

as the width w decreases. The magnitude of the internal stress σ can therefore be written in terms of a scaling function f:

$$\sigma = E\beta\, f(w, \nu_{pois}, \ldots), \tag{2.1}$$

where the scaling function f might further depend on cooling conditions or material properties such as thermal diffusivity and fracture toughness.

The scaling function approach is inspired by work on mud and dessicating thin films, where analytical expressions for the scaling function have been derived [21]. An asymptotic shape of the scaling function for columnar jointing in Eq. 2.1 has been suggested in [22]. Here, we determine the dependencies and shape of the scaling function f aided by simple analytical models, numerical simulations and experiments on cooling stearic acid.

2.1.1 *The contraction length scale*

The length scale w, over which the material experiences the contraction β, is governed by the heat transport in the material. In the literature, two main modes of heat transport have been considered: bulk heat conduction and crack-aided convective cooling.

Heat conduction through the bulk of the material is a diffusive process controlled by the thermal diffusivity D. In an infinite medium, the only natural length scale of the temperature distribution is therefore $w \sim \sqrt{Dt}$. This is the length scale over which temperature changes and thus contraction occur, and this length scale increases with time (Figure 2.3a). Taking the latent heat, released during solidification, into account does not change this picture (Appendix A.1).

Crack-aided convective cooling on the other hand, assumes that water and steam perform a convection cycle in the crack network, efficiently extracting heat from the hot interior, resulting in a cold zone of $T = 100\,^{\circ}C$ propagating through the material at a constant speed v. This moving boundary condition in an otherwise purely heat conducting material, leads to a temperature distribution with a fixed shape, propagating at speed v with a characteristic length scale of temperature change $w \sim D/v$, which is constant in time (Figure 2.3b).

The dominance of the crack-aided convective cooling mechanism is supported by borehole measurements of the Kilauea Iki lava lake [23], where the temperature profile of the cooling lava lake was measured over a year. In the top 40 m, closest to the cooling surface of air, a uniformly 100°C cold zone was found, and this zone propagated at a constant speed towards the interior of the lava lake. The spatial shape of the measured temperature profile was in agreement, with the convective cooling picture.

Furthermore, the crack-aided convective cooling mechanism is compatible with the observation, that the column diameter and the stria-

tion width of basaltic columnar joints are typically constant over most of the column height [12, 24, 25]. If conductive cooling dominated, one would instead have expected the column diameter and the striation width to increase with the distance from the cooling surface, due to the increase of the contraction length scale w.

In modeling the cooling and subsequent cracking of the material, we will therefore employ the temperature distribution resulting from crack-aided convective cooling.

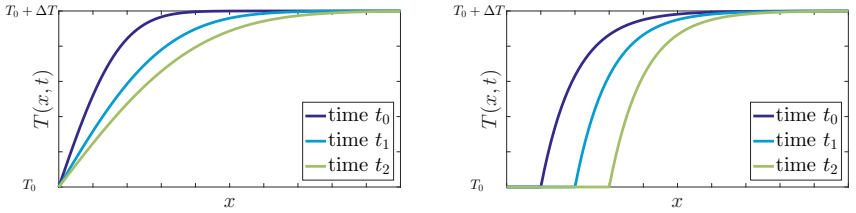

(a) *Conductive cooling.* Temperature evolution governed by: $T(x,t) = T_0 + \Delta T \operatorname{erf}\left(\frac{x}{2\sqrt{Dt}}\right)$

(b) *Convective cooling.* Temperature evolution governed by: $T(x,t) = T_0 + \Delta T\left(1 - e^{-v/D(x-vt)}\right)\theta(x-vt)$

Figure 2.3: **Heat transfer modes in columnar jointing.** In a conductively cooled system, the width of the temperature profile $w = \sqrt{Dt}$ increases with time as illustrated in Figure 2.3a. For a convectively cooled system, the temperature profile width is fixed $w = D/v$ and the profile moves with a constant speed v and fixed shape, see Figure 2.3b. Both systems are subject to the boundary condition $T(\infty, t) = T_0 + \Delta T$, where T_0 is the temperature of the cooling surface, e.g. air, and $T_0 + \Delta T$ is the temperature of the molten interior. The system in (a) is subject to $T(0, t) = T_0$ whereas the system in (b) is subject to $T(x < vt, t) = T_0$.

2.1.2 *The column diameter*

The diameter of the columns ℓ in the convectionally cooled regime is widely considered to be governed by the temperature profile speed v, which is proportional to the rate of cooling [16, 26], though alternative mechanisms have been suggested [27–29].

Faster cooling leads to slenderer columns, as the heat transferred from the hot interior to the fracture network per time must equal the cooling rate. Assuming that 1 m of crack is only capable of transferring a fixed amount of heat per time, then the length of the crack network would have to increase, if the cooling rate increased, and thus the column diameter would decrease [16], see Figure 2.4. Also the geological setting (lava flow, lava lake, lava dome, sill, and dyke) has been found to influence the column diameter, through control of the surfaces where heat can be exchanged with the environment, and thus influencing the cooling rate [11].

Whether there is a one-to-one correspondence between the column diameter ℓ on one hand, and the material properties (such as E, α_T, D and fracture toughness $K_{I,c}$) and cooling parameters (such as $\Delta T, w$) on the other hand, is to the best of our knowledge still uncertain. A one-to-one correspondence is frequently assumed in the literature [26, 30, 31], but one might alternatively operate with a range of possible column diameters for each set of material and cooling parameters, as observed in experiments on dessicating corn starch [32]. In this work, we will therefore explore the idea of a range of possible column diameters.

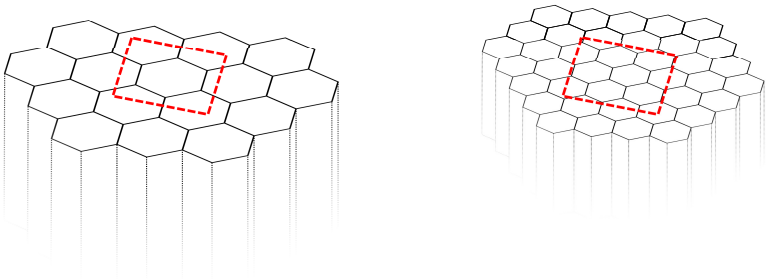

(a) Low cooling rate fracture network. (b) High cooling rate fracture network

Figure 2.4: **Cooling rate and column diameter.** The length of the fracture network increases with increasing cooling rate. This is seen by comparing the length of the fracture network within the red box in Figure 2.4a and 2.4b. As the fracture network length increases, the column diameter decreases.

2.2 A CONTINUUM MODEL OF COLUMNAR JOINTING

Our starting point is the idealized version of a system undergoing columnar jointing shown in Figure 2.5a. Here, we have considered all columns to be perfectly hexagonal, though real igneous columnar jointed rock commonly shows columns with five or seven edges. We have furthermore assumed the system to be of infinite extend, which is a reasonable simplification since the characteristic length scale of the columns, their diameter ℓ, is typically much smaller than the extend of the columnar jointed region.

We will further simplify the problem by performing a plane cut through the red dashed line of the three-dimensional model, and considering the resulting array of semi-infinite cracks shown in Figure 2.5b. In reality, columnar joints are neither perfectly hexagonal nor two-dimensional, and the validity of the two-dimensional model thus ultimately relies on its agreement with three-dimensional numerical simulations.

We consider the heat transfer mechanism to be crack-aided convective cooling, and in the frame (X, Y, Z) moving with the convection

zone at speed v, the two-dimensional strip is subject to the temperature distribution:

$$T_{w,a}(X) = \Delta T \left(1 - e^{-(X+a)/w}\right) \theta(X+a) - \Delta T, \tag{2.2}$$

where ΔT is the maximal temperature difference with respect to the undeformed state, a is the signed distance between the temperature front and the crack tips, $w = D/v$ is the length scale over which temperature changes occur, $b = \ell/2$ is half the column diameter, and $\theta(X)$ is the Heaviside step function. We define the dimensionless moving frame coordinates x, y and the dimensionless control parameters δ, Pe:

$$x = \frac{X}{b}, \qquad y = \frac{Y}{b}, \qquad \delta = \frac{a}{b}, \qquad Pe = \frac{v}{D/\ell} = \frac{\ell}{w} = \frac{2b}{w}. \tag{2.3}$$

For later convenience, we have rescaled with half the column diameter b. The Péclet number Pe is the ratio of the heat advection and heat diffusion rates $Pe = v/(D/\ell)$, but in the case of columnar jointing, it can also be though of as the ratio between the column diameter and the width of the thermal front $Pe = \ell/w$. The dimensionless temperature profile becomes:

$$T_{Pe,\delta}(x) = \frac{T_{w,a}(X)}{\Delta T} = \left(1 - e^{-(x+\delta)Pe/2}\right) \theta(x+\delta) - 1. \tag{2.4}$$

We take the model material to be linearly elastic and the two-dimensional strip to be under plane stress conditions. As the speed of sound in basalt is of the order 10^3 m/s [33], whereas the speed of the temperature front is of the order 10^{-8} m/s [23] it is reasonable to assume, that the changes in thermal fluxes happen on a time scale much larger than the time needed to reach elastostatic equilibrium. The crack front thus merely follows the temperature profile and propagates continuously at a speed v through the material.

2.2.1 *Relating column width and system parameters*

To be able to relate the column diameter ℓ to material properties and cooling parameters, we need to calculate the mode I stress intensity factor K_I of the crack tips in the linear elastic strip. Since the cracks propagate straight, the mode II stress intensity factor K_{II} is zero. We performed the calculation using the Wiener-Hopf method along the lines of Marder [34]. The calculations are available in [1] and the result for the dimensionless mode I stress intensity factor κ_I:

$$\kappa_I(Pe, \delta) = \frac{K_I}{E\alpha_T \Delta T \sqrt{b}} \tag{2.5}$$

is displayed in Figure 2.6. In igneous columnar jointing, fracturing occurs incrementally, leaving striations. However, we will not model

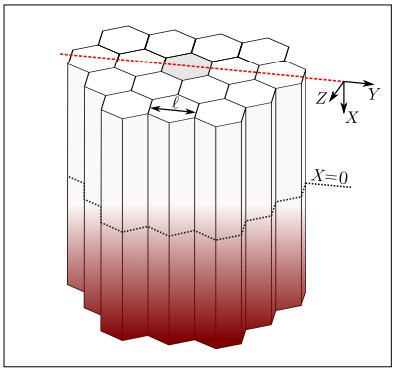

(a) *Idealized 3D system.* Infinite array of perfectly hexagonal columns with diameter $\ell = 2b$. The columns extend over $X \in \{-\infty; 0\}$ and the uncracked material extends over $X \in \{0; \infty\}$. The front of crack tips is indicated with a black dashed line and is located at $X = 0$.

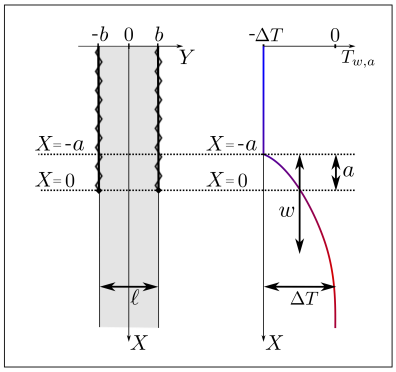

(b) *Idealized 2D model.* The gray strip results from a vertical cut along the red dashed line in Figure 2.5a. We only need to consider one column, since the 2D plane cut is periodic in the y-direction. The semi-infinite cracks are indicated with zigzag lines and extend over $X \in \{-\infty; 0\}$.

Figure 2.5: **Columnar jointing model.** The system in Figure 2.5a is subject to a temperature field $T_{w,a}(X)$, which varies only in the X-direction. Red indicates hot regions and white indicates colder regions. We emphasize that the coordinate system (X, Y, Z) is moving at speed v with the convection zone. It is only in this moving frame, that the temperature front has a constant shape. The gray strip in Figure 2.5b results from a vertical cut along the red dashed line in Figure 2.5a and is infinite in the X-direction and periodic in the Y-direction with $Y = +b$ equal to $Y = -b$. The strip is subject to the temperature profile $T_{w,a}(X)$ in Eq. 2.2. The figure text is adapted from Christensen et al. [1].

the striation process, but consider the crack propagation to be continuous, such that the fracture criterion:

$$\kappa_I(Pe, \delta) = \kappa_{I,c} \tag{2.6}$$

is always fulfilled at the crack tips. Here, $\kappa_{I,c} = K_{I,c}/(E\alpha_T \Delta T\sqrt{b})$ is the dimensionless fracture toughness (the critical mode I stress intensity factor). We note, that the dimensionless fracture toughness can be expressed in terms of half the column width b and a mechanical loading length b_{min}:

$$\kappa_{I,c} = \sqrt{\frac{b_{min}}{b}} \qquad b_{min} = \left(\frac{K_{I,c}}{E\alpha_T \Delta T}\right)^2 \tag{2.7}$$

In case of a uniform thermal contraction, the Péclet number is zero and the stress intensity factor reaches its maximal value $\kappa_I(0, \delta) = 1$ independent of δ, see Figure 2.6. For fracturing to occur, we must thus have $\kappa_{I,c} = 1$, leading to $b = b_{min}$ and the column diameter being equal to twice the mechanical loading length $\ell = 2b_{min}$. This

is the minimum column diameter possible - any other temperature profile will lead to smaller values of κ_I and thus larger values of b (see Figure 2.6).

Let us assume, that we fix the material properties and the temperature profile, i.e. we keep b_{min} and w fixed. What are the possible column diameters $\ell = 2b$ of this configuration? The fracture criterion in Eq. 2.6 can be fulfilled for any column width:

$$b \geqslant b_{min}, \tag{2.8}$$

if the crack tip position $\delta = a/b$ is changed accordingly, thus adjusting $\kappa_I(Pe, \delta)$ in the interval $[0, 1]$. A continuous set of (Pe, δ) values is therefore possible for each set of material properties and cooling conditions, and the physical mechanism behind this can be thought of as follows: imagine that the fracture spacing, and thus the Péclet number, is increased slightly. The resulting fracture density then decreases, and the stress intensity at the crack tips will increase in turn. To bring the stress intensity level at the crack tips back to the critical value, the crack tips can move further into the hot uncontracted region by increasing δ.

2.2.2 *A one-to-one relation?*

The two-dimensional linear elastic model does allow a range of column diameters to occur for each set of system parameters. To test whether this is the relevant case, or a one-to-one relation better describes columnar jointing, we performed a set of discrete element simulations, see Section A.2.1 for details.

In the simulations, a temperature profile with the shape given by Eq. 2.2 propagated through a three-dimensional network of connected springs. The springs' equilibrium length changes with the temperature and they can break when a critical stress or strain is reached. An example of the resulting fracture network is shown in Figure 2.7. In the simulations, the fracture toughness $\kappa_{I,c}$ and the temperature front width w are fixed. The resulting diameter of the columns $\langle \ell \rangle$ and the distance between the crack tips and the temperature front $\langle a \rangle$ are then measured, when the system has reached a state where the crack front propagates steadily with a constant column diameter. From the measured column diameter and the temperature front width, a Péclet number of the simulation can be determined $Pe = \langle \ell \rangle / w$.

To assess whether a range of column diameters do occur, we performed simulations, where the temperature front width w was suddenly increased/decreased for otherwise fixed parameters. The column diameter was observed to increase/decrease correspondingly, such that the Péclet number stayed approximately constant. In the case, where all column diameters $b \geqslant b_{min}$ were equally possible, we would instead have expected to see cases where the column diameter

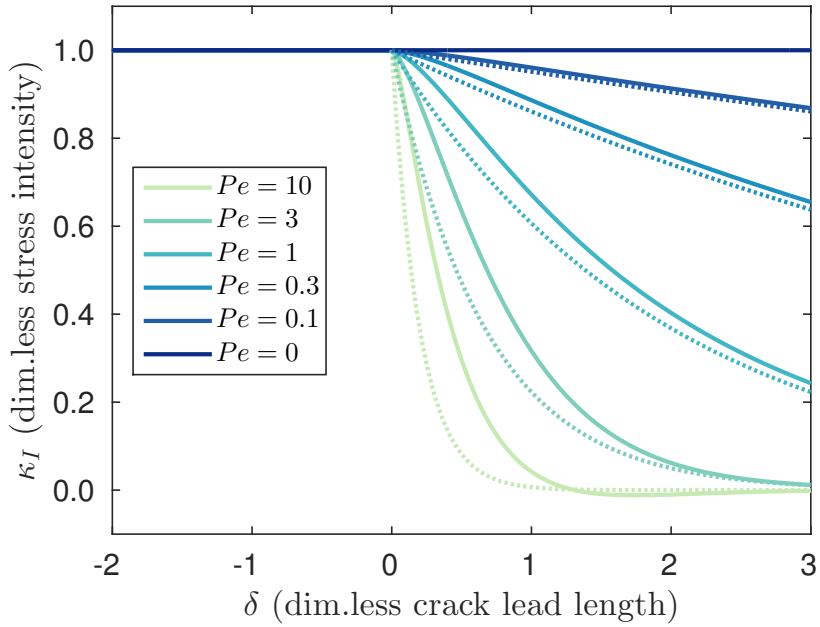

Figure 2.6: **The dimensionless mode-I stress intensity factor,** κ_I, as a function of the distance between the temperature front and the crack tips, $\delta = a/b$, for different Péclet numbers, $Pe = 2b/w$. Solid lines represent the analytical solution for $\kappa_I(Pe, \delta)$. For small Péclet numbers, the analytical solution coincides with the negative of the temperature profile $-T_{Pe,\delta}(x = 0)$ represented by dashed lines. This can be understood by noting, that for small Péclet numbers, the temperature gradient is small (i.e. the temperature front width w is large) and a crack tip located at $x = 0$, a distance δ ahead of the temperature profile, experiences an essentially uniform contraction, which in dimensionless form will be equal to $-T_{Pe,\delta}(x = 0)$. We note, that the value $\kappa_I = 1$ corresponds to the stress intensity factor for a uniform temperature field ($Pe = 0$). When the Péclet number increases, the temperature gradient kicks in, and the analytical solution deviates more and more from the negative of the temperature field.

remained constant but the distance a between the crack tips and the temperature profile changed. The simulated systems instead picked out one column diameter ℓ for each choice of the temperature profile width w, leading to a constant Péclet number and a one-to-one correspondence between the Péclet number Pe and the fracture toughness $\kappa_{I,c}$. Even though the simulations strongly suggest a one-to-one correspondence, a narrow range of allowed Péclet numbers can not be completely ruled out.

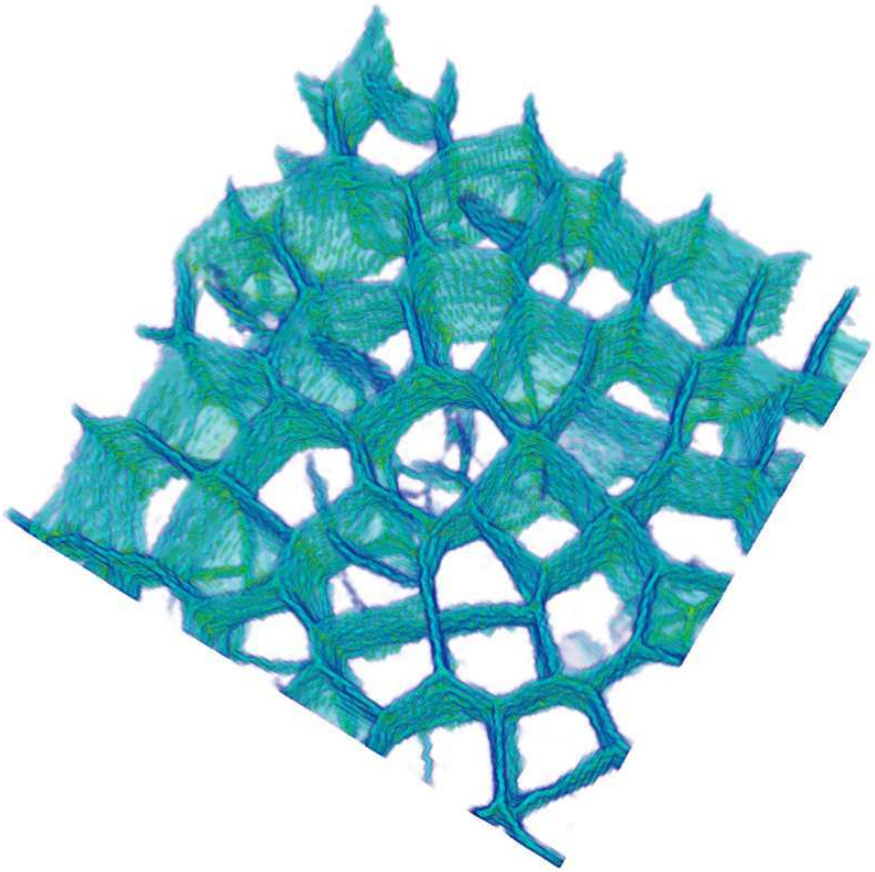

Figure 2.7: **Example of a discrete element simulation of columnar jointing.** The figure shows the broken bonds in a typical discrete element simulation. The polygonal geometry of the fracture network is clearly visible. The simulations as well as the scheme for extracting pairs of $(Pe, \kappa_{I,c})$ are described in Appendix A.2.1. Simulations similar to the depicted one, were carried out in two dimensions to produce Figure 2.8.

2.2.3 *The scaling function*

The one-to-one relation between the Péclet number and the fracture toughness combined with the fracture criteria in Eq. 2.6 imply, that the crack lead length δ must also be a function of the Péclet number $\delta = g(Pe)$.

To determine the function $g(Pe)$, we performed two-dimensional discrete element simulations. As in the three-dimensional simulations, the column diameter $\langle \ell \rangle$ and the distance between the crack tips and the temperature front $\langle a \rangle$ were measured, whereas the temperature front width w and the fracture toughness $\kappa_{I,c}$ were simulation parameters. The two-dimensional simulation results in Figure 2.8 indicate

that the relation between the Péclet number and the crack lead length is a power law:

$$\delta = g(Pe) = c_1 \, Pe^{c_2}, \tag{2.9}$$

where we propose the coefficients $c_1 = 5.4$ and $c_2 = -1.4$. The error-bars are large, but this choice of coefficients is in agreement with the data in Figure 2.8 and furthermore yields a best fit between the fracture toughness and the measured Péclet number in the three-dimensional simulations, see Figure 2.9.

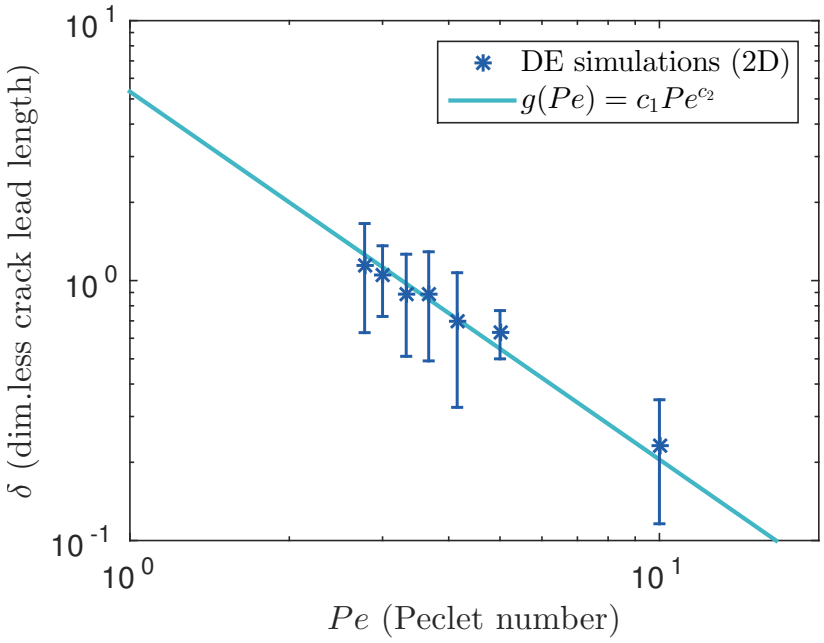

Figure 2.8: **Crack lead length is a function of the Péclet number.** Discrete element simulations were performed in two dimensions and the average column diameter, $\langle \ell \rangle$, as well as the average crack lead length, $\langle a \rangle$, were measured. We observe a power law relation between the Péclet number, $Pe = \langle \ell \rangle / w$, and the crack lead length, $\delta = \langle a \rangle / (\langle \ell \rangle / 2)$. The plotted power law is given by $\delta = g(Pe) = c_1 \, Pe^{c_2}$ with $c_1 = 5.4$ and $c_2 = -1.4$. Figure text adapted from Christensen et al. [1].

With the crack lead length expressed as a function of the Péclet number (Eq. 2.9), we are now in a position to analytically determine the one-to-one relation between the Péclet number Pe and the fracture toughness $K_{I,c}$. Substituting Eq. 2.9 in the fracture criterion in Eq. 2.6 yields:

$$K_{I,c} = K_I(Pe, g(Pe)) = f(Pe), \tag{2.10}$$

where we have defined the scaling function $f(Pe) = K_I(Pe, g(Pe))$. The scaling function predicts, that the column diameter ℓ is a func-

tion of both the material properties ($E, \alpha_T, D, K_{I,c}$) and of the cooling conditions parametrized by ($\Delta T, v$).

The scaling function is in excellent agreement with the results of the three-dimensional discrete element simulations, see Figure 2.9. A few finite element simulations (Section A.2.2) were performed to check the validity of the discrete element scheme, and they also showed excellent agreement with both the scaling function and the discrete element simulations. The scaling function furthermore agrees reasonably well with our experimental measurements of cooling stearic acid and with field measurements from the Kilauea Iki lava lake [23]. To the best of our knowledge, the Kilauea Ikia lava lake field study is the only published direct measurement of the thermal front speed v.

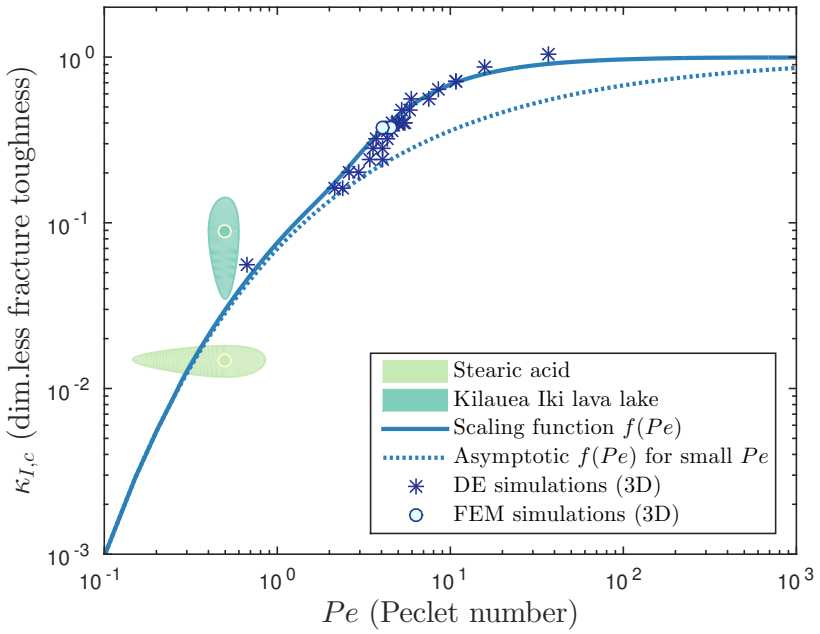

Figure 2.9: **Columnar jointing scaling function.** The analytically derived scaling function $f(Pe)$ excellently describes the three-dimensional discrete element (DE) simulations. To check the validity of the DE scheme, a few finite element (FEM) simulations of columnar jointing were run. The FEM simulations correspond closely to the DE simulations. The scaling function agrees reasonably well with estimates for the Kilauea Iki lava lake, where the velocity of the temperature front was measured directly, as well as with the stearic acid experiments reported in Christensen et al. [1]. We note, that Figure 2.6 showed, that for small Péclet numbers, the dimensionless stress intensity factor $\kappa_{I,c}$ approaches $-T_{Pe,\delta}(x = 0)$. The asymptotic behavior of the scaling function is therefore $f(Pe) \to -T_{Pe,g(Pe)}(x = 0)$ for small Péclet numbers.

The relation between the scaling function and the dimensionless fracture toughness in Eq. 2.10 allows us to estimate the temperature

front propagation speed v from field measurements of the column diameter $\ell = 2b$, the emplacement temperature and material properties. This is concretely done, by first calculating the dimensionless fracture toughness $\kappa_{I,c} = K_{I,c}/(E\alpha_T \Delta T\sqrt{b})$. The scaling function can then be used to estimate the relevant Péclet number from $\kappa_{I,c}$. When the Péclet number is known, the temperature front speed can be found as $v = Pe(D/\ell)$.

Figure 2.10 shows the prediction of the temperature front speed v, calculated using the scaling function and field measurements of the column diameter. The data cover sites in the Columbia River Basalt Group and are available from Goehring and Morris [25]. The figure also displays the temperature front speed, as estimated by [25] from measurements of striae heights at the same sites. Our model systematically predict values of the speed a factor of about two lower than the estimates based on striae heights. However, keeping in mind that the two estimates are based on independent field data and different models, the estimates are close.

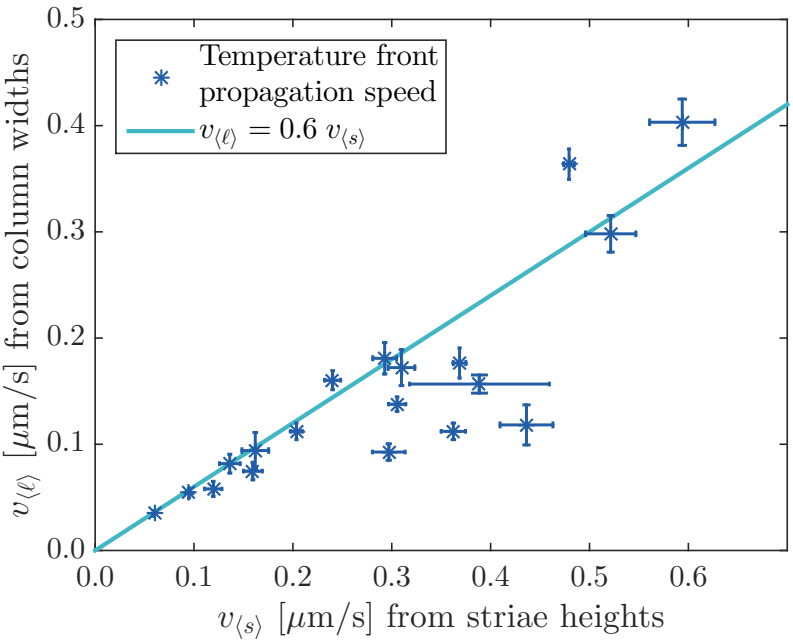

Figure 2.10: **Estimates of the cooling rate from field measurements.** The temperature front propagation speed, $v = Pe\,(D/\ell)$, is estimated for different field locations using two different methods requiring different input measurements: column diameter, $\langle \ell \rangle$, and striae height, $\langle s \rangle$, respectively. The speeds on the vertical axis are calculated using the scaling function $Pe = f^{-1}(\kappa_{I,c})$, and field measurements of the average column diameter $\langle \ell \rangle$ from [25]. The speeds on the horizontal axis are calculated on the basis of field measurements of striae heights $\langle s \rangle$ at the same sites following [35]. Each point represents one field location. Figure text adapted from Christensen et al. [1].

2.3 DISCUSSION

In this work, we argued that the process of columnar jointing selects one Péclet number for each dimensionless critical stress intensity factor. We determined the functional form of this relationship based on analytical calculations and numerical simulations, and found it to be in reasonable agreement with experiments on stearic acid, geological field data and three-dimensional numerical simulations. The scaling function, relating the Péclet number and the dimensionless critical stress intensity factor, can be used to estimate the velocity by which the fracture front, and thus the cooling front, propagated through the system, when basic properties of the rock, the emplacement temperature and the column diameter are known.

Though our simulations in two- and three dimensions indicated a one-to-one correspondence between the Péclet number and the dimensionless stress intensity factor, a narrow finite range of allowed Péclet numbers can not be ruled out. The model system of cooling stearic acid, could be used to experimentally clarify how well the one-to-one correspondence holds, if better control of the temperature evolution is gained.

The model system of cooling stearic acid, has the great advantage of tractable sizes and temperatures as well as being an affordable harmless substance. It furthermore relies on thermal contraction, and not contraction caused by dessication, as the often studied starch system. Aside from testing the one-to-one relation, the stearic acid model system could be used to investigate entablature formation as well as the effect of an initial surface crack pattern.

3

COLLECTIVE DYNAMICS AND DIVISION PROCESSES IN TISSUE

Schools of fish, flocking birds and dense bacterial suspensions are examples of active matter, composed of a large number of self-driven units (Figure 3.1). As energy is constantly introduced at the local scale of each constituent unit, these systems are continuously driven out of equilibrium. This local injection of energy distinguishes active matter from traditional non-equilibrium systems, where external driving such as an applied stress pushes the system out of equilibrium [36, 37].

Collective behavior, such as flocking and pattern formation on the length scale of several constituent units, is observed in active matter and is driven by the local interaction of the constituent units with each other and with the surrounding medium. Also turbulent-like states, characterized by flow vortices and the continuous creation of swirls and velocity jets, have been observed in active matter such as bacteria suspensions [38–40] and cell mono-layers [41].

Epithelial tissue, which is the main topic of this chapter, can be characterized as active matter. Individual living cells constitute the self-driven units and intra-cellular junctions allow for interaction between units.

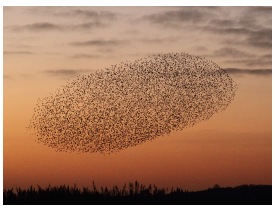

(a) *Flocking birds.* Starling murmuration at Minsmere, Suffolk. [42]

(b) *School of fish.* Barracudas at Sanganeb Reef, Sudan. [43]

(c) *Bacterial suspension.* A myxobacterial flock. [44]

Figure 3.1: Examples of living active matter.

Epithelial cells line cavities in the human body such as the mouth and lungs and cover surfaces such as the skin. The epithelial cells' ability to form tight layers is vital for their function as protection and mechanical support for the enclosed tissue and is achieved mainly through the tight cell-cell junctions. The strong inter cellular interactions support collective cell behavior such as wound closure, where long range velocity correlations and collective migration are observed [45]. Also long range vortex patterns around cell division sites [46] and mechanical waves have been observed in epithelial tissues [47].

CELL LINE	TYPE	ORIGIN	NOTE
67NR	Epithelial	Murine	Cancerous, non-invasive
4T1	Epithelial	Murine	Cancerous, invasive
MCF7	Epithelial	Human	Cancerous, non-invasive
MDA-MB-231	Epithelial	Human	Cancerous, invasive
HUVEC	Endothelial	Human	Not cancerous

Table 3.1: The proposed model is compared to experiments on confluent mono layers of the above five cell lines. Experimental sample pictures are depicted in Figure 3.2 and experimental details can be found in Appendix B.1. The experimental data on epithelial cells were published in West et al. [2] and the data on endothelial cells in Rossen et al. [46].

Epithelial cells play a key role in cancer development, as most cancerous tissues take the form of carcinomas of epithelial origin [48]. Invasion into healthy tissue is a hallmark of aggressive cancer, and cancer cells have been observed to migrate both as single cells and collectively in groups or sheets [49]. Many important signaling pathways controlling cancer cell migration have been identified [50], but also mechanical cues might play a role, as mechanical forces can be transmitted over large distances in tissue [51] and cells have been observed to migrate in the direction of minimal shear stress [52].

In our work [2, 3], we focus on the mechanical aspect of cancer tissue dynamics, and try to understand which features of the cell dynamics, can be described by a purely mechanical framework, when the tissue is regarded as an active material.

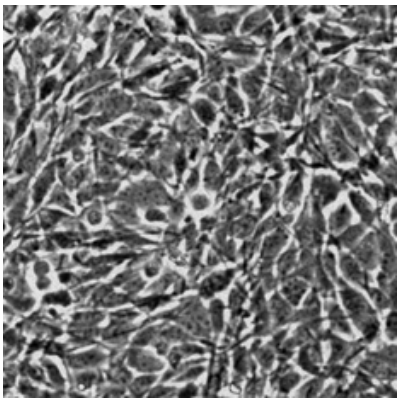

(a) *Murine non-invasive* breast cancer. Epithelial 67NR cells. The window is 300×300 µm.

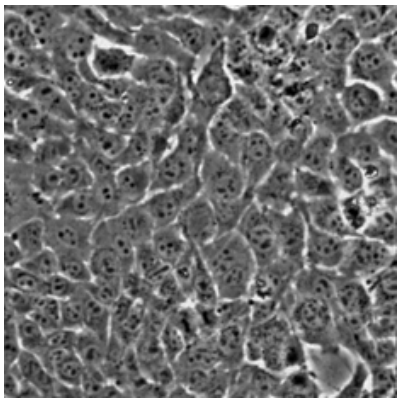

(b) *Murine invasive* breast cancer. Epithelial 4T1 cells. The window is 300×300 µm.

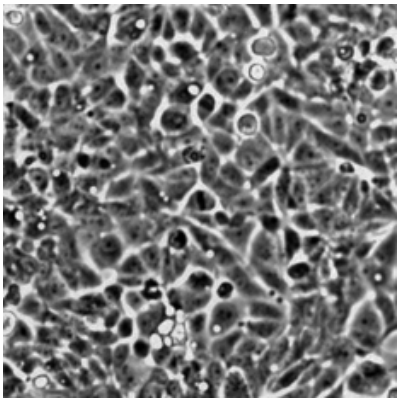

(c) *Human non-invasive* breast cancer. Epithelial MCF7 cells. The window is 300×300 µm.

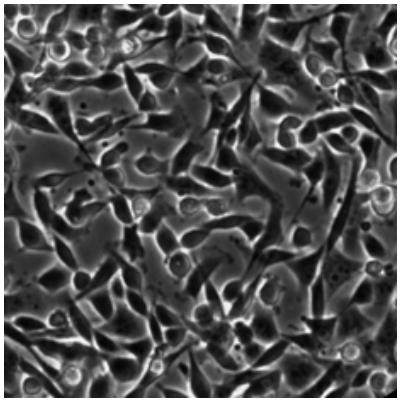

(d) *Human invasive* breast cancer. Epithelial MDA-MB-231 cells. The window is 300×300 µm.

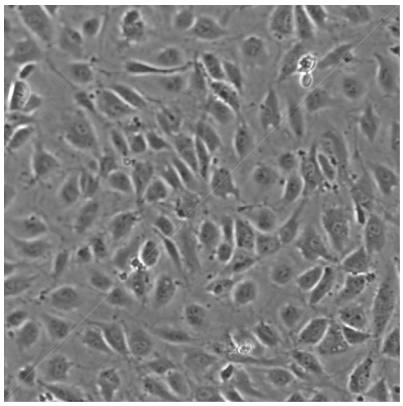

(e) *Human endothelial cells.* Endothelial umbilical vein HUVEC cells. The window is 600×600 µm.

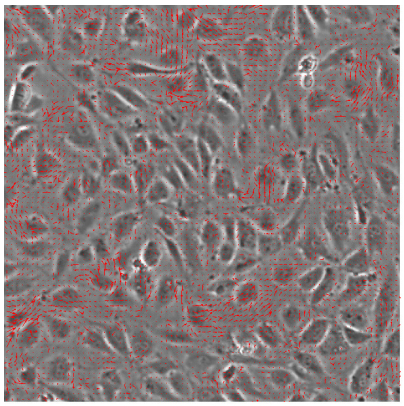

(f) *Human endothelial cells.* Velocity field of Figure 3.2e obtained from PIV analysis.

Figure 3.2: **Sample of experimental data.** Phase-contrast microscopy pictures of confluent cell monolayers. The cancerous epithelial cells in Figure 3.2a-3.2d are the main focus of this section, and has a characteristic size of 20 µm. The non-cancerous endothelial cells in Figure 3.2e-3.2f are included for comparison, and has a characteristic size of 40 µm. The experiments are described in Appendix B.1.

3.1 A CONTINUUM MODEL FOR COLLECTIVE MOTION OF CELLS

We formulate the model in terms of the local mean velocity field $\mathbf{v}$ of the active material. This readily allows for comparison with experiments, where confluent mono layers of cells are grown and the velocity fields extracted by Particle Image Velocimetry (PIV). We will compare the model to experiments on four types of cancerous epithelial cells, see Table 3.1. Also a single line of non-cancerous endothelial cells, which line blood and lymphatic vessels in animals, will be considered for completeness. Experimental details are given in Appendix B.1.

The active material is assumed to obey momentum conservation and to be incompressible ($\nabla \cdot \mathbf{v} = 0$), such that the projected area of each cell is conserved. For tissue, viscous dissipation and frictional damping completely dominate over inertial forces, and momentum conservation takes the form:

$$0 = -\frac{1}{\rho}\nabla p + \frac{1}{\rho}\nabla \cdot \sigma + \mathbf{f} + \mathbf{m}, \tag{3.1}$$

where ρ is density, p is pressure, σ is the deviatoric stress tensor, $\mathbf{f}$ is the cell-substrate friction force and $\mathbf{m}$ represents the motility force generated by the self propulsion of the cells. The key ingredients of the model are the *rheology, friction* and *motility*:

RHEOLOGY: Both individual cells [53, 54] and tissues [55–59] have been observed to respond viscoelastically when subject to mechanical stimuli. I.e. on short time scales, the material deforms elastically, whereas long time mechanical loading results in viscous flow and thus permanent deformation. On the time scale of the considered experiments (several hours), the tissue experiences permanent deformation, as the considered cells have a typical speed of 1 μm/min and a cell size of 20 μm. The tissue is therefore best described by a fluid-like rheology.

One of the simplest fluid-like viscoelastic rheologies is the Oldroyd-B model:

$$\sigma + \lambda_1 \overset{\nabla}{\sigma} = 2\eta_0 \left(\gamma + \lambda_2 \overset{\nabla}{\gamma}\right), \tag{3.2}$$

where $\gamma = \frac{1}{2}(\nabla\mathbf{v} + (\nabla\mathbf{v})^T)$ is the strain rate tensor and $\overset{\nabla}{\sigma}, \overset{\nabla}{\gamma}$ are the upper convected derivatives (see Section B.2-B.3) of the stress and the strain rate respectively. The Oldroyd-B model can be thought of as the result of dissolving a Maxwell fluid in a Newtonian solvent (Figure 3.3). A pure Maxwell fluid would have been the simplest possible rheology, but as the Maxwell fluid does not capture the observed flow fields during cell division, the Oldroyd-B model is used.

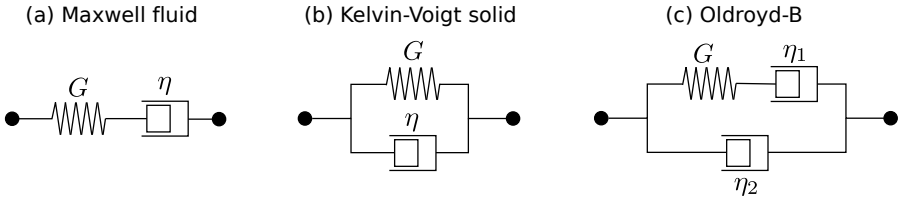

Figure 3.3: **Rheological diagrams.** Constitutive equations can be visualized as rheological diagrams, where elastic springs (denoted by their elastic modulus G) and viscous dash pots (denoted by their viscosity η) are coupled together. Stress of elements coupled in parallel add up. The same is true for strains in series. *(a) Maxwell fluid.* Under sudden stress, the spring deforms instantaneously whereas the dash pot deforms at a constant rate like a fluid. When the Maxwell element is released, the spring regains its original length, but irreversible deformation has happened due to the dash pot. The Maxwell element is thus the simplest possible fluid-like rheology. *(b) Kelvin-Voigt solid.* Under sudden stress, the Kelvin-Voigt solid deforms with a characteristic time scale η/G. The deformation is reversible and when released, the Kelvin-Voigt solid regains its original shape. The Kelvin-Voigt element is thus the simplest possible solid-like rheology. *(c) Oldroyd-B fluid.* This rheology can be viewed as a Maxwell fluid described by (G, η_1) dissolved in a Newtonian fluid of viscosity η_2. When subject to a sudden strain ϵ_0, the stress decays exponentially with a timescale η_1/G towards zero.

FRICTION: In the literature on cell continuum models, the cell-substrate friction $\mathbf{f}$ has commonly been represented by a Stokesian drag-like term linear in the velocity [60–65]:

$$\mathbf{f}_{\text{drag}} = -\alpha_{\text{drag}}\mathbf{v}.$$

However, this drag term is incapable of reproducing the exponential tails of the speed distributions observed in the experiments (see Figure 3.5a).

By considering simple stochastic processes we motivated [3], that the simplest possible term reproducing the exponential tails is reminiscent of dry Coulomb friction:

$$\mathbf{f} = -\alpha\hat{\mathbf{v}}, \tag{3.3}$$

where $\hat{\mathbf{v}} = \mathbf{v}/|\mathbf{v}|$ is the direction of the velocity. From a microscopic point of view, the friction term can be thought of as resulting from the breaking of cell-substrate contacts during motion. If the energy associated with breaking/establishing a contact is independent of the cell velocity, and the density of contacts between cell and substrate is assumed constant, then the energy spent as the cell moves along will only depend on the distance moved - not on the velocity magnitude. Thus the force is constant, as described by Eq. 3.3.

MOTILITY: The self-propulsion of non-interacting cells is frequently modelled as the result of an Ornstein-Uhlenbeck process:

$$\frac{\partial \mathbf{m}}{\partial t} + (\mathbf{v}\cdot\nabla)\mathbf{m} = -\frac{1}{\lambda_m}\mathbf{m} + \boldsymbol{\phi}(\mathbf{x},t), \tag{3.4}$$

where $\mathbf{m}(\mathbf{x},t)$ is the local forcing arising from cell motility, λ_m is the persistence time and $\boldsymbol{\phi}$ is a white Gaussian noise field. With this choice of noise, Eq. 3.4 describes a persistent random motion of the cells, where the velocity changes on the time scale λ_m.

However, the finite extend of the cells impose a minimum length scale ℓ_m on the system, below which the velocity field should be constant, because a single cell constitutes a coherent unit. The length scale ℓ_m is imposed by letting $\boldsymbol{\phi}$ be white noise filtered with a Gaussian function of width ℓ_m:

$$\boldsymbol{\phi}(\mathbf{x},t) = \frac{1}{2\pi\ell_m^2}\int \xi(\mathbf{x}',t)\exp\left(-\frac{|\mathbf{x}-\mathbf{x}'|^2}{2\ell_m^2}\right)\mathrm{d}\mathbf{x}', \tag{3.5}$$

where $\xi(\mathbf{x},t)$ is a Gaussian white noise field of strength β_m.

The literature on models of collective motion of cells covers a broad range of approaches from agent based models [60, 66, 67], cellular Potts models [68–70], vertex models [71] to phase field models [72] and continuum models [46, 61–63, 73–77]. In formulating the above model, we have sought to:

1. *Make it simple*. The model should be able to capture the experimentally observed speed distribution, temporal and spatial velocity correlation functions and the division flow field using as few parameters as possible.

2. *Allow for experimental comparison*. The model is formulated in terms of the velocity field, which is experimentally accessible from time-lapse microscopy and PIV analysis.

3. *Allow for quantification of forces*. Therefore the model is formulated in a mechanical framework and treats the tissue mono layer as a material.

Furthermore, the continuum approach allows us to perform a number of analytical calculations.

3.2 CAPTURING BULK MOTION OF TISSUE

To assess the performance of the proposed model, Eq. 3.1-3.5 were simulated numerically and fitted to the statistical characteristics of tissue bulk motion obtained experimentally (Section B.3).

The results are displayed in Figure 3.5. The model is clearly capable of reproducing the exponential tails of the speed distributions (Figure 3.5a) and closely matches the temporal correlation functions (Figure 3.5c). The length scale of the spatial velocity correlation function is captured (Figure 3.5b), but the negative dip predicted by the model, signaling the presence of vortices of a characteristic length scale, is not present in the data.

We note, that the choice of either a drag term $-\alpha\mathbf{v}$ or a dry friction term $-\alpha\hat{\mathbf{v}}$ mainly affects the speed distributions. The model was simulated numerically with the friction term replaced by the drag term, and no considerable differences were detected in the correlation functions (Figure 3.6). Our analytical calculations support this finding, and the calculations are available in the SI of [3]. The speed distributions in the case of drag and dry friction are however very different, and the drag term does not result in an exponential tail.

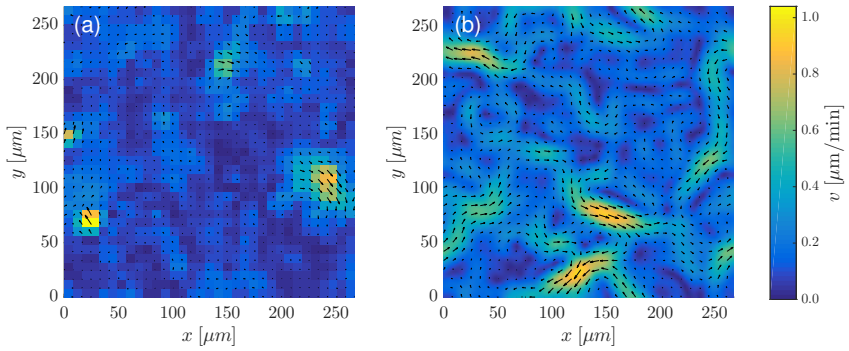

Figure 3.4: **Bulk velocity fields.** *(a) Experiment.* Snapshot of the velocity field during motion in the bulk of non-invasive human MCF7 cells. *(b) Model fit.* Snapshot of the velocity field of a simulation on a periodic domain. The simulation parameters have been fitted using the experimentally measured statistical characteristics of the MCF7 cell.

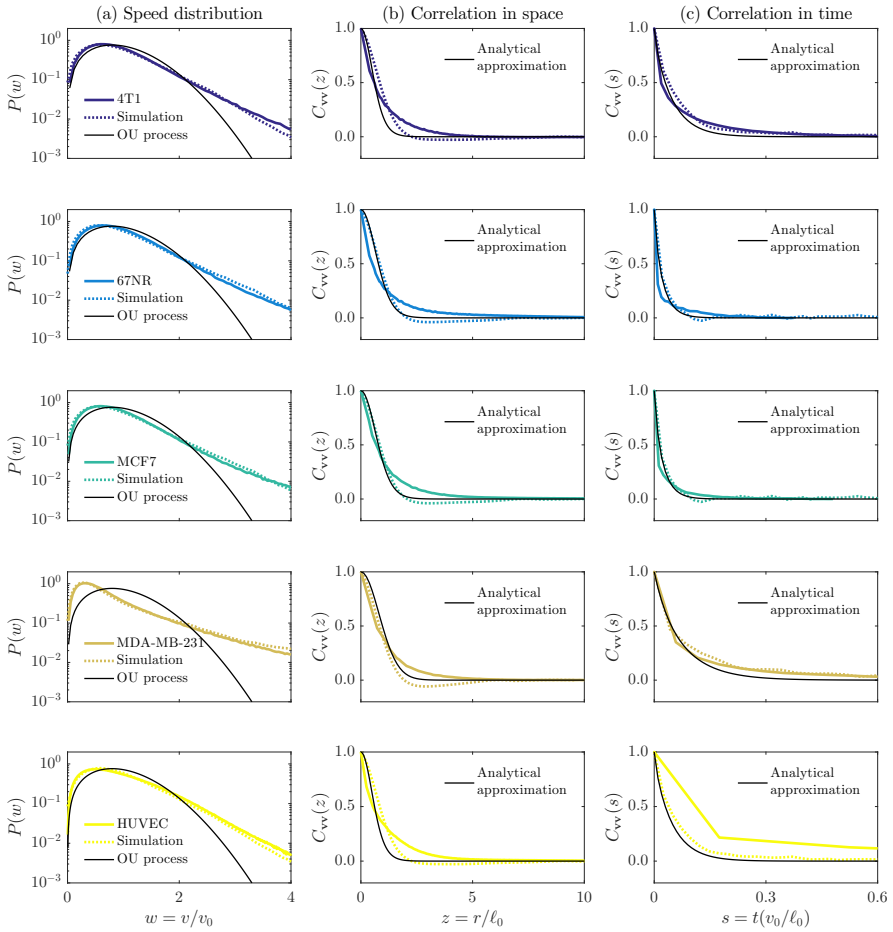

Figure 3.5: **Statistical characteristics of tissue dynamics.** Solid lines represent experimentally measured quantities, whereas dashed lines indicate the result of a model fit. *(a) Speed distribution* as a function of the speed v normalized with the mean speed v_0. The model captures the exponential tails of the speed distributions. The black lines depict the Gaussian tailed speed distribution, that would result from a pure Ornstein-Uhlenbeck process. *(b) The spatial velocity correlation* as a function of distance r scaled with the correlation length ℓ_0. The negative dips of the model fit correlation functions are not present in the data, but the agreement is otherwise reasonable. The black lines depict the analytical correlation functions in the case of a drag term replacing friction. The solutions closely resemble the model fits. *(c) The temporal velocity correlation* as a function of time t scaled with the characteristic time ℓ_0/v_0. The model fit closely matches the experiments. Also the analytical solution in the case of a drag term matches the experiments.

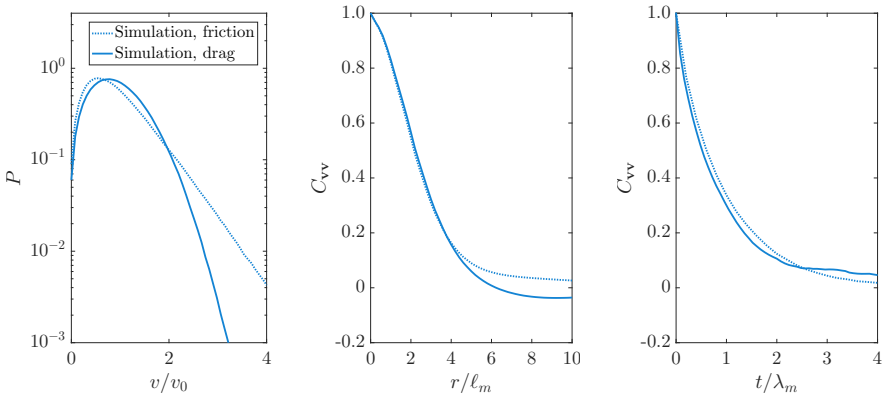

(a) Speed distribution (b) Spatial velocity correlation (c) Temporal velocity correlation

Figure 3.6: **Comparison of drag and friction.** Plot of the statistical characteristics resulting from numerical simulations using a friction term $\mathbf{f} = -\alpha\hat{\mathbf{v}}$ or a drag term $\mathbf{f} = -\alpha\mathbf{v}$ in Eq. 3.1. Whereas the speed distributions are clearly different in the case of friction and drag (Figure 3.6a), the spatial and temporal correlation functions are almost identical (Figure 3.6b-3.6c). The same set of parameters, representative of the parameters fitted to the experiments, was used for both friction and drag simulations.

3.3 CAPTURING THE CELL DIVISION PROCESS

The cell division process is of special interest in cancerous tissue, as one hallmark of cancer is uncontrolled cell division. Experimentally, the flow fingerprint of a cell division can be obtained by averaging over a number of cell division flow fields aligned along the direction of division and centered on the division site. The averaged flow fields will be denoted by an overline $\overline{\mathbf{v}}(\mathbf{x}, t)$. Experiments on Madin–Darby Canine Kidney cells revealed a force-dipole like flow field around the cell division site [75] in accordance with previous modeling efforts [74].

Cell division is not included in the model described by Eq. 3.1-3.5, as it was found to have a negligible effect on the bulk flow in the considered experiments. The flow field generated by a single cell division can however be predicted by the proposed model, in the form of the response to a force dipole turned on at time $t = 0$ and turned off at time $t = t_{off}$. When computing the flow field generated by a single cell division, the friction term $\mathbf{f}$ in Eq. 3.1 is discarded, as the friction should be small compared to the forces involved in the division process, for the cell division to be feasible. Also the motility term $\mathbf{m}$ in Eq. 3.1 is neglected, as we are interested in the effect of the cell division only. This condition is experimentally obtained by performing the aligned centered averages of flow fields.

In the absence of friction and intrinsic motility, the governing equations of the model are linear and we find an analytical solution for the flow field created by a single cell division [3]. The spatial and temporal dependencies separate:

$$\mathbf{v}(\mathbf{x}, t) = \mathbf{v}_{\text{Stokes}}(\mathbf{x})h(t), \tag{3.6}$$

where the time dependence $h(t)$ is:

$$h(t) = 1 - e^{-t/\lambda_2} - \left[1 - e^{-(t-t_{off})/\lambda_2}\right]\theta(t - t_{off}), \tag{3.7}$$

and $\mathbf{v}_{\text{Stokes}}(\mathbf{x})$ is the two-dimensional Stokes flow generated by a force dipole (two equal but opposite point forces $\pm\mathbf{b_0}$ located at $\mathbf{x} = \pm\mathbf{a}$ respectively):

$$\mathbf{v}_{\text{Stokes}}(\mathbf{x}) = \frac{1}{4\pi}\left\{[\mathbf{b}_0 \cdot (\mathbf{x} - \mathbf{a})]\frac{(\mathbf{x} - \mathbf{a})}{r_+^2} - [\mathbf{b}_0 \cdot (\mathbf{x} + \mathbf{a})]\frac{(\mathbf{x} + \mathbf{a})}{r_-^2} - \mathbf{b}_0 \ln\left(\frac{r_+}{r_-}\right)\right\}, \tag{3.8}$$

where $\mathbf{r}_\pm = |\mathbf{x} \mp \mathbf{a}|$. The velocity field in Eq. 3.6 was fitted to the time series of experimental averaged flow fields $\overline{\mathbf{v}}(\mathbf{x}, t)$. We fixed the duration of the force exertion t_{off} for all four cell types, as it was not found to significantly influence the obtained values of (λ_2, b_0), when included in the fitting procedure. The time dependence described

by Eq. 3.7 captures the experimentally observed time evolution (Figure 3.7), and also the spatial flow fields are well described by the model (Figure 3.8).

The fit to the experimental flow fields showed, that the invasive cell lines had a larger force to viscosity ratio b_0/η_0 during cell division, than the non-invasive cell lines (Figure 3.9). This was the case for both the human and murine cells and the difference was found to be statistical significant using a two-sided student's t-test [2]. If the cell lines have similar viscosities, this difference hints, that the invasive cancer cells might exert larger forces on the surrounding tissue during cell division than their non-invasive counterparts.

Whereas the spatial flow fingerprint of cell division has previously been described and modelled [75], the consideration of the temporal evolution of the flow field is new. We note, that the exact form of the time evolution function in Eq. 3.7 is governed by the rheological model. If a pure Maxwell fluid rheology had been used instead of the Oldroyd-B model, then the flow would have responded instantaneously to the forcing, leading to a time dependence $h(t) = \theta(t) - \theta(t - t_{off})$, where $\theta(t)$ is the Heaviside step function.

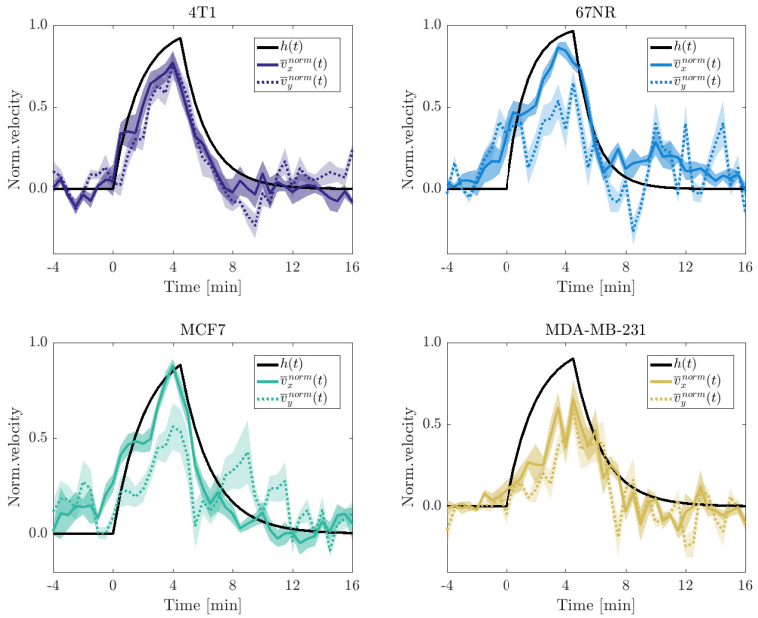

Figure 3.7: **Time evolution of flow field during cell division.** At each spatial point, we denote the maximal averaged velocity component during cell division $\bar{v}_{i,max}(\mathbf{x})$ for $i = x, y$. The full colored lines show the evolution of the normalized velocity components $\bar{v}_i^{norm}(t) := \langle \bar{v}_i(\mathbf{x}, t)/\bar{v}_{i,max}(\mathbf{x}) \rangle_{\mathbf{x}\in A}$ averaged over an area A close to the cell division center. The shading indicates the standard deviation. For a velocity field that separates into a spatial solution multiplied by a time dependent function, as in Eq. 3.6, the normalized velocity $\bar{v}_i^{norm}(t)$ should equal the time dependence function. The experimentally observed normalized velocity evolution is qualitatively well described by the model time dependence function $h(t)$ given in Eq. 3.7.

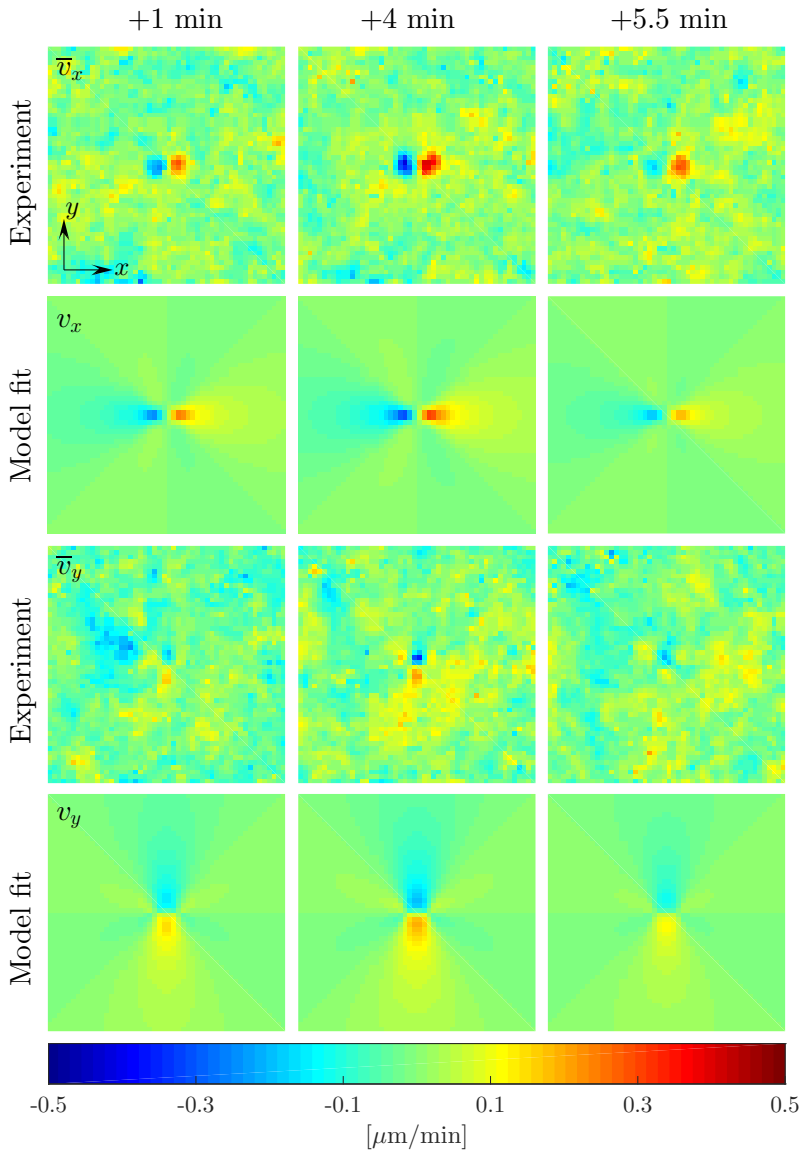

Figure 3.8: **Spatial evolution of flow field during cell division.** Plot of the experimental averaged velocity field $\overline{\mathbf{v}}(\mathbf{x}, t)$ during cell division of MCF7 cells, along with the velocity field $\mathbf{v}(\mathbf{x}, t)$ obtained by fitting the model prediction in Eq. 3.6 to the experimental $\overline{\mathbf{v}}(\mathbf{x}, t)$. The model captures the spatial structure and the temporal evolution of the experimental velocity field well. Time zero is defined as the onset of cytokinesis, i.e., the first image where two distinct daughter cells are visible, and each picture depicts a domain of 200×200 µm.

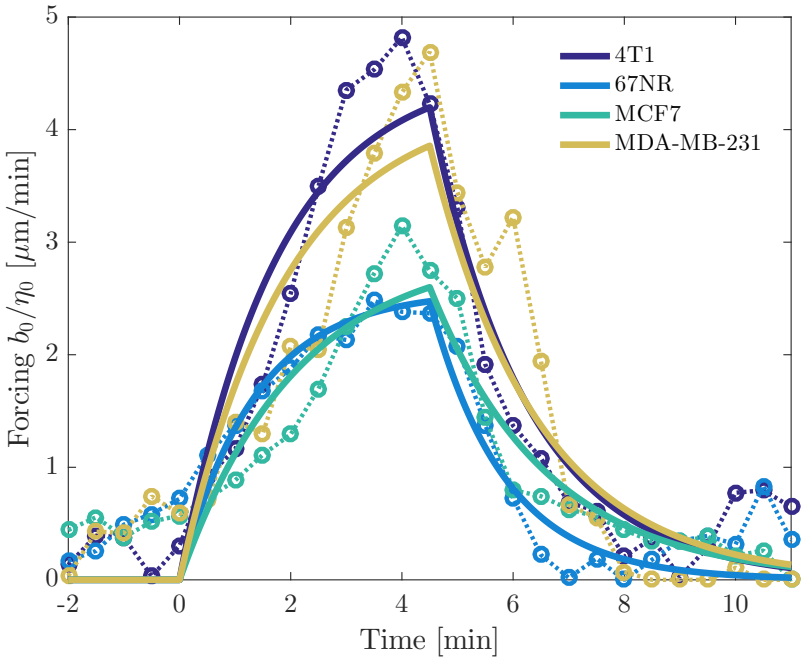

Figure 3.9: **Time evolution of forcing during cell division.** The solid lines represent the force divided by viscosity exerted by an expanding daughter cell, and are the result of fitting Eq. 3.6 to the experimental velocity *time series* $\bar{\mathbf{v}}(\mathbf{x}, t)$. For each of the four time series, one value of b_0/η_0 and λ_2 is obtained from the fitting procedure. The dotted lines represent fits to the same experimental data, when no time dependence is imposed on the model. I.e. for each time frame t_j with $j = 1 : N$, a Stokeslet dipole $\mathbf{v}_{sto}(x)$ is fitted to the *time frame* $\bar{\mathbf{v}}(\mathbf{x}, t_j)$. The result is a time series of b_0/η_0 values and serves as a test of the time dependence predicted by the model. The agreement between the *time series* fits (full lines) and the *time frame* fits (dashed lines) is reasonable. The invasive cell lines exert the largest force divided by viscosity during cell division and expansion. This is the case for both human and murine cells.

3.4 DISCUSSION

In this section we proposed a viscoelastic continuum model for tissue dynamics, which captured the exponential speed distribution tails as well as the temporal and spatial velocity correlations observed experimentally in five different cell lines. The model was formulated in a mechanical framework and thus naturally allowed for quantification of stress and forces in the tissue. The model furthermore allowed for an analytical solution of the velocity field induced by a single cell division. By fitting the model to the experimentally observed cell division flow fields, physical parameters such as retardation and relaxation times and cell division forces could be extracted. The proposed model differs in two aspects significantly from the previous literature on continuum models for tissue dynamics.

First, the proposed model includes a friction term similar to dry Coulomb friction, instead of the drag-like friction term traditionally employed [60–65]. The Coulomb type friction term is responsible for the model being able to reproduce the experimentally observed exponential tails of the tissue speed distributions. The substrate friction ultimately stems from a complex interplay between cell-substrate adhesion contacts, substrate properties and properties of any surrounding fluid. Experiments on the appropriateness of a drag- or a Coulomb-like friction with the substrate are therefore of interest and could yield valuable input to the modelling efforts.

Second, the proposed model is formulated in terms of the tissue velocity field, and the tendency of neighboring cells to align is incorporated through the material rheology. This contrasts approaches, where an explicit cell polarization field is included [61] or where the tissue is treated as an active nematic material [37, 65, 75, 78]. Recent experiments on kidney cell tissue revealed, that cell death and extrusion is highly correlated with the presence of $+1/2$ topological defects, when analyzing the tissue as an active nematic material [79]. I.e. the cell death and the subsequent extrusion is caused by the compressive stress field of a $+1/2$ defect, not by chemical signaling.

These experiments indicate, that the model proposed in this work might be too simple in its coarse graining of cell-cell interactions to pure rheology. The proposed model is not able to describe nematic features of the tissue, and thus can not account for the $+1/2$ defect induced cell death and extrusion.

The proposed model has been designed to reproduce the experimentally observed statistical characteristics of tissue dynamics and single cell division in the *tissue bulk*. However, migration of tissue into *unfilled space* is also an important aspect of tissue dynamics, which we have not considered in this work. Incorporating tissue boundaries in the proposed model, would allow for comparison and study of the classical scratch-wound assay experiment [45, 80, 81], the observed

fingering of tissue edges [45, 82] and the propagation of strain rate waves in spreading tissue [47], and thus be a natural next step.

When considering cancerous tissue, tumor growth is of great interest. An extensive literature on the modeling of tumor growth exists [83, 84] taking into account aspects such as evolution of tumor morphology, cell division and death, interaction between healthy and cancerous tissue as well as the effect of availability of resources such as oxygen and nutrients. Several of the continuum models of tumor growth lend themselves to different rheologies [83], and the specific rheology in Eq. 3.2 could be implemented.

The model hinted that one distinction between invasive and non-invasive cell types is the magnitude of the force, they exert during cell division. It would be of interest, to consider what the model tells us about the distinction between invasive and non-invasive cancer cells, when considering bulk motion.

4

COUPLING BETWEEN SUBSTRATE CURVATURE AND TEXTURE OF BLOCK COPOLYMERS

A block copolymer is composed of two or more distinct copolymers (the blocks) linked together with a covalent bond (Figure 4.1a). If the blocks are immiscible, then several textures with a characteristic length scale can form due to phase separation. The characteristic length scale is related to the length of the copolymer chains and is typically in the range of $10-100$ nm [85]. The transition from an isotropic homogeneous state to an ordered texture, as well as the type of texture arising are governed by the polymer molecular weight, the segmental interactions, and the volumetric composition [85]. In this section, we will focus on the cylindrical texture (Figure 4.1b-4.1c), which for instance occurs in diblock copolymers, where the two blocks have a comparable volume.

The cylindrical phase of a block copolymer film has the symmetry of a two-dimensional smectic liquid crystal [86]. It is liquid-like along one axis and described by a mass density wave along the orthogonal axis (Figure 4.2). We will refer to it as a striped phase, inspired by its appearance in SEM/TEM images. These striped thin films have attracted attention, since they can be used as self-organizing templates for nanofabrication of e.g. nanodots and wires [87–91] as well as defect functionalization [92, 93].

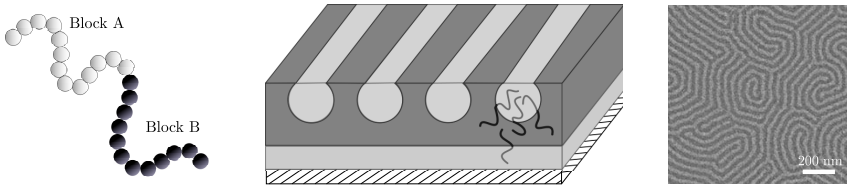

(a) *A block copolymer.* The constituent polymers of block A and B are immiscible.

(b) *Sketch of cylindrical texture.* The immiscibility of block A and B leads to phase separation. The sketch displays a possible configuration for a thin film of the block copolymer in (a).

(c) *Experimental cylindrical texture.* TEM picture adapted from [6].

Figure 4.1: **Block copolymers** can self-assemble into a variety of ordered states. In this chapter, we focus on thin layers of cylinder forming block copolymers as illustrated in *(a-c)*.

Defects are typically undesirable in these thin films but are hard to avoid, as the self-assembly process from a disordered state into the ordered cylindrical texture occurs via nucleation and growth or spinodal decomposition [94]. Several techniques aiming at reducing the

number of defects exist [85, 95], such as graphoepitaxy [96, 97], shear flow [98], electric fields [89, 99], sweeping of a temperature gradient [100] and using substrate curvature as an ordering field [101, 102]. In this chapter, we will focus on the effect of substrate curvature. It is of interest to understand and predict the textures of minimum energy for a given curved surface, since this is the state the block copolymers will evolve towards, as well as to study the defect structures and the ordering process of defect motion and annihilation.

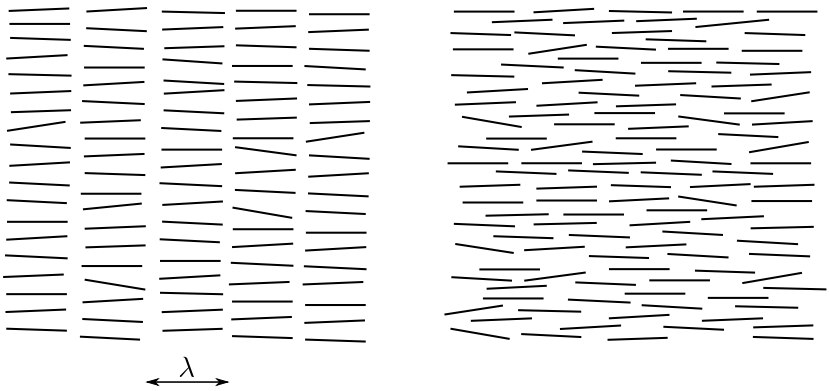

(a) *Smectic symmetry.* (b) *Nematic symmetry.*

Figure 4.2: **Symmetries.** The smectic phase in *(a)* shows translational order in the horizontal direction, resulting in a mass density wave, but is liquid-like along the vertical direction. The nematic phase in *(b)* possesses no translational order.

Several authors have developed models for the striped phase of block copolymers [103, 104], where both intrinsic and extrinsic bending of the stripes are energetically penalized. *Intrinsic* bending occurs, when the stripes deviate from geodesics of the surface. *Extrinsic* bending occurs, when the stripes bend in three dimensional space. As an example, consider only the two-dimensional top layers of the cylinders in Fig 4.3. The stripes running along the cylinder (Fig 4.3a) have neither intrinsic nor extrinsic bending, whereas stripes running around the cylinder (Fig 4.3c) have no intrinsic bending but do have extrinsic bending, because they are curved in three-dimensional space. The type of model considered by Santangelo et al. [103] and Kamien et al. [104], implies that stripes like to be straight in three-dimensions and that running along the cylinder as in Fig 4.3a is preferred.

However, the opposite behavior was experimentally observed for thin films [94, 102, 105]. In this paper, we therefore take the approach of Pezzutti, Gomez, and Vega [94], where the free energy is dominated by the deviation of the stripe spacing from its preferred value. This approach reproduces the experimentally observed tendency of the stripes to run around the cylinder as in Figure 4.3c. To understand the effect of a deviation from the preferred stripe spacing for

a thin film, consider first the striped thin layers in Figure 4.3a and b. The stripe spacing in both cases has to change in the radial direction, leading to the film being simultaneously under compression and dilation, see Figure 4.3 inset. The more curved the surface is, the larger the compression and dilation. So even though the films are thin, the third spatial dimension can not be neglected, as it effectively couples the free energy to the surface curvature.

In this chapter we develop an effective two-dimensional model for thin films of block copolymers by expanding the three-dimensional Brazovskii free energy in the film thickness. We benchmark the derived two-dimensional model against the known case of a cylindrical thin film. As this chapter contains non-finalized work, we go on to discuss future directions of the research and discuss other approaches to striped phases on curved surfaces.

4.1 THE FREE ENERGY FUNCTIONAL

We model a thin film of block copolymers using a Brazovskii type free energy functional [106], which frequently has been employed as a continuum level description of block copolymers [94, 105, 107–109]

The Brazovskii model was originally proposed to describe ordering transitions in antiferromagnets and cholesteric liquid crystals and has since inspired a range of works on phase transitions and pattern formation. Notably, the Swift-Hohenberg model [110], describing Rayleigh-Bénard convection, as well as the Phase Field Crystal model [111–113], describing crystals on atomic length scales and diffusive time scales, are extensions of the Brazovskii model.

The Brazovskii mean field free energy $F(\psi)$ is a Ginzburg-Landau expansion in the order parameter $\psi(\mathbf{x})$ performed under consideration of the system symmetries. We work with the free energy density $f = F/V$ also employed by Pezzutti, Gomez, and Vega [94] and Yamada and Komura [107]:

$$f(\psi) = \frac{1}{V}\int dV \left[2(\nabla^2\psi)^2 - 2|\nabla\psi|^2 + \frac{\tau}{2}\psi^2 + \frac{1}{4}\psi^4\right], \tag{4.1}$$

where V is the volume, $\psi(\mathbf{x}) = \rho(\mathbf{x}) - \rho_0$ measures the deviation of the local copolymer composition from the average composition ρ_0 at the critical temperature T_c. The model has one parameter, the reduced temperature $\tau = (T_c - T)/T_c$.

The negative sign of the gradient squared in Eq. 4.1 makes spatial modulations of the order parameter field ψ energetically favorable. In combination with the positive Laplacian squared, the negative gradient squared favors a specific wavelength $\lambda = 2\pi\sqrt{2}$. To see this, consider the free energy density of a field $\psi = \psi_0 \sin(q_0 x)$:

$$f(\psi) = \left(q_0^4 - q_0^2\right)\psi_0^2 + \frac{\tau}{4}\psi_0^2 + \frac{3}{32}\psi_0^4. \tag{4.2}$$

The free energy density is minimized for $q_0 = 1/\sqrt{2}$ resulting in a characteristic wave length $\lambda = 2\pi\sqrt{2}$. Any deviation from this spacing of the stripe pattern is energetically penalized.

In the current work, we focus on thin films on curved surfaces. A simple way to describe the free energy of the thin film is to consider the two-dimensional surface version of Eq. 4.1 where all derivatives have been replaced with their covariant surface equivalents:

$$f_{\tilde{S}}(\psi) = \frac{1}{\tilde{A}} \int d\tilde{A} \left[2(\tilde{\nabla}^2\psi)^2 - 2|\tilde{\nabla}\psi|^2 + \frac{\tau}{2}\psi^2 + \frac{1}{4}\psi^4 \right]. \tag{4.3}$$

Here, $\tilde{\nabla}$ denotes a covariant surface derivative on the surface $\tilde{S}$ and $d\tilde{A}$ is the area element of the curved surface. The strategy of replacing bulk derivatives with their surface equivalents has been applied to crystallization on curved surfaces using the related Phase Field Crystal model [109, 114] as well as in treatments of nematic crystals on curved surfaces using the Frank energy [93, 104, 115]. Replacing the bulk derivatives with their surface equivalents preserve the model's energetic penalty on all other wavelengths than λ. However, this approach does not take the third dimension into account, and results for example in all stripe orientations on a cylinder being equally energetically favorable, which is not in accordance with the experimental observations.

To properly account for the third dimension, we will start with the three-dimensional free energy density in Eq. 4.1 and expand it in the thickness of the film divided by the curvature length scale, to obtain a two-dimensional free energy density which takes the curvature of the surface into account.

4.2 GEOMETRICAL SETUP

We consider a thin three-dimensional region Ω of thickness h around a regular compact surface $\tilde{S}$ (Figure 4.4). We define $\tilde{\mathbf{n}}$ to be the unit normal vector field to the surface $\tilde{S}$. The volume Ω is described by the three-dimensional position vector $\mathbf{p}(u, w, \xi)$ parametrized by the three parameters (u, w, ξ):

$$\mathbf{p}(u, w, \xi) = \tilde{\mathbf{p}}(u, w) + \xi\, \tilde{\mathbf{n}}(u, w), \tag{4.4}$$

where $\tilde{\mathbf{p}}$ is the normal projection of the point $\mathbf{p}$ onto $\tilde{S}$. The distance between $\mathbf{p}$ and the surface $\tilde{S}$ along the normal $\tilde{\mathbf{n}}$ at a point $\tilde{\mathbf{p}}$ is given by $|\xi|$. The surface is of thickness h and thus $\xi \in [-h/2, h/2]$.

The tangent vectors at the point $\tilde{\mathbf{p}}(u, w) \in \tilde{S}$ are:

$$\tilde{\mathbf{a}}_i = \partial_i \tilde{\mathbf{p}}, \tag{4.5}$$

where the tilde indicates, that the tangent vectors belong to the surface $\tilde{S}$ and the index i runs over the parametrization parameters u, w. The induced metric (first fundamental form) on the surface $\tilde{S}$ is:

$$\tilde{g}_{ij} = \tilde{\mathbf{a}}_i \cdot \tilde{\mathbf{a}}_j. \tag{4.6}$$

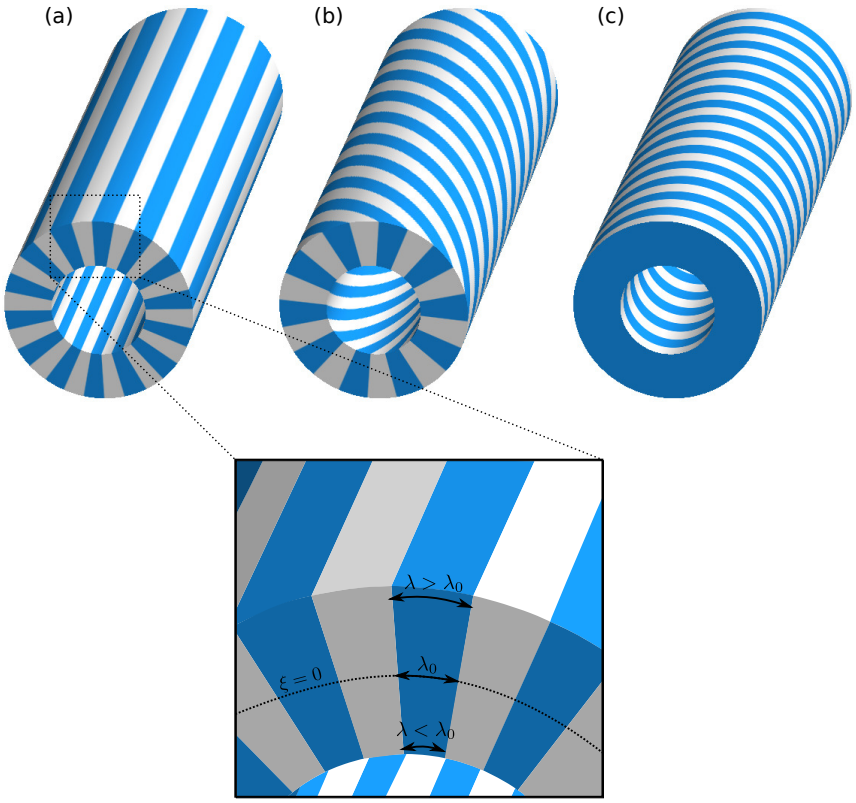

Figure 4.3: **Stripe textures on a cylindrical surface,** with different texture orientations, given by the angle α between the stripe direction and the axial direction. *(a)* When the stripe texture runs along the cylinder axis $\alpha = 0$, the finite thickness of the layer and the curvature of the cylinder results in a slight increase of the stripe wavelength λ with the radial coordinate, see inset. *(b)* Also the stripes with orientation $\alpha = \pi/4$ experience an increase of the wavelength in the radial direction, although the effect is smaller. *(c)* When the stripes run around the cylinder, $\alpha = \pi/2$ they are not affected by the curvature. The figure is inspired by [94].

The metric determinant will be denoted $\tilde{g}$. The metric inverse is $\tilde{g}^{ij}$ and defined such that $\tilde{g}^{ik}\tilde{g}_{jk} = \delta^i_j$, where repeated indices indicate summation. The metric and its inverse can be used to raise and lower indices. The curvature tensor (second fundamental form) of the surface $\tilde{S}$ is:

$$K_{ij} = \tilde{\mathbf{n}} \cdot (\partial_i \tilde{\mathbf{a}}_j). \tag{4.7}$$

We will not consider changes in the curvature. Thus K_{ij} describes all parallel surfaces in the volume Ω, and no tilde is used. We denote the two principal curvatures at the point $\tilde{\mathbf{p}}$ as $\kappa_1(\tilde{\mathbf{p}})$ and $\kappa_2(\tilde{\mathbf{p}})$ respectively. If we define the local curvature length scale, $l(\tilde{\mathbf{p}})$ and the global curvature length scale, $\ell(\tilde{\mathbf{p}})$, as:

$$l(\tilde{\mathbf{p}}) = \min\left[\frac{1}{\kappa_1(\tilde{\mathbf{p}})}, \frac{1}{\kappa_2(\tilde{\mathbf{p}})}\right] \qquad \ell = \min_{\tilde{\mathbf{p}}\in\tilde{S}} l(\tilde{\mathbf{p}}), \tag{4.8}$$

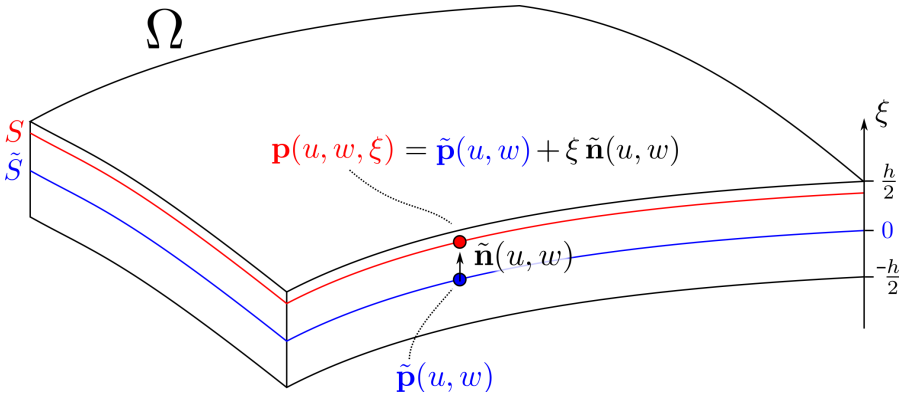

Figure 4.4: **Geometrical setup.** The thin film volume Ω is comprised of a series of parallel surfaces S with $\xi \in [-h/2, h/2]$ around the central surface $\tilde{S}$ with $\xi = 0$. The point $\tilde{\mathbf{p}} \in \tilde{S}$ is the normal projection of the point $\mathbf{p} \in S$ onto $\tilde{S}$. The surfaces are parametrized by (u, w), and the tangent vectors (not depicted) at $\mathbf{p}(u, w, \xi)$ and $\tilde{\mathbf{p}}(u, w)$ are in general not identical. I.e., for the same parameters (u, w), the tangent vectors change, as ξ traverses the interval $[-h/2, h/2]$.

then the requirement of the volume Ω being a thin shell can be formulated as:

$$\frac{h}{\ell} \ll 1. \tag{4.9}$$

We consider the scalar order parameter field ψ to be constant throughout the thickness of the shell:

$$\psi(\tilde{\mathbf{p}} + \xi\tilde{\mathbf{n}}) = \psi(\tilde{\mathbf{p}}) \qquad \text{for all} \qquad \tilde{\mathbf{p}} \in \tilde{S}, \;\; \xi \in \left[-\frac{h}{2}, \frac{h}{2}\right]. \tag{4.10}$$

The covariant gradient and Laplacian of the scalar field ψ and the divergence of the vector field $\mathbf{v}$ on the surface $\tilde{S}$ are:

$$\tilde{\nabla}^i\psi = \tilde{g}^{ij}\tilde{\nabla}_j\psi = \tilde{g}^{ij}\partial_j\psi \tag{4.11}$$

$$\tilde{\nabla}^2\psi = \tilde{\nabla}_i\tilde{\nabla}^i\psi = \frac{1}{\sqrt{\tilde{g}}}\partial_i(\sqrt{\tilde{g}}\tilde{g}^{ij}\partial_j\psi) \tag{4.12}$$

$$\tilde{\nabla}\cdot\mathbf{v} = \tilde{\nabla}_i v^i = \frac{1}{\sqrt{\tilde{g}}}\partial_i(\sqrt{\tilde{g}}v^i), \tag{4.13}$$

where $\tilde{g}$ is the metric determinant.

The goal is to expand the three-dimensional free energy density described by Eq. 4.1 in the surface normal coordinate ξ, the curvature tensor K_{ij} in Eq. 4.7, invariants of the surface $\tilde{S}$ such as the mean curvature H and the Gaussian curvature K and the surface derivatives in Eq. 4.11-4.13. When this expansion has been performed, the surface height $\xi \in \left[-\frac{h}{2}, \frac{h}{2}\right]$ can be integrated out, and we arrive at an effective two dimensional free energy density to lowest order in the surface thickness to curvature ratio h/ℓ. We assume that $h/\ell \ll 1$ throughout this chapter and we do not consider derivatives of the curvature tensor.

4.3 EXPANSION OF THE FREE ENERGY DENSITY

The free energy density in Eq. 4.1 has five terms, which should be expanded. The volume element dV, the gradient squared $|\nabla\psi|^2$, the Laplacian squared $(\nabla^2\psi)^2$ and the two powers of the order parameter field.

To perform these five expansions we need an expression for the metric on the parallel surfaces $g_{ij} = \mathbf{a}_i \cdot \mathbf{a}_j$. First step is to find the surface tangent vectors of the parallel surface S:

$$\mathbf{a}_i = \partial_i \mathbf{p} = \partial_i \tilde{\mathbf{p}} + \xi \partial_i \tilde{\mathbf{n}} = \tilde{\mathbf{a}}_i + \xi \partial_i \tilde{\mathbf{n}}. \tag{4.14}$$

Because $\tilde{\mathbf{n}} \cdot \tilde{\mathbf{n}} = 1$ then $\partial_i \tilde{\mathbf{n}} \cdot \tilde{\mathbf{n}} = 0$ and $\partial_i \tilde{\mathbf{n}}$ is orthogonal to the normal $\tilde{\mathbf{n}}$. Thus $\partial_i \tilde{\mathbf{n}}$ can be expressed as a linear combination of the mid surface tangent vectors $\partial_i \tilde{\mathbf{n}} = A_i^k \tilde{\mathbf{a}}_k$. We can identify A_i^k by dotting with a tangent vector:

$$\begin{aligned} \tilde{\mathbf{a}}_j \cdot \partial_i \tilde{\mathbf{n}} &= A_i^k \, \tilde{\mathbf{a}}_j \cdot \tilde{\mathbf{a}}_k \\ -K_{ij} &= A_i^k \tilde{g}_{jk} \\ A_i^k &= -K_{ij} \tilde{g}^{jk}, \end{aligned} \tag{4.15}$$

where we have used, that because $\tilde{\mathbf{a}}_j \cdot \tilde{\mathbf{n}} = 0$ then $\tilde{\mathbf{a}}_j \cdot \partial_i \tilde{\mathbf{n}} = -\partial_i \tilde{\mathbf{a}}_j \cdot \tilde{\mathbf{n}} = -K_{ij}$. With the aid of Eq. 4.15 we can rewrite Eq. 4.14 as:

$$\mathbf{a}_i = \tilde{\mathbf{a}}_i - \xi K_{ij} \tilde{g}^{jk} \tilde{\mathbf{a}}_k. \tag{4.16}$$

The metric on the parallel surfaces can then be expressed as:

$$g_{ij} = \mathbf{a}_i \cdot \mathbf{a}_j = \tilde{g}_{ij} - 2\xi K_{ij} + \xi^2 \tilde{g}^{kl} K_{ik} K_{jl}. \tag{4.17}$$

Note, that the above equation is exact. The metric inverse can be found by demanding that $g_{ik} g^{kj} = \delta_i^j$. To second order in the small quantity ξ/ℓ, the inverse metric is [116]:

$$\begin{aligned} g^{ij} &= \tilde{g}^{ij} + 2\xi K^{ij} + 3\xi^2 (2HK^{ij} - K\tilde{g}^{ij}) + \mathcal{O}^3(\xi/\ell) \\ &= (1 - 3\xi^2 K)\tilde{g}^{ij} + 2(\xi + 3\xi^2 H) K^{ij} + \mathcal{O}^3(\xi/\ell). \end{aligned} \tag{4.18}$$

The square root of the metric determinant is [116]:

$$\sqrt{g} = J_\xi \sqrt{\tilde{g}} \qquad \text{where} \qquad J_\xi = 1 - 2H\xi + K\xi^2. \tag{4.19}$$

Here, H is the mean curvature and K the Gaussian curvature.

4.3.1 *The volume element*

We denote the volume of Ω by $V = \mathrm{vol}(\Omega)$ and the surface area of $\tilde{S}$ by $\tilde{A} = \mathrm{area}(\tilde{S})$. We imagine the volume Ω to be comprised of a series of surfaces S parallel to $\tilde{S}$. Each of these parallel surfaces is described by Eq. 4.4 for a fixed value of ξ, with $\xi = 0$ corresponding to the central

surface $\tilde{S}$ (4.4). The surface area element of the central surface $\tilde{S}$ is denoted $d\tilde{A}$, whereas the surface area element of the parallel surface S is denoted dA. The volume element $dV = d\xi dA$ depends on the normal coordinate ξ through the area element dA. Using Eq. 4.19:

$$dA = J_\xi d\tilde{A}. \tag{4.20}$$

We note, that the volume V can be expressed as:

$$V = \int_\Omega dV = \int_{-h/2}^{h/2} d\xi \int_S dA = \int_{-h/2}^{h/2} d\xi \int_{\tilde{S}} d\tilde{A}\, J_\xi = \tilde{A}h + \frac{h^3}{12}\chi,$$

where we have introduced the integrated Gaussian curvature $\chi = \int_{\tilde{S}} d\tilde{A}\, K$, which for a surface with no boundary is the Euler characteristic of the surface times 2π.

4.3.2 *The gradient squared*

The squared gradient of the scalar field ψ on the parallel surface S is:

$$\begin{aligned}
|\nabla\psi|^2 &= g_{ij}(\nabla^i\psi)(\nabla^j\psi) = g^{ij}\nabla_i\psi\nabla_j\psi \\
&= (1-3\xi^2K)\tilde{g}^{ij}\tilde{\nabla}_i\psi\tilde{\nabla}_j\psi + 2(\xi+3\xi^2H)K^{ij}\tilde{\nabla}_i\psi\tilde{\nabla}_j\psi \\
&= (1-3\xi^2K)|\tilde{\nabla}\psi|^2 + 2(\xi+3\xi^2H)K^{ij}\tilde{\nabla}_i\psi\tilde{\nabla}_j\psi.
\end{aligned} \tag{4.21}$$

The expression in Eq. 4.21 depends explicitly on the normal coordinate ξ and we can perform the expansion in ξ/ℓ:

$$\begin{aligned}
J_\xi|\nabla\psi|^2 &= (1-2H\xi+K\xi^2)|\nabla\psi|^2 \\
&= c_0 + c_1\xi + c_2\xi^2 + c_3\xi^3 + \mathcal{O}^4(\xi/\ell),
\end{aligned} \tag{4.22}$$

where $c_n(\psi)$ for $n = 1, 2, \ldots$ is a curvature coupling term, and has the characteristic size $|\tilde{\nabla}\psi|^2/\ell^n$. The relevant even coefficients are:

$$c_0(\psi) = |\tilde{\nabla}\psi|^2 \tag{4.23}$$

$$c_2(\psi) = 2HK^{ij}\tilde{\nabla}_i\psi\tilde{\nabla}_j\psi - 2K|\tilde{\nabla}\psi|^2. \tag{4.24}$$

The gradient contribution to the free energy density is then:

$$\begin{aligned}
\int_\Omega dV\, |\nabla\psi|^2 &= \int_{-h/2}^{h/2} d\xi \int_S dA\, |\nabla\psi|^2 \\
&= \int_{\tilde{S}} d\tilde{A} \int_{-h/2}^{h/2} d\xi\, J_\xi|\nabla\psi|^2 \\
&= \int_{\tilde{S}} d\tilde{A} \int_{-h/2}^{h/2} d\xi \left[|\tilde{\nabla}\psi|^2 + c_1\xi + c_2\xi^2 + c_3\xi^3 + \mathcal{O}^4(\xi/\ell)\right] \\
&\approx h\int_{\tilde{S}} d\tilde{A}\, |\tilde{\nabla}\psi|^2 + \frac{h^3}{12}\int_{\tilde{S}} d\tilde{A}\, c_2(\psi).
\end{aligned} \tag{4.25}$$

Only the terms even in ξ survive the integration and the first truncated term in Eq. 4.25 is therefore of the order $\mathcal{O}^4(h/\ell)$.

4.3.3 *The Laplacian squared*

The Laplacian squared is calculated in the same fashion as the gradient squared, and we neglect derivatives of the curvature tensor. The Laplacian of the scalar field ψ on the parallel surface S is:

$$\begin{aligned}\nabla^2\psi = \nabla_i\nabla^i\psi &= \frac{1}{\sqrt{g}}\partial_i(\sqrt{g}g^{ij}\partial_j\psi)\\ &= \frac{1}{\sqrt{\tilde{g}}}\partial_i(\sqrt{\tilde{g}}g^{ij}\partial_j\psi)\\ &= (1-3\xi^2K)\tilde{\nabla}^2\psi + 2(\xi+3\xi^2H)\frac{1}{\sqrt{\tilde{g}}}\partial_i\left(\sqrt{\tilde{g}}K^{ij}\partial_j\psi\right) \quad (4.26)\\ &= (1-3\xi^2K)\tilde{\nabla}^2\psi + 2(\xi+3\xi^2H)(\tilde{\nabla}\cdot\mathbf{v}), \quad (4.27)\end{aligned}$$

where we have defined the vector field $v^i = K^{ij}\nabla_j\psi$, and identified the last term in Eq. 4.26 as the divergence of $\mathbf{v}$. As we do not consider derivatives of the curvature tensor, we can also write $\tilde{\nabla}\cdot\mathbf{v} = \tilde{\nabla}_i v^i = K^{ij}\tilde{\nabla}_i\tilde{\nabla}_j\psi$. The expression in Eq. 4.27 depends explicitly on the normal coordinate ξ and we can perform the expansion:

$$J_\xi(\nabla^2\psi)^2 = d_0 + d_1\xi + d_2\xi^2 + d_3\xi^3 + \mathcal{O}^4(\xi/\ell), \quad (4.28)$$

where the curvature couplings terms $d_n(\psi)$ have the characteristic size $(\tilde{\nabla}^2\psi)^2/\ell^n$. The relevant even coefficients are:

$$d_0(\psi) = (\tilde{\nabla}^2\psi)^2 \quad (4.29)$$

$$\begin{aligned}d_2(\psi) &= 4(\tilde{\nabla}\cdot\mathbf{v})^2 + 4H(\tilde{\nabla}\cdot\mathbf{v})(\tilde{\nabla}^2\psi) - 5K(\tilde{\nabla}^2\psi)^2\\ &= 4(K^{ij}\tilde{\nabla}_i\tilde{\nabla}_j\psi)^2 + 4H(K^{ij}\tilde{\nabla}_i\tilde{\nabla}_j\psi)(\tilde{\nabla}^2\psi) - 5K(\tilde{\nabla}^2\psi)^2.\end{aligned} \quad (4.30)$$

The Laplacian contribution to the free energy density is then:

$$\begin{aligned}\int_\Omega dV\,(\nabla^2\psi)^2 &= \int_{-h/2}^{h/2} d\xi \int_S dA\,(\nabla^2\psi)^2\\ &= \int_{\tilde{S}} d\tilde{A}\int_{-h/2}^{h/2} d\xi\,\left[(\tilde{\nabla}^2\psi)^2 + d_1\xi + d_2\xi^2 + d_3\xi^3 + \mathcal{O}^4(\xi/\ell)\right]\\ &\approx h\int_{\tilde{S}} d\tilde{A}\,\left(\tilde{\nabla}^2\psi\right)^2 + \frac{h^3}{12}\int_{\tilde{S}} d\tilde{A}\,d_2(\psi) \quad (4.31)\end{aligned}$$

Only the terms even in ξ survive the integration and the first truncated term in Eq. 4.31 is therefore of the order $\mathcal{O}^4(h/\ell)$.

4.3.4 *Powers of the order parameter field*

We note that the density field is constant throughout the thickness of the film. In other words, ψ does not depend on ξ. The expansion of the n'th power of ψ is:

$$\begin{aligned}\int_\Omega dV\,\psi^n &= \int_{-h/2}^{h/2} d\xi \int_S dA\,\psi^n \\ &= h\int_{\tilde{S}} d\tilde{A}\,\psi^n + \frac{h^3}{12}\int_{\tilde{S}} d\tilde{A}\,\psi^n K. \end{aligned} \tag{4.32}$$

So if the surface has a constant Gaussian curvature, then the expression reduces to $\frac{1}{V}\int_\Omega dV\,\psi^n = \frac{1}{\tilde{A}}\int_{\tilde{S}} d\tilde{A}\,\psi^n$.

4.3.5 *The final two-dimensional free energy density*

Substituting Eq. 4.25,4.31,4.32 in the three-dimensional free energy density in Eq. 4.1, we arrive at:

$$\begin{aligned} f(\psi) &= \frac{h\tilde{A}}{V}\left\{ f_{\tilde{S}}(\psi) + \frac{1}{12}\frac{1}{\tilde{A}}\int_{\tilde{S}} d\tilde{A}\; h^2\left[2d_2(\psi) - 2c_2(\psi) + \frac{\tau}{2}K\psi^2 + \frac{1}{4}K\psi^4\right]\right\} \\ &= \frac{h\tilde{A}}{V}\left[f_{\tilde{S}}(\psi) + k_{\tilde{S}}(\psi)\right], \end{aligned} \tag{4.33}$$

which is valid up to the order of $\mathcal{O}^4(h/\ell)$ and we have defined the curvature correction term $k_{\tilde{S}}(\psi)$. We note, that the volume differs from the area times the thickness $V \neq h\tilde{A}$, unless the surface has zero integrated Gaussian curvature, $\chi = 0$.

4.4 RELAXATION TOWARDS EQUILIBRIUM

The relaxation of the conserved density field ψ towards equilibrium is similarly to the Phase Field Crystal model described by the equation of motion [94, 107]:

$$\frac{\partial\psi}{\partial t} = M\tilde{\nabla}^2\left(\frac{\delta f}{\delta\psi}\right) + \eta(\mathbf{r},t), \tag{4.34}$$

where $\delta f/\delta\psi$ denotes a functional derivative, M is a phenomenological mobility constant and $\eta(\mathbf{r},t)$ is a noise term. The noise has zero mean $\langle\eta(\mathbf{r},t)\rangle = 0$ and the fluctuation-dissipation theorem relates the noise strength η_0 and the mobility constant M:

$$\left\langle\eta(\mathbf{r},t)\eta(\mathbf{r}',t')\right\rangle = 2M\eta_0\delta(\mathbf{r}-\mathbf{r}')\delta(t-t'). \tag{4.35}$$

The functional derivative of the free energy density in Eq. 4.33 can be found in Appendix C.1.

4.5 A BENCHMARK PROBLEM

The expansion of the three-dimensional free energy density in Eq. 4.1 in powers of the small quantity h/ℓ was performed for the special case of the cylinder by Pezzutti, Gomez, and Vega [94]. They find that the free energy is minimized when the stripes run around the cylinder as in Figure 4.3c, thus qualitatively behaving as the experiments [94, 102, 105]. The surface free energy density derived in this chapter is the generalization of the work by Pezzutti, Gomez, and Vega [94], and we therefore use their result for the cylinder as a benchmark problem.

We parametrize the cylindrical surface $\tilde{S}$ of radius R and length L by the cylindrical coordinates $u \in [0, 2\pi], w \in [0, L]$:

$$\tilde{\mathbf{p}} = \begin{bmatrix} R\cos(u) \\ R\sin(u) \\ w \end{bmatrix} \tag{4.36}$$

Relevant geometrical quantities associated with the specific parametrization are:

$$\tilde{g}_{uu} = R^2 \qquad \tilde{g}_{ww} = 1 \qquad \tilde{g}_{uw} = \tilde{g}_{uw} = 0 \tag{4.37}$$

$$K_{uu} = R \qquad K_{ww} = 0 \qquad K_{uw} = K_{uw} = 0 \tag{4.38}$$

$$K = 0 \qquad H = \frac{1}{2R} \tag{4.39}$$

We consider a striped texture making an angle α with the axis of the cylinder, see Fig 4.3:

$$\psi(u, w) = \psi_0 \cos\Big[q_0(Ru\cos(\alpha) + w\sin\alpha)\Big] = \psi_0\cos(\beta), \tag{4.40}$$

where for convenience, we have defined $\beta = q_0(Ru\cos(\alpha) + w\sin\alpha)$. Since the Gaussian curvature vanishes everywhere, the curvature coupling terms reduce to:

$$\begin{aligned}
c_2 &= 2HK^{ij}\partial_i\psi\partial_j\psi \\
&= 2Hg^{uu}g^{uu}K_{uu}\partial_u\psi\partial_u\psi \\
&= \frac{q_0^2\psi_0^2}{R^2}\cos^2(\alpha)\sin^2(\beta) \\
d_2 &= 4(K^{ij}\tilde{\nabla}_i\tilde{\nabla}_j\psi)^2 + 4H(K^{ij}\tilde{\nabla}_i\tilde{\nabla}_j\psi)(\tilde{\nabla}^2\psi) \\
&= 4(K^{uu}\partial_u\partial_u\psi)^2 + 4H(K^{uu}\partial_u\partial_u\psi)(g^{uu}\partial_u\partial_u\psi + g^{ww}\partial_w\partial_w\psi) \\
&= \frac{1}{R^2}\left[\frac{6}{R^4}(\partial_u\partial_u\psi)^2 + \frac{2}{R^2}(\partial_w\partial_w\psi)(\partial_u\partial_u\psi)\right] \\
&= \frac{q_0^4\psi_0^2}{R^2}\Big[6\cos^4(\alpha) + 2\cos^2(\alpha)\sin^2(\alpha)\Big]\cos^2(\beta) \\
&= \frac{q_0^4\psi_0^2}{R^2}\left[4\cos^4(\alpha) + 2\cos^2(\alpha)\right]\cos^2(\beta).
\end{aligned}$$

So the curvature contribution to the free energy is:

$$k_{\tilde{S}} = \frac{1}{12}\frac{1}{\tilde{A}}\int_{\tilde{S}} d\tilde{A}\; h^2\Big[2d_2(\psi) - 2c_2(\psi)\Big] \tag{4.41}$$

$$= \frac{1}{12}\left(\frac{h}{R}\right)^2 \psi_0^2\Big[4q_0^4\cos^4(\alpha) + (2q_0^4 - q_0^2)\cos^2(\alpha)\Big] \tag{4.42}$$

$$= \frac{1}{12}\left(\frac{h}{R}\right)^2 \psi_0^2\cos^4(\alpha), \tag{4.43}$$

where we have inserted the preferred wavelength $q_0 = 1/\sqrt{2}$ in the last step. The curvature contribution to the energy is minimized when $\alpha = \pi/2$ and the stripes on every parallel surface are able to maintain the preferred lattice spacing controlled by q_0. Thus the stripes prefer to align with the direction of maximal principal curvature and run around the cylinder as depicted in Figure 4.3c. The result in Eq. 4.43 is identical to the result of Pezzutti, Gomez, and Vega [94].

Note that the model *on a general surface* results in a local tendency of the stripes to align with the direction of maximal principal curvature. Thus curvature acts as a *local ordering field*.

4.6 FUTURE DIRECTIONS

Though the free energy density in Eq. 4.33 lends itself to analytical calculations for simple surfaces, a numerical approach is necessary in order to deal with more complicated and interesting surfaces as well as to study the time evolution of the block copolymer textures and the global effect of the local ordering due to curvature.

The model is currently being implemented numerically, and the approach and challenges are described in Section 4.6.4. With the numerical implementation at hand, several aspects of thin block copolymer films can be investigated. We plan to focus on 1) identifying minimum energy textures, 2) studying curvature as an ordering field and 3) investigating ordering kinetics. These three aspects are discussed in the following subsections.

4.6.1 *Minimum energy texture*

As discussed in the chapter introduction, the textures formed by block copolymers are used as patterns for nano-fabrication. It is therefore of interest to calculate the texture with the lowest free energy for a given curved surface, thus predicting the resulting pattern. Also the reverse situation, of being able to identify a curved surface that will result in a pre-specified pattern, is of interest.

A first step is to study the minimum energy configuration on a sphere, where a total rotational defect charge of $+2$ is required due to the Poincaré–Hopf theorem. Several defect configurations are possible (Figure 4.5), and the energy of these have previously been studied

numerically [117, 118] using a self-consistent field theory for block copolymers. A comparison with this previous work would be relevant and is currently being pursued.

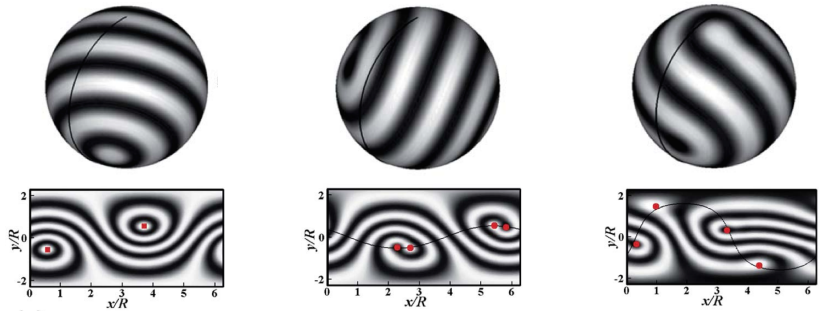

(a) *Polar structure.* (b) *Spiral structure.* (c) *Baseball structure.*

Figure 4.5: **Defect structures.** Examples of defect structures in a striped phase fulfilling the requirement of a total rotational defect charge of +2. The top panel shows the texture in three dimensions and the lower panel displays a modified Mercator projection. Red squares indicate cores of +1 disclinations (see Figure *(a)*) whereas red circles indicate the cores of +1/2 disclinations (see Figure *(b,c)*). Figure adapted from Zhang, Wang, and Lin [109].

4.6.2 *Curvature as an ordering field*

For substrates with a vanishing Euler number, there is no topological requirement of defects. However, defects might still arise due to the distortions caused by the substrate. As a first step, we therefore plan to study the effect of a Gaussian bump on an otherwise planar surface (Figure 4.6a). The stripe texture will be distorted as it passes over the bump, and we wish to study the spatial extent of the distortion and the angular deviation of the stripes. Similar considerations of a Gaussian bump were done by Kamien et al. [104] using an alternative model for block copolymers. Based on their model, they devised broad design principles to engineer the geometry of the curved substrate and thereby obtain the desired block copolymer texture by self-assembly. The model by Kamien et al. differs significantly from the model derived in this chapter and will be discussed in Section 4.7.1.

As the texture of block copolymers self-organize during the phase transition from a disordered state to the striped phase, defects are completely unavoidable in the absence of any external fields. Curvature can however serve as an ordering field, limiting defect formation and enhancing defect annihilation. To investigate the role of curvature as an ordering mechanism, we plan to study a series of Gaussian ridges (Figure 4.6b), which we expect will suppress defects and align the stripes with the direction of maximal principal curvature.

(a) *Gaussian bump.* (b) *Gaussian ridge.*

Figure 4.6: **Curvature as an ordering field.** We plan to use the Gaussian bump and the Gaussian ridge as simple test grounds for the effect of curvature as an ordering field. Both surfaces are here depicted with a possible stripe texture.

4.6.3 *Ordering kinetics*

Experiments on the ordering of striped textures in block copolymers confined to *flat surfaces* have been performed, and especially the growth of micro domains and the defect annihilation process were studied in detail [56, 86].

The spatial size L of defect free micro domains with the same stripe orientation was experimentally found to depend on time as $L \sim t^{1/4}$ in flat space [56, 86]. This is in accordance with previous theoretical and numerical studies of flat space Brazovskii type models [119], and we wish to study whether this dependence change on curved substrates, where the ordering process might be enhanced by curvature.

The experiments also measured the time evolution of the defect numbers and carefully mapped out defect annihilation processes such as dipole and quadropole annihilation of disclinations as well as the ability of disclinations to act as sources/sinks for dislocations [56]. It would be interesting to compare the defect time evolution generated by the model in curved space with the flat space experiments.

The ordering kinetics of the striped phase has been studied numerically on a sinusoidal curved substrate [120]. However, these authors just replaced the derivatives in the three-dimensional Brazovskii free energy with covariant surface derivatives, in order to obtain a two-dimensional model. Curvature thus only affected the free energy through changes in distances on the surface, forcing the stripe spacing to change. The model discussed in Gómez and Vega [120] does therefore not consider the coupling between curvature and stripe spacing, arising from the finite thickness of the film.

4.6.4 *Numerical implementation*

The numerical implementation is ongoing work and not yet completed, but a brief overview of the intended approach is given here. A preliminary simulation example is shown in Figure 4.7.

An essential part of the numerical implementation is the discretization of the curved surface, its geometric attributes such as curvature and normal vectors and the discretization of differential operators on the surface.

The surface itself is discretized by a triangular mesh. Following Meyer et al. [121], the mean curvature (with the normal), the Gaussian curvature and the Laplacian are calculated at each vertex from spatial averages around this vertex. Principal curvatures and principal directions are calculated using constrained least-square fitting, with the linear constraint, that the sum of the principal curvatures equals twice the mean curvature. The density field ψ is discretized at the vertices of the triangle mesh.

The covariant derivatives are calculated by:

1. Projecting the 1-ring of a vertex v_i onto the tangent plane at v_i spanned by the principal directions.
2. Estimating the quadratic approxmiation of the order parameter ψ in the tangential plane using least squares fitting.
3. Obtaining the covariant derivatives in the principal directions from the quadratic approximation of ψ.

The time evolution of the density field is implemented using operator splitting into a linear and non-linear part. The linear part of the time evolution equation is solved for implicitly whereas the non-linear part (a ψ^3 term and noise) is integrated explicitly.

4.7 DISCUSSION

In this chapter we studied the striped phase of thin block copolymer films. For these systems, the finite film thickness results in a coupling between substrate curvature and the stripe wavelength. We derived an effective two-dimensional free energy functional by expanding the Brazovskii three-dimensional free energy in the ratio of the film thickness to the characteristic curvature length scale. The predicted orientation of the stripes on a cylinder is in accordance with previous calculations [94] and experiments [94, 102, 105].

To explore the effect of curvature on block copolymer films further, we are currently implementing the two-dimensional model numerically. A numerical implementation will allow us to assess the minimum energy texture for a given curved substrate, to investigate the effect of curvature as an ordering field, as well as to study the dynamics of defect annihilation and creation during the ordering process.

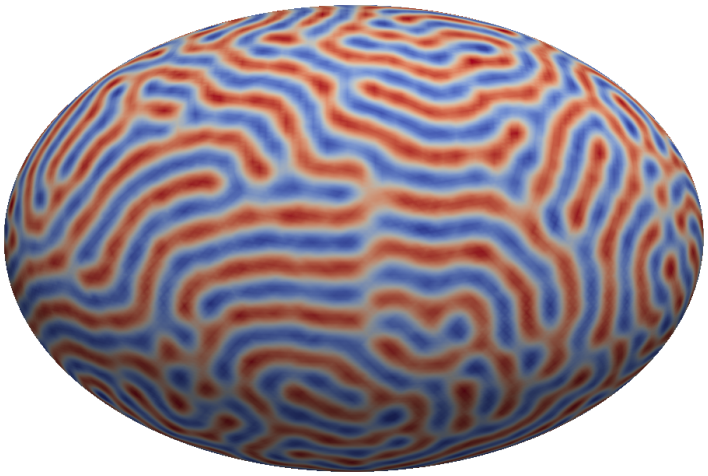

Figure 4.7: **Preliminary simulation example.** The derived effective two-dimensional model was simulated on the surface of an ellipsoid. Color indicates the value of the order parameter and the striped texture is clearly present.

4.7.1 *Previous models of block copolymers on curved substrates*

Block copolymers on curved surface have previously been modelled by introducing a free energy with two main ingredients: a term penalizing any deviation from the prescribed stripe spacing and a term penalizing any geodesic or normal curvature of the stripes [103, 104]. This ad hoc inclusion of curvature in the free energy results in the texture shown in Figure 4.3a being the lowest energy state on the cylinder and was inspired by experiments of Hexemer [101], which showed this behavior on the zero Gaussian curvature circle of a Gaussian bump (Figure 4.8a).

However, as Santangelo et al. [103] also note, the film in these experiments was not one-layered and: " How the underlying layers couple to the two-dimensional geometry of the topmost columns is an open question." Thus, the experiments on these approximately ten-layer thick films by Hexemer [101] are different from the one-layer film experiments by references [94, 102, 105], the latter being the inspiration for the thin-shell model in this chapter.

We note, that as opposed to the ad hoc inclusion of curvature in the model of Santangelo et al. [103], we have in this chapter introduced substrate curvature in the free energy in a controlled way, by expanding the three-dimensional equal stripe spacing requirement in the film thickness and obtaining an effective two-dimensional model.

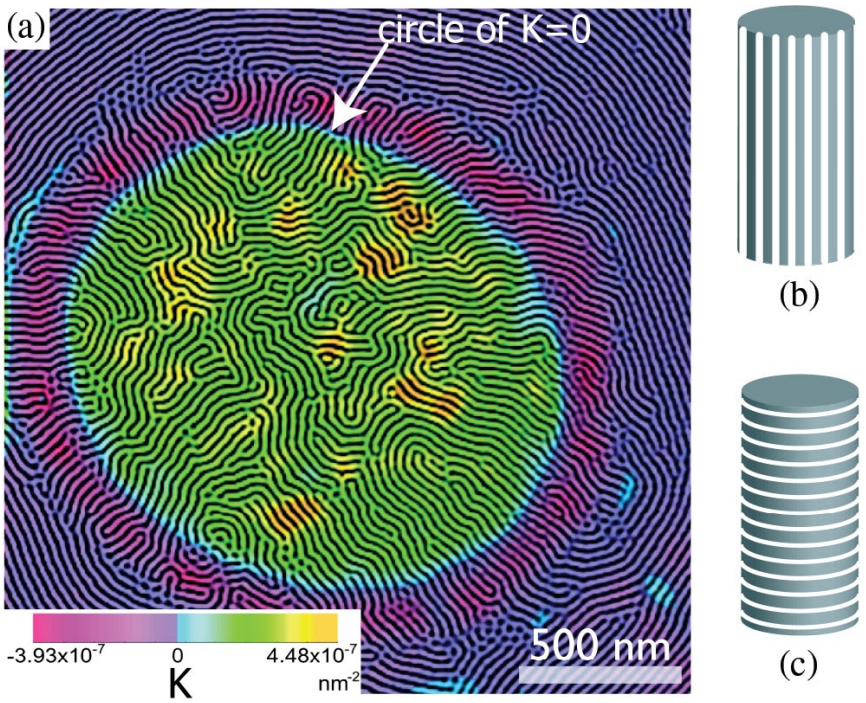

Figure 4.8: **Block copolymers on Gaussian bump.** The depicted film is about 10 layers thick. The circle of zero Gaussian curvature $K = 0$, is geometrically identical to a cylinder, and the stripes tend to be aligned as sketched in *(b)*. This is the opposite behavior of what was observed on single layer films as discussed in Section 4.7.1. The single layer films were observed to align as in Figure *(c)*. The figure is adapted from Santangelo et al. [103].

4.7.2 *Nematic approaches*

The experimental system of block copolymers considered in this chapter has smectic symmetry (Figure 4.2a). The smectic phase is however closely related to the nematic phase (Figure 4.2b), where the nematogens show orientational order but no mass density wave.

Napoli and Vergori [122, 123] modelled a thin layer of a nematic phase on a curved substrate. They obtained an effective two-dimensional model by expanding the three-dimensional Frank elastic energy of nematic liquid crystals to zeroth order in the small parameter h/ℓ (film thickness/curvature length scale). This is the same strategy, as we have used in this chapter. They also considered a cylindrical surface and found, that the absolute free energy minimum occurs, when the director field points along the cylindrical axis. This orientation of the director is similar to the block copolymers, where the director is perpendicular to the stripes (see Figure 4.2a), leading to the director pointing along the cylindrical axis, when the stripes run around the cylinder as in Figure 4.3c. A nematic approach was also used by Mbanga, Grason, and Santangelo [124] who studied defects in a ne-

matic phase on a catenoid, and by Segatti, Snarski, and Veneroni [125] who investigated the behavior of Napoli and Vergori's model [122, 123] on a torus.

The striped texture of block copolymer films considered in this chapter, is however not nematic, but the nematic models could be relevant for other related materials.

5 CONCLUSION

In this thesis we summarized and discussed our work on the three largely independent projects of columnar jointing, tissue dynamics and block copolymers on curved surfaces. The three topics were studied using continuum modeling, analytical calculations and numerical simulations.

We developed a simple linear elastic model for columnar jointing and argued from numerical simulations, that one Péclet number is selected for each dimensionless critical stress intensity factor. This observation allowed us to analytically derive a scaling function, giving the functional relation between the Péclet number and the dimensionless critical stress intensity factor. The derived scaling function was in excellent agreement with numerical simulations and with the few existing experimental measurements. The scaling function allowed us to estimate the speed of the crack front, if the column diameter and certain material parameters have been measured. Using the field measurements of Goehring and Morris [25], the crack front velocities were estimated and the results compared well with the independent estimates of Goehring and Morris [25].

Aiming at simplicity and the possibility for quantitative comparison with experiments, we formulated a continuum model for tissue dynamics. The model treated the tissue as a viscoelastic active fluid experiencing a dry friction with the underlying substrate. The model captured the spatial and temporal velocity correlations of experiments on breast cancer tissue as well as the speed distributions, which showed exponential tails. The model allowed for an analytical solution of the flow field generated by a single cell dividing, and the solution compared well with experimental observations.

To gauge the effect of curvature on thin films of cylinder forming block copolymers, we expanded the three-dimensional Brazovskii free energy for block copolymers in the ratio of film thickness to curvature length scale. By this procedure, we obtained an effective two-dimensional model, that incorporated the coupling between substrate curvature and stripe spacing. The obtained model reproduced the expected behavior of a thin layer of block copolymers on a cylinder, with the stripes running around the cylinder. We outlined future research directions, which we want to pursue using a numerical implementation of the model. These include identifying the minimum energy texture for relevant surfaces, studying the effect of curvature as an ordering field and the ordering kinetics of defect creation and annihilation.

A

APPENDIX: SCALE SELECTION IN COLUMNAR JOINTING

A.1 CONDUCTIVE COOLING WITH LATENT HEAT

A common igneous rock like basalt has a liquidus temperature of about $T_L = 1200°C$, a solidus temperature of about $T_S = 1000°C$ and a glass transition temperature of about $T_G = 725°C$ [14, 126]. Above the liquidus temperature, T_L, the material is a homogeneous melt, below T_L melt and solid material coexist, and below the solidus, T_S, the material is solidified. The glass transition, T_G, is a second order phase transition, where the thermal expansion coefficient and the Young's modulus change abruptly. Below T_G the system can no longer accommodate shrinkage by viscous relaxation, it becomes hard and brittle and effective stress starts to accumulate.

To gain insight in the temperature evolution of solidifying igneous rock, we consider a homogeneous and isotropic half-space $X \geqslant 0$. The X-axis is pointing into the igneous body, and at the interface $X = 0$ the body is in contact with a cooling substance (air, ground) such that the temperature is always $T(X = 0, t) = T_0$. Initially at time $t = 0$ the body is uniformly at the emplacement temperature $T(X, t = 0) = T_1$. Only the $X-$direction enters the heat diffusion equation, as the body is taken to be homogeneous and isotropic as well as infinite in the $Y-$ and $Z-$direction:

$$\frac{\partial T(X,t)}{\partial t} = D\nabla^2 T(X,t). \tag{A.1}$$

For the above specified boundary and initial conditions, the resulting temperature distribution is:

$$T(X,t) = T_0 + (T_1 - T_0)\,\mathrm{erf}\left(\frac{X}{2\sqrt{Dt}}\right), \tag{A.2}$$

where the error function is defined as: $\mathrm{erf}(\eta) = \frac{2}{\sqrt{\pi}} \int_0^\eta e^{-\tau^2} d\tau$.

The temperature distribution in Eq. A.2 does not take latent heat into account. Basalt releases the majority of latent heat in an interval of $1025°C - 1125°C$ [19], which is not easily incorporated in analytical models. Instead of completely neglecting latent heat, as in Eq. A.2, we can assume that solidification happens at a single temperature T_S. The solidification front is then always located at the T_S isotherm with position $x_m(t)$, such that $T(x_m(t), t) = T_S$.

We split the temperature field of the igneous body into two parts: one field, $T^s(x,t)$, describing the solidified part of the body for $x \leqslant$

$x_m(t)$ and one field, $T^l(x,t)$, describing the still molten part for $x \geqslant x_m(t)$. Continuity of temperature at the phase boundary demands:

$$T^s(x_m) = T^l(x_m) = T_S \tag{A.3}$$

If we consider solutions of the type $T(\eta)$, then the similarity variable $\eta = x/2\sqrt{Dt}$ must take a constant value δ on the solidus line at $x_m(t)$ in order to always fulfill Eq. A.3. This implies that $x_m(t) = 2\delta_s\sqrt{D_s t} = 2\delta_l\sqrt{D_l t}$ and therefore $\delta_l = \delta_s\sqrt{D_s/D_l}$.

We assume, that the air cools the surface of the igneous body to the temperature T_0, and that the liquid initially has the temperature T_1:

$$T^s(0,t) = T_0 \qquad T^l(x,0) = T_1 \tag{A.4}$$

Solving Eq. A.1 for each of the two temperature fields $T^s(x,t)$ and $T^l(x,t)$ with the boundary conditions in Eq. A.3-A.4 yields:

$$T^s(x,t) = T_0 + \frac{T_S - T_0}{\operatorname{erf}(\delta_s)} \operatorname{erf}\left(\frac{x}{2\sqrt{D_s t}}\right) \tag{A.5}$$

$$T^l(x,t) = \frac{T_1 \operatorname{erf}(\delta_l) - T_S}{\operatorname{erf}(\delta_l) - 1} + \frac{T_S - T_1}{\operatorname{erf}(\delta_l) - 1} \operatorname{erf}\left(\frac{x}{2\sqrt{D_l t}}\right) \tag{A.6}$$

The parameters δ_s, δ_l can be determined through considerations of the latent heat release. In our half space model, energy conservation implies that the difference in heat flux density through the phase boundary plane $x = x_m(t)$ must equal the release of latent heat:

$$K_s \frac{\partial T^s(x,t)}{\partial x}\Big|_{x=x_m} - K_l \frac{\partial T^l(x,t)}{\partial x}\Big|_{x=x_m} = \rho_l L \frac{dx_m(t)}{dt} \tag{A.7}$$

where K_l, K_s are the thermal conductivities of the solid and liquid phase respectively, ρ_l is the liquid density and L is the latent heat of the igneous rock. From Eq. A.7 we then get an implicit equation that together with $\delta_l = \delta_s\sqrt{D_s/D_l}$ determines δ_s:

$$\begin{aligned}\sqrt{D_s} L \rho_l \delta_s \sqrt{\pi} = &\frac{e^{-\delta_s^2}}{\operatorname{erf}(\delta_s)} \frac{K_s(T_S - T_0)}{\sqrt{D_s}} \\ &+ \frac{e^{-\delta_l^2}}{\operatorname{erf}(\delta_l) - 1} \frac{K_l(T_1 - T_S)}{\sqrt{D_l}}\end{aligned} \tag{A.8}$$

For air of temperature $T_0 = 20°C$ and similar thermal diffusivities and conductivities in the liquid and solid igneous phase, one obtains $\delta_l = \delta_s = 0.74$ for the physical parameters of lava listed in Table 2 of Degraff, Long, and Aydin [19]. An example of the obtained temperature profile for these parameters is shown in Figure A.1.

The temperature field in the solid phase described by Eq. A.5 is aside from constant factors identical to the temperature field in Eq. A.2 where only one phase was considered. The inclusion of latent heat does therefore not alter the qualitative time and space dependence of the temperature field. As in the case of no latent heat, we therefore expect the striae height, s, to increase with the distance from the cooled surfaces.

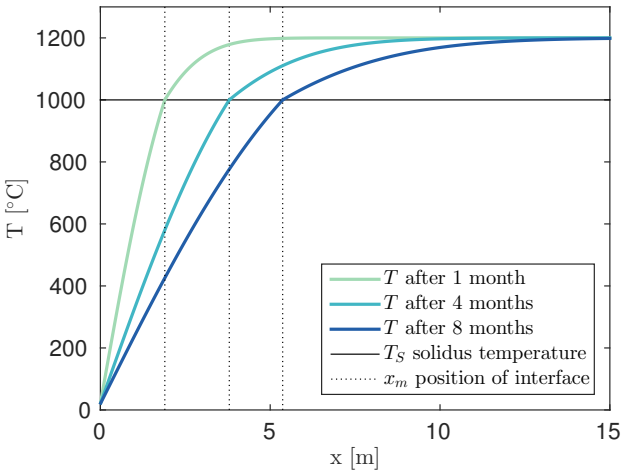

Figure A.1: Example of a temperature field resulting from pure diffusive heat transport when considering the release of latent heat at the solidification front. The temperature field is depicted at three different times, $t = 1, 4$ and 8 months, together with the position of the solidification front $x_m(t)$. The parameters described in the text with $\delta_l = \delta_s = 0.74$ are used.

A.2 NUMERICAL SIMULATIONS

For convenience, the description of the numerical simulations of columnar jointing given in Appendix B-C of Christensen et al. [3] is reproduced in this section.

A.2.1 *Discrete element simulations*

To model the cracking of an elastic medium, we use a discrete element method with nodes arranged in a cubic lattice with a lattice constant L^0. The nodes are interacting with their nearest-neighbors (NN) and next-nearest-neighbors (NNN) through Hookean springs with spring constants k_1 and k_2 for NNs and NNNs, respectively. The spring connecting the nodes i and j has an equilibrium length L_{ij}^{eq} and holds an elastic energy quadratic in the deviation from the equilibrium length,

$$U_{ij} = \frac{1}{2} k_{ij} (L_{ij} - L_{ij}^{eq})^2 \tag{A.9}$$

where $\mathbf{x}_i$ denotes the position of the i'th node and $L_{ij} = |\mathbf{x}_i - \mathbf{x}_j|$. The total energy of the system is given by the sum over all springs $U^{tot} = \sum U_{ij}$. The elasticity tensor corresponding to these interactions can be written in the form [22]:

$$C_{iiii} = (k_1 + 2k_2)/L^0 \quad C_{iijj} = C_{ijji} = C_{ijij} = k_2/L^0. \tag{A.10}$$

The thermal contraction of the system is modelled by changing the local equilibrium distance between the nodes. Like in the previous section, we shall consider a contraction front on the form of Eq. 2.2:

$$L_{ij}^{eq}(X, X_0) = L_{ij}^0 \left[1 + \alpha_T \Delta T \left(1 - e^{-\frac{X - X_0}{w}} \right) \theta (X - X_0) - \alpha_T \Delta T \right] \tag{A.11}$$

where $X_0 = vt = \frac{D}{w} t$ is the position of the temperature front, which moves through the system with time. Since elastic relaxation happens many orders of magnitude faster than thermal relaxation, the simulations proceed by advancing the contraction front a length dX_0, relaxing the system to elastostatic equilibrium, and repeating the process. The value of dX_0 does not affect the resulting fracture pattern. The state of elastostatic equilibrium or force balance is reached by minimizing the elastic energy, i.e. finding the lattice configuration for which $\nabla U = \nabla \sum U_{ij} = 0$. To that end, we apply a conjugate gradient method in the multidimensional configuration space. In the simulations, we use a failure criterion where an elastic bond in the lattice is broken when it is strained, ϵ_{ij}, beyond a critical strain ϵ_c:

$$\epsilon_{ij} > \epsilon_c. \tag{A.12}$$

With this threshold, bonds do not break during compression, i.e. the fractures forming the columnar joints will mostly grow at the trailing edge of the contraction front. Note, that while this asymmetry in the fracture criterion have little impact on the morphology of the steady state patterns, it may influence the fracture patterns formed close to the boundary of the system, i.e. where the front is initiated.

If more than one bond is strained beyond the critical level, the bond with the highest strain is broken and the lattice is relaxed to the new state of elastostatic equilibrium. We then check whether other bonds still exceed the critical stress. If a bond still exceeds the critical stress the process is repeated until no such bond exists and then finally we advance the contraction front by a small increment, dX_0. In that way, bonds are broken one-by-one until none of them exceeds the critical strain.

Note that in the simulations the temperature profile starts out with the steady state shape and therefore the initial cracks nucleating at the surface of the simulation system might not have any resemblance to the columns close to the cooling surface in real system. After a transient dynamics over a length of approximately $2w$, the cracks in the simulations form a regular polygonal pattern equivalent to the columnar joints. An example of a simulation is shown in Figure 2.7. When the regular polygonal crack pattern has formed, then the average column diameter $\langle \ell \rangle$ is measured. From this measurement, the Péclet number $Pe = \langle \ell \rangle / w$ for the simulation can be determined.

The fracture criterion $K_I = K_{I,c}$ given in Eq. 2.6 is in the simulations implemented through a critical strain. The dimensionless crit-

SIMULATION PARAMETER	VALUE
Poisson's ratio	$\nu_{pois} = 0.2$
Critical strain	$\epsilon_c \in [0.07, 2.60] \cdot 10^{-2}$
Maximal contraction	$\alpha_T \Delta T \in [0.01, 0.04]$
Dim.less. critical stress intensity factor[1]a	$\kappa_{I,c} = \frac{\epsilon_c}{\alpha_T \Delta T}$
Temperature front width	$w \in [1, 24]$

Table A.1: List of simulation parameters used in the discrete element simulations. In Figure 2.9 the value of $\kappa_{I,c}$ has been multiplied with $(1 - \nu_{pois})$ to make it comparable with the scaling function derived for 2D.

ical stress intensity factor is related to the critical strain as: $\kappa_{I,c} = K_{I,c}/(E\alpha_T \Delta T\sqrt{b}) = \epsilon_c/(\alpha_T \Delta T)$. This should not affect the above observations.

A.2.2 *Finite element simulations*

The material undergoing cooling is approximated by a box $[0, 4] \times [0, 1] \times [0, 1]$ with periodic boundary conditions applied on the faces parallel to the X-axis. The computational domain is finely discretized using tetrahedral elements (4 million tetrahedra). We assume the material to be isotropic and Cauchy elastic in the simulation, with the Young's modulus E and Poisson ratio $\nu_{pois} = 0.25$. The assumption of small displacements is valid in the context of columnar joint formation and the elasticity model is appropriate for simulating infinite systems.

We use the von Mises yield criterion, which states that failure occurs when the von Mises stress, σ_M, exceeds the material's yield strength, σ_c, chosen in simulation to be equal $\sigma_c = 0.01E$. We use a standard, linear Galerkin method to discretize the constitutive equation.

The propagating temperature front and corresponding thermal contraction are modelled as a body force:

$$\beta(X, X_0) = \alpha_T \Delta T\left(1 - \exp^{-(X - X_0)/w}\right)\theta(X - X_0) - \alpha_T \Delta T \quad \text{(A.13)}$$

where the maximum contraction is $\alpha_T \Delta T = 0.2$, the contraction front is located at $X_0 = vt = \frac{D}{w}t$ and the slope $1/w$ varies between 12 and 18. The simulation method at each time step advances the contraction front a step dX_0, updates the equilibrium von Mises stress values, and proceeds to fracture resolution. The fracture resolution is performed by finding the element with the maximum von Mises stress exceeding σ_c and removing it from the computational mesh (by labeling it as air). This is followed by reassembling the stiffness matrix and re-

SIMULATION PARAMETER	VALUE
Poisson's ratio	$\nu_{pois} = 0.25$
Tensile strength	$\sigma_c = 0.01E$
Maximal contraction	$\alpha_T \Delta T = 0.02$
Dim.less. critical stress intensity factor	$\kappa_{I,c} = \frac{\sigma_c}{E\alpha_T\Delta T} = 0.5$
Temperature front width	$w \in [1/18, 1/12]$

Table A.2: List of simulation parameters used in the finite element simulations. In Figure 2.9 the value of $\kappa_{I,c}$ has been multiplied with $(1-\nu_{pois})$ to make it comparable with the scaling function derived for 2D.

equilibrating the system. Those two steps are then repeated as long as there are elements with $\sigma^M > \sigma_c$ in the mesh. Re-equilibration, which amounts to solving the constitutive equations with a new stiffness matrix, is a computationally intensive process. Hence, in order to improve the method's performance we introduce two simplifications:

- System relaxation in the fracture resolution step is performed on a submesh composed of elements lying in the X-distance 0.1 from the temperature front (which is equivalent to treating the excluded region as fluid).
- Instead of only removing a single element at a time, all elements whose von Mises stress are greater than $\gamma\sigma_c$, $\gamma > 1$ are all removed at once, where γ is chosen in a way that it does not affect the resulting fracture pattern (determined in our simulation to be $\gamma = 1.1$).

The resulting set of removed tetrahedra displayed in Figure A.2 gives a representation of the columnar fracturing pattern, and can be used to measure the typical column diameter $\langle \ell \rangle$. The FEM results for pairs of $(Pe, \kappa_{I,c})$ obtained for fixed w and $\kappa_{I,c} = K_{I,c}/(E\alpha_T\Delta T\sqrt{b}) = \sigma_c/(E\alpha_T\Delta T)$ are in agreement with the discrete element simulation results, see Figure 2.9. In the figure, $\kappa_{I,c}$ is multiplied with $(1-\nu_{pois})$ to be comparable with the scaling function which is derived for 2D.

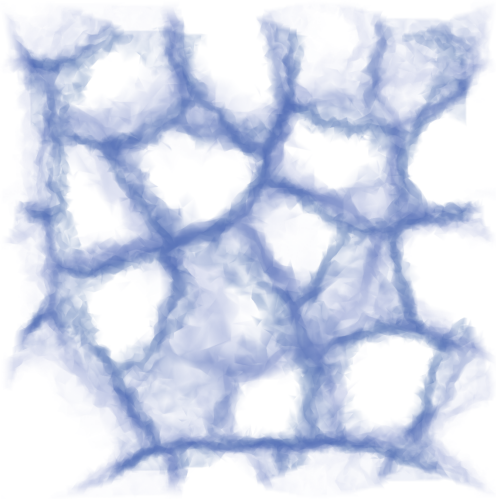

Figure A.2: **Example of the resulting fracture network** in a finite element simulation of columnar jointing for $w = 1/15$ and the parameters displayed in Table A.2.

B

APPENDIX: COLLECTIVE DYNAMICS AND DIVISION PROCESSES IN TISSUE

B.1 EXPERIMENTS ON EPITHELIAL AND ENDOTHELIAL TISSUES

The experiments on confluent monolayers of epithelial and endothelial cells used in this thesis, were performed by Lene Oddershedes lab at the Niels Bohr Institute. The data on epithelial cells have previously been published in West et al. [2] and the data on endothelial cells in Rossen et al. [46]. Details of the cell culturing and data analysis can be found in these two references.

B.1.1 *Epithelial cells*

Four breast cancer cell lines, listed in Table 3.1 of the main text, were considered. The human non-invasive MCF7 cells show an epithelial-like round shape, whereas the invasive human MDA-MB-231 cells are elongated and mesenchymal-like. The picture is turned around for the murine cells, where the non-invasive 67NR cells show an elongated shape, and the invasive 4T1 cells are round. The cells all have a characteristic size of about 20 µm.

Each cell type was seeded and cultured until a confluent mono layer was obtained after approximately 24 hours. The mono-layers were imaged in phase-contrast microscopy with an image taken every 2 minutes. The image sequences were analyzed with Particle Image Velocimetry (PIV) [127] to obtain the time evolution of the velocity fields.

The averaged time series of cell division displayed in Figure 3.8 of the main text were obtained by:

1. Manually identifying a dividing cell with no other dividing cells being closer than 150 µm.
2. Centering the dividing cell in a 300×300 µm frame.
3. Rotating the frame such that the daughter cells move horizontally away from the division site.
4. Taking the average of the velocity fields for at least 30 such centered and rotated events.

B.1.2 *Endothelial cells*

The human umbilical vein endothelial cells (HUVEC) were seeded and cultured until a confluent mono layer was obtained after approximately 3 days. The mono-layers were imaged in phase-contrast microscopy with an image taken every 10 minutes. The image sequences were analyzed with Particle Image Velocimetry (PIV) to obtain the time evolution of the velocity fields. The HUVEC cells have a characteristic size of about 40 μm.

B.2 CONVECTED DERIVATIVES

The physical laws governing the behavior of a material should not depend on the observer. In other words, constitutive equations for material rheology should be material frame indifferent (objective), as we do not expect stress to develop in a body, just because we run in a circle around it [128]. Note, that the frame indifference apply to any moving frame (Euclidean), not only frames which move with constant translation (Galilean).

B.2.1 *Objective vectors and tensors*

Let us consider observer A to be at rest. By $\mathbf{x}$ we denote the coordinates of a material particle as observed by A. The second observer B rotates and translates relative to observer A, and sees the same material particle perform the motion:

$$\hat{\mathbf{x}} = R(t)\mathbf{x} + \mathbf{x}_0(t) + \mathbf{x}, \tag{B.1}$$

where $R(t)$ is a rotation matrix and $\mathbf{x}_0(t)$ characterizes the translational motion. I.e. the mapping from $\mathbf{x}$ to $\hat{\mathbf{x}}$ is an Euclidean transformation. If the rotation is fixed in time $R(t) = R_0$ and the translational velocity is constant plus a shift of origin $\mathbf{x}_0(t) = \mathbf{v}_0 t + \mathbf{a}$, then the transformation is Galilean.

An Euclidean objective vector $\mathbf{w}$ and tensor τ transforms as:

$$\hat{\mathbf{w}} = R(t)\,\mathbf{w} \tag{B.2}$$

$$\hat{\tau} = R(t)\,\tau\,R^{T}(t). \tag{B.3}$$

Let us denote the material derivative $(\partial_t + \mathbf{v}\cdot\nabla)$ by an overline dot. The velocity gradient $\nabla\mathbf{v}$ is an example of a non-objective tensor [128]:

$$\hat{\nabla}\hat{\mathbf{v}} = R(t)\,\nabla\mathbf{v}\,R(t)^{T} + \dot{R}(t)\,R^{T}(t) \tag{B.4}$$

due to the term marked with blue, whereas the strain rate tensor $\gamma = \frac{1}{2}(\nabla \mathbf{v} + (\nabla \mathbf{v})^T)$ is objective:

$$\begin{aligned}
\hat{\gamma} &= \frac{1}{2}(\hat{\nabla}\hat{\mathbf{v}} + (\hat{\nabla}\hat{\mathbf{v}})^T) \\
&= R(t)\left[\frac{1}{2}(\nabla \mathbf{v} + (\nabla \mathbf{v})^T)\right] R(t)^T + \frac{1}{2}\left[\dot{R}(t)\, R^T(t) + R(t)\, \dot{R}^T(t)\right] \\
&= R(t)\,\gamma\, R(t)^T + \frac{1}{2}\overbrace{\dot{R}(t)R^T(t)} \\
&= R(t)\,\gamma\, R(t)^T, \qquad \text{(B.5)}
\end{aligned}$$

since for rotation matrices, $R(t)R^T(t) = I$, where I is the identity matrix and its material derivative vanish $\dot{I} = 0$.

However, even though a quantity is objective, its material derivative is not in general objective. The material derivatives of the objective quantities $\mathbf{w}$ and $\boldsymbol{\tau}$ transform as:

$$\dot{\hat{\mathbf{w}}} = R(t)(t)\,\dot{\mathbf{w}} + \dot{R}(t)\,\mathbf{w} \qquad \text{(B.6)}$$

$$\dot{\hat{\tau}} = R(t)\,\dot{\tau}\,R^T(t) + \dot{R}(t)\,\tau\,R^T(t) + R(t)\,\tau\,\dot{R}^T(t) \qquad \text{(B.7)}$$

and the blue parts of the equations are in excess, leading to the conclusion, that $\dot{\mathbf{w}}$ and $\dot{\tau}$ are not objective. For the constitutive equation to be objective, we demand that it is only comprised of objective quantities such as the strain rate tensor and objective time derivatives, which we still have to identify.

B.2.2 *Objective time derivatives*

Let us define the vorticity tensor:

$$\Omega = \frac{1}{2}(\nabla \mathbf{v} - (\nabla \mathbf{v})^T) \qquad \text{(B.8)}$$

which is not objective and transforms as [128]:

$$\hat{\Omega} = R(t)\,\Omega\,R^T(t) + \dot{R}(t)\,R^T(t). \qquad \text{(B.9)}$$

We can then define the Gordon-Schowalters family of convected derivatives for objective tensors τ:

$$\frac{\mathcal{D}_a \tau}{\mathcal{D}t} = \dot{\tau} - \Omega\tau + \tau\Omega - a(\gamma\tau + \tau\gamma), \qquad \text{(B.10)}$$

where the derivative is parametrized by the scalar a. This family of tensor derivatives is objective:

$$\begin{aligned}
\frac{\mathcal{D}_a\hat{\tau}}{\mathcal{D}t} &= \dot{\hat{\tau}} - \hat{\Omega}\hat{\tau} + \hat{\tau}\hat{\Omega} - a(\hat{\gamma}\hat{\tau} + \hat{\tau}\hat{\gamma}) \\
&= R(t)\,\dot{\tau}\,R^T(t) + \dot{R}(t)\,\tau\,R^T(t) + R(t)\,\tau\,\dot{R}^T(t) \\
&\quad - \left[R(t)\,\Omega\,R^T(t) + \dot{R}(t)\,R^T(t)\right]R(t)\,\tau\,R^T(t) \\
&\quad + R(t)\,\tau\,R^T(t)\left[R(t)\,\Omega\,R^T(t) + \dot{R}(t)\,R^T(t)\right] \\
&\quad - a\left\{R(t)\,\gamma\,R^T(t)\;R(t)\,\tau\,R^T(t) + R(t)\,\tau\,R^T(t)\;R(t)\,\gamma\,R^T(t)\right\} \\
&= R(t)\,\dot{\tau}\,R^T(t) + \dot{R}(t)\,\tau\,R^T(t) + R(t)\,\tau\,\dot{R}^T(t) \\
&\quad - R(t)\,\Omega\,\tau\,R^T(t) - \dot{R}(t)\,\tau\,R^T(t) \\
&\quad + R(t)\,\tau\,\Omega\,R^T(t) + R(t)\,\tau\,R^T(t)\,\dot{R}(t)\,R^T(t) \\
&\quad - aR(t)\,\{\gamma\tau + \tau\gamma\}\,R^T(t) \\
&= R(t)\,\dot{\tau}\,R^T(t) - R(t)\,\Omega\,\tau\,R^T(t) + R(t)\,\tau\,\Omega\,R^T(t) - aR(t)\,\{\gamma\tau + \tau\gamma\}\,R^T(t) \\
&= R(t)\left(\frac{\mathcal{D}_a\tau}{\mathcal{D}t}\right)R^T(t) \qquad \text{(B.11)}
\end{aligned}$$

where we have used that $R(t)R^T(t) = I$, such that $\dot{R}(t)R^T(t) = -R(t)\dot{R}^T(t)$. The scalar parameter a interpolates between the upper and lower convected derivatives. The last term of the Gordon-Schowalters derivative Eq. B.10, proportional to a, describes the effect of the fluid deformation. For $a = 0$, we obtain the Jaumann derivative, which describes the time derivative with respect to a frame that rotates with the flow. For $a = 1$ we obtain the upper convected derivative and for $a = -1$ we obtain the lower convected derivative, which describes the effect of respectively convecting the contravariant and covariant basis vectors of the coordinate system with the flow [129].

B.3 NUMERICAL SIMULATIONS

The proposed model for tissue dynamics is described by the equation system (introduced in Chapter 3, Eq. 3.1-3.5):

$$0 = -\frac{1}{\rho}\nabla p + \frac{1}{\rho}\nabla\cdot\sigma - \alpha\hat{\mathbf{v}} + \mathbf{m} \qquad \text{(B.12)}$$

$$\sigma + \lambda_1\frac{\partial\sigma}{\partial t} = 2\eta_0\left(\gamma + \lambda_2\frac{\partial\gamma}{\partial t}\right) \qquad \text{(B.13)}$$

$$0 = \nabla\cdot\mathbf{v} \qquad \text{(B.14)}$$

$$\frac{\partial\mathbf{m}}{\partial t} + (\mathbf{v}\cdot\nabla)\mathbf{m} = -\frac{1}{\lambda_m}\mathbf{m} + \boldsymbol{\phi}(\mathbf{x},t) \qquad \text{(B.15)}$$

$$\boldsymbol{\phi}(\mathbf{x},t) = \frac{1}{2\pi\ell_m^2}\int\xi(\mathbf{x}',t)\exp\left(-\frac{|\mathbf{x}-\mathbf{x}'|^2}{2\ell_m^2}\right)d\mathbf{x}' \qquad \text{(B.16)}$$

$$\left\langle\xi_i(\mathbf{x},t)\xi_j(\mathbf{x}',t')\right\rangle = \beta_m\delta^{(2)}(\mathbf{x}-\mathbf{x}')\delta(t-t')\delta_{ij}. \qquad \text{(B.17)}$$

Note, that the upper convected derivatives in Eq. 3.2 have been replaced by partial time derivatives in the corresponding Eq. B.13. This

replacement can be justified, since the viscoelastic time scale is much smaller than the deformation time scale in the cell experiments. To clarify this point, consider the upper convected derivative of a tensor ψ:

$$\overset{\nabla}{\psi} = \frac{\partial \psi}{\partial t} + (\mathbf{v}\cdot\nabla)\psi - \left[\psi\cdot(\nabla\mathbf{v}) + (\nabla\mathbf{v})^{T}\cdot\psi\right]. \tag{B.18}$$

The upper convected derivative in Eq. B.18 can be cast in dimensionless form, if we define the characteristic time scale t_ψ on which ψ changes, the characteristic flow velocity U_v and the characteristic flow length scale L_v. Denoting dimensionless quantities by an apostrophe, the dimensionless form of the upper convected derivative is:

$$\overset{\nabla'}{\psi} = \frac{\partial \psi}{\partial t'} + \frac{t_\psi U_v}{L_v}\left\{(\mathbf{v}'\cdot\nabla')\psi - \left[\psi\cdot(\nabla'\mathbf{v}') + (\nabla'\mathbf{v}')^{T}\cdot\psi\right]\right\}. \tag{B.19}$$

When the velocity gradients, characterized by U_v/L_v, are small compared to the characteristic time t_ψ, then the upper convected derivative reduces to a partial time derivative. This is the case for the considered experiments, where the cells have a characteristic flow velocity $U_v \sim 1\ \mu m/min$ and a characteristic size of $L_v \sim 20\ \mu m$. The characteristic viscoelastic time can be estimated as the retardation time $t_\psi \sim \lambda_2$ obtained from the cell division process (Section 3.3). Thus, the quantity $(t_\psi U_v/L_v) \sim 0.05$ is small and we replace the upper convected derivative by a partial time derivative.

B.3.1 *Dimensionless form*

The governing equations are cast in a dimensionless form by scaling with the motility length ℓ_m, the time scale λ_m and the total viscosity η_0:

$$\nabla p = \nabla\cdot\sigma - a_\alpha\hat{\mathbf{v}} + \mathbf{m} \tag{B.20}$$

$$\sigma + a_1\frac{\partial\sigma}{\partial t} = 2\left(\gamma + a_2\frac{\partial\gamma}{\partial t}\right) \tag{B.21}$$

$$0 = \nabla\cdot\mathbf{v} \tag{B.22}$$

$$\frac{\partial\mathbf{m}}{\partial t} + (\mathbf{v}\cdot\nabla)\mathbf{m} = -\mathbf{m} + \boldsymbol{\phi}(\mathbf{x},t) \tag{B.23}$$

$$\boldsymbol{\phi}(\mathbf{x},t) = \frac{1}{2\pi}\int \boldsymbol{\xi}(\mathbf{x}',t)\exp\left(-\frac{|\mathbf{x}-\mathbf{x}'|^2}{2}\right)d\mathbf{x}' \tag{B.24}$$

$$\left\langle \xi_i(\mathbf{x},t)\xi_j(\mathbf{x}',t')\right\rangle = a_\beta\delta^{(2)}(\mathbf{x}-\mathbf{x}')\delta(t-t')\delta_{ij}. \tag{B.25}$$

All quantities in Eq. B.20-B.25 are now dimensionless, and we have defined the four dimensionless control parameters:

$$a_1 = \frac{\lambda_1}{\lambda_m} \qquad a_2 = \frac{\lambda_2}{\lambda_m} \qquad a_\alpha = \frac{\rho}{\eta_0}\ell_m\lambda_m\alpha \qquad a_\beta = \left(\frac{\rho}{\eta_0}\right)^2\lambda_m^3\beta_m.$$

CELL LINE	MEAN SPEED v_0 [μm/min]	CORR. LENGTH ℓ_0 [μm]
4T1	0.27 ± 0.06	25.8 ± 0.9
67NR	0.13 ± 0.03	26.5 ± 1.1
MCF7	0.23 ± 0.02	19.6 ± 0.7
MDA-MB-231	0.7 ± 0.2	13.7 ± 0.4
HUVEC	0.5 ± 0.1	28.0 ± 0.1

Table B.1: **Measured characteristics of experimental velocity fields in bulk experiments.** The correlation length ℓ_0 was found by fitting a single exponential $C_{vv}(r) = e^{-r/\ell_0}$ to the spatial correlation functions displayed in Figure 3.5.

B.3.2 *Numerical scheme*

The model given by Eq. B.20-B.25 was simulated numerically in a periodic two-dimensional box of 256×256 grid points using a pseudo-spectral method. The Fast Fourier Transform algorithm was used to perform Fourier- and inverse Fourier transforms, and non-linear terms were evaluated in real space. The exponential time differencing scheme [130] was used to perform the time integration of the stress tensor and the noise term. The velocity field and the pressure was found by a relaxation procedure in each time step.

B.3.3 *Fitting procedure*

For each of the five cell lines, the experimental speed distribution $P(v)$, the spatial velocity correlation function $C_{vv}(r)$ and the temporal velocity correlation function $C_{vv}(t)$ were calculated from the velocity fields obtained by PIV analysis. Also the mean speed v_0 and the correlation length ℓ_0 were calculated for the experiments (Table B.1). From these quantities the normalized experimental speed distribution $P(w = v/v_0)$, the spatial velocity correlation function $C_{vv}(z = r/\ell_0)$ and the temporal velocity correlation function $C_{vv}(s = t/(v_0/\ell_0))$ displayed in Figure 3.5 were found.

The model was fitted to the experiments, by varying the four control parameters $a_1, a_2, a_\alpha, a_\beta$, calculating $P(w), C_{vv}(z)$ and $C_{vv}(s)$ for each simulation, and choosing the control parameter set, that minimized the chi squared between the experimental and simulated $P(w), C_{vv}(z)$ and $C_{vv}(s)$.

When the control parameters $a_1, a_2, a_\alpha, a_\beta$ have been fitted, the value of the motility time scale λ_m and length scale ℓ_m can be deter-

CELL LINE	λ_1 (min)	λ_2 (min)	λ_m (min)	ℓ_m (μm)	$\alpha\left(\frac{\rho}{\eta_0}\right)$ $(\mu m \cdot min)^{-1}$	$\beta_m\left(\frac{\rho}{\eta_0}\right)^2$ $(min)^{-3}$
4T1	1.6	0.4	7.8	10	0.002	0.003
67NR	2.9	0.7	7.1	12	0.001	0.001
MCF7	1.2	0.3	3.0	9	0.003	0.010
MDA-MB-231	2.2	0.2	4.3	7	0.015	0.125
HUVEC	1.6	0.4	7.8	10	0.002	0.003

Table B.2: **Fitted parameters for bulk cell motion.** The viscosity and density have not been measured, and α, β are therefore given as $\alpha\,(\rho/\eta_0)$ and $\beta_m\,(\rho/\eta_0)^2$ respectively.

mined from the mean speeds and correlation lengths of experiments (ℓ_0, v_0) and simulations $(\ell_0^{sim}, v_0^{sim})$:

$$\ell_m = \frac{\ell_0}{\ell_0^{sim}} \qquad \lambda_m = \frac{v_0^{sim}}{v_0}\ell_m.$$

The remaining four physical parameters can then be found from the dimensionless control parameters resulting from the fits:

$$\lambda_1 = \lambda_m a_1 \qquad \lambda_2 = \lambda_m a_2 \qquad \alpha = \left(\frac{\eta_0}{\rho}\right)\frac{a_\alpha}{\lambda_m \ell_m} \qquad \beta = \left(\frac{\eta_0}{\rho}\right)^2 \frac{a_\beta}{\lambda_m^3}$$

The parameters obtained by fitting to the experimental data are displayed in Table B.2. With these parameters, the periodic two-dimensional domain corresponded to a box of length $\sim 200\,\mu m$ in physical units. The time step was $\sim 0.01\,min$ in physical units.

C

APPENDIX: COUPLING BETWEEN SUBSTRATE CURVATURE AND TEXTURE OF CO-BLOCK POLYMERS

C.1 FUNCTIONAL DERIVATIVE OF THE FREE ENERGY

If $G(\psi)$ is a functional of ψ, then the functional derivative $\delta G/\delta\psi$ can be identified as:

$$\left.\frac{dG(\psi(\tilde{\mathbf{p}})+\epsilon\,\phi(\tilde{\mathbf{p}}))}{d\epsilon}\right|_{\epsilon=0} = \int d\tilde{A}\ \frac{\delta G}{\delta\psi}\phi(\tilde{\mathbf{p}}), \tag{C.1}$$

where $\phi(\tilde{\mathbf{p}})$ is an arbitrary function and $\epsilon\,\phi(\tilde{\mathbf{p}})$ is the variation of $\psi(\tilde{\mathbf{p}})$. The functional derivative of the free energy is:

$$\frac{\delta f}{\delta\psi} = \frac{h\tilde{A}}{V}\left[\frac{\delta f_{\tilde{S}}}{\delta\psi}+\frac{\delta k_{\tilde{S}}}{\delta\psi}\right], \tag{C.2}$$

where:

$$\tilde{A}\frac{\delta f_{\tilde{S}}}{\delta\psi} = \tau\psi+\psi^3+4\tilde{\nabla}^2\psi+4\tilde{\nabla}^4\psi \tag{C.3}$$

$$\tilde{A}\frac{\delta k_{\tilde{S}}}{\delta\psi} = \frac{h^2}{12}\left[2\frac{\delta D_2}{\delta\psi}-2\frac{\delta C_2}{\delta\psi}+\tau K\psi+K\psi^3\right]. \tag{C.4}$$

Here, we have considered surfaces with no border and defined the functionals:

$$C_2(\psi) = \int d\tilde{A}\ c_2(\psi)$$

$$D_2(\psi) = \int d\tilde{A}\ d_2(\psi).$$

The functional derivative of C_2 is identified from:

$$\begin{aligned}\left.\frac{dC_2(\psi(\tilde{\mathbf{p}})+\epsilon\,\phi(\tilde{\mathbf{p}}))}{d\epsilon}\right|_{\epsilon=0} &= \int d\tilde{A}\Big[2HK^{ij}(\tilde{\nabla}_i\psi\tilde{\nabla}_j\phi+\tilde{\nabla}_j\psi\tilde{\nabla}_i\phi)\\ &\qquad -2K(\tilde{\nabla}_i\psi\tilde{\nabla}^i\phi+\tilde{\nabla}^i\psi\tilde{\nabla}_i\phi)\Big]\\ &= \int d\tilde{A}\Big[4HK^{ij}\tilde{\nabla}_i\psi\tilde{\nabla}_j\phi-4K(\tilde{\nabla}^i\psi\tilde{\nabla}_i\phi)\Big]\\ &= \int d\tilde{A}\Big[-4HK^{ij}\tilde{\nabla}_j\tilde{\nabla}_i\psi+4K\tilde{\nabla}_i\tilde{\nabla}^i\psi\Big]\phi,\end{aligned}$$

using the fact that the curvature tensor K_{ij} and the metric g_{ij} are symmetric as well as integration by parts. (For a surface with no boundary, Stokes theorem yields $\int d\tilde{A}\ \nabla_i(qw^i)=0$ where q is a scalar and w^i a vector field. Using that the covariant derivative obeys the product

rule we get $\int d\tilde{A}\ q\nabla_i w^i = -\int d\tilde{A}\ w^i \nabla_i q$). The functional derivative of C_2 is:

$$\frac{\delta C_2}{\delta \psi} = -4HK^{ij}\tilde{\nabla}_i\tilde{\nabla}_j\psi + 4K\tilde{\nabla}^2\psi. \tag{C.5}$$

Following the same procedure, we get:

$$\begin{aligned}\frac{\delta D_2}{\delta \psi} = {} & 8K^{lm}K^{ij}\tilde{\nabla}_l\tilde{\nabla}_m\tilde{\nabla}_i\tilde{\nabla}_j\psi - 10K\tilde{\nabla}^4\psi \\ & + 4H\Big[\tilde{\nabla}^2(K^{ij}\tilde{\nabla}_i\tilde{\nabla}_j\psi) + K^{lm}\tilde{\nabla}_m\tilde{\nabla}_l(\tilde{\nabla}^2\psi)\Big].\end{aligned}$$

The functional derivative of the free energy density is in total:

$$\frac{\delta f}{\delta \psi} = \frac{h}{V}\left[\left(1 + \frac{h^2}{12}K\right)(\tau\psi + \psi^3) + 4\tilde{\nabla}^2\psi + 4\tilde{\nabla}^4\psi + \frac{h^2}{12}\left(2\frac{\delta D_2}{\delta \psi} - 2\frac{\delta C_2}{\delta \psi}\right)\right]. \tag{C.6}$$

REFERENCES

[1] Amalie Christensen, Christophe Raufaste, Marek Misztal, Frank Celestini, Maria Guidi, Clive Ellegaard, and Joachim Mathiesen. "Scale selection in columnar jointing: Insights from experiments on cooling stearic acid and numerical simulations." In: *Journal of Geophysical Research: Solid Earth* (2016).

[2] Ann-Katrine Vransøe West, Lena Wullkopf, Amalie Christensen, Natascha Leijnse, Jens Tarp, Joachim Mathiesen, Janine Terra Erler, and Lene Broeng Oddershede. "Dynamics of cancerous tissue correlates with invasiveness." In: *Scientific Reports* (2017).

[3] Amalie Christensen, Ann-Katrine Vransøe West, Lena Wullkopf, Janine Terra Erler, Lene Broeng Oddershede, and Joachim Mathiesen. "Quantifying Cell Motility and Division Processes in Tissue by a Mechanical Continuum Model." In: *Under review in PLOS Computational Biology* (2017).

[4] Petr Broz. *Giant's Causeway, Northern Ireland. Hexagonal basalts.* 2010. URL: https://commons.wikimedia.org/wiki/File:Giant's_Causeway_%2813%29.JPG.

[5] Ann-Katrine Vransøe West. *Epithelial cancer cells.* Pictures of experiments performed in Lene Oddershede's Lab. 2016.

[6] Ward A Lopes and Heinrich M Jaeger. "Hierarchical self-assembly of metal nanostructures on diblock copolymer scaffolds." In: *Nature* 414.6865 (2001), pp. 735–738.

[7] Marek Misztal. *Columnar jointing at Svartifoss, Iceland*.

[8] Minghong. *Hexagonal volcanic tuffs at East Dam of High Island Reservoir.* 2008. URL: https://www.flickr.com/photos/minghong/2780061894/.

[9] L. Goehring, L. Mahadevan, and W. Moris. *Regular prismatic columns in corn starch with a milimeter scale.* Picture adapted from L. Goehring et al. "Nonequilibrium scale selection mechanism for columnar jointing." In: Proceedings of the National Academy of Sciences 106.2 (Jan. 2009), pp. 387–392.

[10] Simon A. Kattenhorn and Conrad J. Schaefer. "Thermal–mechanical modeling of cooling history and fracture development in inflationary basalt lava flows." In: *Journal of Volcanology and Geothermal Research* 170.3–4 (Mar. 2008), pp. 181–197.

[11] György Hetényi, Benoît Taisne, Fanny Garel, Étienne Médard, Sonja Bosshard, and Hannes B. Mattsson. "Scales of columnar jointing in igneous rocks: field measurements and controlling factors." en. In: *Bulletin of Volcanology* 74.2 (Mar. 2012), pp. 457–482.

[12] J. C. Phillips, M. C. S. Humphreys, K. A. Daniels, R. J. Brown, and F. Witham. "The formation of columnar joints produced by cooling in basalt at Staffa, Scotland." en. In: *Bulletin of Volcanology* 75.6 (June 2013), pp. 1–17.

[13] Alan Spry. "The origin of columnar jointing, particularly in basalt flows." In: *Journal of the Geological Society of Australia* 8.2 (Jan. 1962), pp. 191–216.

[14] Michael P. Ryan and Charles G. Sammis. "The glass transition in basalt." en. In: *Journal of Geophysical Research: Solid Earth* 86.B10 (Oct. 1981), pp. 9519–9535.

[15] Atilla Aydin and James M. DeGraff. "Evolution of Polygonal Fracture Patterns in Lava Flows." In: *Science*. New Series 239.4839 (Jan. 1988), pp. 471–476.

[16] P. Budkewitsch. "Modelling the evolution of columnar joints." In: *Journal of Volcanology and Geothermal Research* 59.3 (1994), pp. 219–239.

[17] E. A. Jagla. "Maturation of crack patterns." In: *Physical Review E* 69.5 (May 2004), p. 056212.

[18] Martin Hofmann, Robert Anderssohn, Hans-Achim Bahr, Hans-Jürgen Weiß, and Jens Nellesen. "Why Hexagonal Basalt Columns?" In: *Physical Review Letters* 115.15 (Oct. 2015), p. 154301.

[19] James M. Degraff, Philip E. Long, and Atilla Aydin. "Use of joint-growth directions and rock textures to infer thermal regimes during solidification of basaltic lava flows." In: *Journal of Volcanology and Geothermal Research* 38.3–4 (Sept. 1989), pp. 309–324.

[20] L. Goehring and S. W. Morris. "Order and disorder in columnar joints." en. In: *EPL (Europhysics Letters)* 69.5 (Mar. 2005), p. 739.

[21] Yossi Cohen, Joachim Mathiesen, and Itamar Procaccia. "Drying patterns: Sensitivity to residual stresses." In: *Physical Review E* 79.4 (2009), p. 046109.

[22] Yoshinori Hayakawa. "Pattern selection of multicrack propagation in quenched crystals." In: *Physical Review E* 50.3 (Sept. 1994), R1748–R1751.

[23] Harry C. Hardee. "Solidification in Kilauea Iki lava lake." In: *Journal of Volcanology and Geothermal Research* 7.3–4 (May 1980), pp. 211–223.

[24] Dallas L. Peck and Takeshi Minakami. "The Formation of Columnar Joints in the Upper Part of Kilauean Lava Lakes, Hawaii." en. In: *Geological Society of America Bulletin* 79.9 (Sept. 1968), pp. 1151–1166.

[25] Lucas Goehring and Stephen W. Morris. "Scaling of columnar joints in basalt." en. In: *Journal of Geophysical Research: Solid Earth* 113.B10 (Oct. 2008), B10203.

[26] Kenneth A. Grossenbacher and Stephen M. McDuffie. "Conductive cooling of lava: columnar joint diameter and stria width as functions of cooling rate and thermal gradient." In: *Journal of Volcanology and Geothermal Research* 69.1–2 (Dec. 1995), pp. 95–103.

[27] Bernard Guy. "Comments on "Basalt columns: Large scale constitutional supercooling? by John Gilman (JVGR, 2009) and presentation of some new data [J. Volcanol. Geotherm. Res. 184 (2009), 347–350]." In: *Journal of Volcanology and Geothermal Research* 194.1–3 (July 2010), pp. 69–73.

[28] John J. Gilman. "Basalt columns: Large scale constitutional supercooling?" In: *Journal of Volcanology and Geothermal Research* 184.3–4 (July 2009), pp. 347–350.

[29] L. H. Kantha. "'Basalt fingers' – origin of columnar joints?" In: *Geological Magazine* 118.03 (May 1981), pp. 251–264.

[30] Marshall Reiter, Margaret W. Barroll, Jeffrie Minier, and Gerry Clarkson. "Thermo-mechanical model for incremental fracturing in cooling lava flows." In: *Tectonophysics* 142.2–4 (Nov. 1987), pp. 241–260.

[31] A. Toramaru and T. Matsumoto. "Columnar joint morphology and cooling rate: A starch-water mixture experiment." en. In: *Journal of Geophysical Research: Solid Earth* 109.B2 (Feb. 2004), B02205.

[32] Lucas Goehring, Stephen W. Morris, and Zhenquan Lin. "Experimental investigation of the scaling of columnar joints." In: *Physical Review E* 74.3 (Sept. 2006), p. 036115.

[33] Arianna Elizabeth Gleason. "Elasticity of Materials at High Pressure." PhD thesis. University of California, Berkeley, 2010.

[34] M. Marder. "Instability of a crack in a heated strip." In: *Physical Review E* 49.1 (Jan. 1994), R51–R54.

[35] Lucas Goehring, L. Mahadevan, and Stephen W. Morris. "Nonequilibrium scale selection mechanism for columnar jointing." In: *Proceedings of the National Academy of Sciences* 106.2 (Jan. 2009), pp. 387–392.

[36] Sriram Ramaswamy. "The Mechanics and Statistics of Active Matter." In: *Annual Review of Condensed Matter Physics* 1.1 (2010), pp. 323–345.

[37] M. C. Marchetti, J. F. Joanny, S. Ramaswamy, T. B. Liverpool, J. Prost, Madan Rao, and R. Aditi Simha. "Hydrodynamics of soft active matter." In: *Reviews of Modern Physics* 85.3 (July 2013), pp. 1143–1189.

[38] Christopher Dombrowski, Luis Cisneros, Sunita Chatkaew, Raymond E. Goldstein, and John O. Kessler. "Self-Concentration and Large-Scale Coherence in Bacterial Dynamics." In: *Physical Review Letters* 93.9 (Aug. 2004), p. 098103.

[39] Henricus H. Wensink, Jörn Dunkel, Sebastian Heidenreich, Knut Drescher, Raymond E. Goldstein, Hartmut Löwen, and Julia M. Yeomans. "Meso-scale turbulence in living fluids." en. In: *Proceedings of the National Academy of Sciences* 109.36 (Sept. 2012), pp. 14308–14313.

[40] Shuang Zhou, Andrey Sokolov, Oleg D. Lavrentovich, and Igor S. Aranson. "Living liquid crystals." en. In: *Proceedings of the National Academy of Sciences* 111.4 (Jan. 2014), pp. 1265–1270.

[41] Thomas E. Angelini, Edouard Hannezo, Xavier Trepat, Jeffrey J. Fredberg, and David A. Weitz. "Cell Migration Driven by Cooperative Substrate Deformation Patterns." In: *Physical Review Letters* 104.16 (Apr. 2010), p. 168104.

[42] Donald Macauley. *Starling Murmuration*. 2014. URL: https://www.flickr.com/photos/27770620@N02/15967110002/.

[43] Robin Hughes. *A "tornado" of schooling barracudas at Sanganeb Reef, Sudan.* 2007. URL: https://www.flickr.com/photos/robinhughes/404457553.

[44] Gregory Velicer and Juergen Bergen. *Liquid-crystalline order in a myxobacterial flock.* Picture adapted from M. C. Marchetti et al. "Hydrodynamics of soft active matter." In: Reviews of Modern Physics 85.3 (July 2013), pp. 1143–1189. 2013.

[45] M. Poujade, E. Grasland-Mongrain, A. Hertzog, J. Jouanneau, P. Chavrier, B. Ladoux, A. Buguin, and P. Silberzan. "Collective migration of an epithelial monolayer in response to a model wound." en. In: *Proceedings of the National Academy of Sciences* 104.41 (Oct. 2007), pp. 15988–15993.

[46] Ninna S. Rossen, Jens M. Tarp, Joachim Mathiesen, Mogens H. Jensen, and Lene B. Oddershede. "Long-range ordered vorticity patterns in living tissue induced by cell division." en. In: *Nature Communications* 5 (Dec. 2014), p. 5720.

[47] Xavier Serra-Picamal, Vito Conte, Romaric Vincent, Ester Anon, Dhananjay T. Tambe, Elsa Bazellieres, James P. Butler, Jeffrey J. Fredberg, and Xavier Trepat. "Mechanical waves during tissue expansion." en. In: *Nature Physics* 8.8 (Aug. 2012), pp. 628–634.

[48] Robert Weinberg. *The biology of cancer*. Garland science, 2013.

[49] Peter Friedl and Darren Gilmour. "Collective cell migration in morphogenesis, regeneration and cancer." In: *Nature Reviews Molecular Cell Biology* 10.7 (July 2009), pp. 445–457.

[50] Shengyu Yang, J. Jillian Zhang, and Xin-Yun Huang. "Orai1 and STIM1 Are Critical for Breast Tumor Cell Migration and Metastasis." In: *Cancer Cell* 15.2 (Feb. 2009), pp. 124–134.

[51] Xavier Trepat, Michael R. Wasserman, Thomas E. Angelini, Emil Millet, David A. Weitz, James P. Butler, and Jeffrey J. Fredberg. "Physical forces during collective cell migration." In: *Nature Physics* 5.6 (June 2009), pp. 426–430.

[52] Dhananjay T. Tambe et al. "Collective cell guidance by cooperative intercellular forces." en. In: *Nature Materials* 10.6 (June 2011), pp. 469–475.

[53] C. T. Lim, E. H. Zhou, and S. T. Quek. "Mechanical models for living cells—a review." In: *Journal of Biomechanics* 39.2 (2006), pp. 195–216.

[54] Karen E Kasza, Amy C Rowat, Jiayu Liu, Thomas E Angelini, Clifford P Brangwynne, Gijsje H Koenderink, and David A Weitz. "The cell as a material." In: *Current Opinion in Cell Biology*. Cell structure and dynamics 19.1 (Feb. 2007), pp. 101–107.

[55] Claude Verdier, Jocelyn Etienne, Alain Duperray, and Luigi Preziosi. "Review: Rheological properties of biological materials." In: *Comptes Rendus Physique*. Fluides complexes et biologiques 10.8 (Nov. 2009), pp. 790–811.

[56] Andrew R. Harris, Loic Peter, Julien Bellis, Buzz Baum, Alexandre J. Kabla, and Guillaume T. Charras. "Characterizing the mechanics of cultured cell monolayers." en. In: *Proceedings of the National Academy of Sciences* 109.41 (Oct. 2012), pp. 16449–16454.

[57] Karine Guevorkian, Marie-Josée Colbert, Mélanie Durth, Sylvie Dufour, and Françoise Brochard-Wyart. "Aspiration of Biological Viscoelastic Drops." In: *Physical Review Letters* 104.21 (May 2010), p. 218101.

[58] Gabor Forgacs, Ramsey A. Foty, Yinon Shafrir, and Malcolm S. Steinberg. "Viscoelastic Properties of Living Embryonic Tissues: a Quantitative Study." In: *Biophysical Journal* 74.5 (May 1998), pp. 2227–2234.

[59] Yue Wang and Michael F. Insana. "Viscoelastic Properties of Rodent Mammary Tumors Using Ultrasonic Shear-Wave Imaging." en. In: *Ultrasonic Imaging* 35.2 (Apr. 2013), pp. 126–145.

[60] Néstor Sepúlveda, Laurence Petitjean, Olivier Cochet, Erwan Grasland-Mongrain, Pascal Silberzan, and Vincent Hakim. "Collective Cell Motion in an Epithelial Sheet Can Be Quantitatively Described by a Stochastic Interacting Particle Model." In: *PLOS Comput Biol* 9.3 (Mar. 2013), e1002944.

[61] Pilhwa Lee and Charles W. Wolgemuth. "Crawling Cells Can Close Wounds without Purse Strings or Signaling." In: *PLOS Comput Biol* 7.3 (Mar. 2011), e1002007.

[62] Julia C. Arciero, Qi Mi, Maria F. Branca, David J. Hackam, and David Swigon. "Continuum Model of Collective Cell Migration in Wound Healing and Colony Expansion." In: *Biophysical Journal* 100.3 (Feb. 2011), pp. 535–543.

[63] Olivier Cochet-Escartin, Jonas Ranft, Pascal Silberzan, and Philippe Marcq. "Border Forces and Friction Control Epithelial Closure Dynamics." In: *Biophysical Journal* 106.1 (Jan. 2014), pp. 65–73.

[64] Jörg Galle, Markus Loeffler, and Dirk Drasdo. "Modeling the Effect of Deregulated Proliferation and Apoptosis on the Growth Dynamics of Epithelial Cell Populations In Vitro." In: *Biophysical Journal* 88.1 (Jan. 2005), pp. 62–75.

[65] Amin Doostmohammadi, Michael F. Adamer, Sumesh P. Thampi, and Julia M. Yeomans. "Stabilization of active matter by flow-vortex lattices and defect ordering." In: *Nature Communications* 7 (Feb. 2016), p. 10557.

[66] B. Szabó, G. J. Szöllösi, B. Gönci, Zs. Jurányi, D. Selmeczi, and Tamás Vicsek. "Phase transition in the collective migration of tissue cells: Experiment and model." In: *Physical Review E* 74.6 (Dec. 2006), p. 061908.

[67] Előd Méhes and Tamás Vicsek. "Collective motion of cells: from experiments to models." en. In: *Integr. Biol.* 6.9 (July 2014), pp. 831–854.

[68] Francois Graner and James A. Glazier. "Simulation of biological cell sorting using a two-dimensional extended Potts model." In: *Physical Review Letters* 69.13 (Sept. 1992), pp. 2013–2016.

[69] A. Szabó, R. Ünnep, E. Méhes, W. O. Twal, W. S. Argraves, Y. Cao, and A. Czirók. "Collective cell motion in endothelial monolayers." en. In: *Physical Biology* 7.4 (2010), p. 046007.

[70] Philipp J. Albert and Ulrich S. Schwarz. "Dynamics of Cell Ensembles on Adhesive Micropatterns: Bridging the Gap between Single Cell Spreading and Collective Cell Migration." In: *PLOS Comput Biol* 12.4 (Apr. 2016), e1004863.

[71] Reza Farhadifar, Jens-Christian Röper, Benoit Aigouy, Suzanne Eaton, and Frank Jülicher. "The Influence of Cell Mechanics, Cell-Cell Interactions, and Proliferation on Epithelial Packing." In: *Current Biology* 17.24 (Dec. 2007).

[72] Sebastian Aland, Haralambos Hatzikirou, John Lowengrub, and Axel Voigt. "A Mechanistic Collective Cell Model for Epithelial Colony Growth and Contact Inhibition." In: *Biophysical Journal* 109.7 (Oct. 2015), pp. 1347–1357.

[73] Thomas Bittig, Ortrud Wartlick, Anna Kicheva, Marcos Gonzalez-Gaitan, and Frank Jülicher. "Dynamics of anisotropic tissue growth." en. In: *New Journal of Physics* 10.6 (2008), p. 063001.

[74] Jonas Ranft, Markus Basan, Jens Elgeti, Jean-François Joanny, Jacques Prost, and Frank Jülicher. "Fluidization of tissues by cell division and apoptosis." en. In: *Proceedings of the National Academy of Sciences* 107.49 (Dec. 2010), pp. 20863–20868.

[75] Amin Doostmohammadi, Sumesh P. Thampi, Thuan B. Saw, Chwee T. Lim, Benoit Ladoux, and Julia M. Yeomans. "Celebrating Soft Matter's 10th Anniversary: Cell division: a source of active stress in cellular monolayers." en. In: *Soft Matter* 11.37 (2015), pp. 7328–7336.

[76] Michael H. Köpf and Len M. Pismen. "A continuum model of epithelial spreading." en. In: *Soft Matter* 9.14 (2013), p. 3727.

[77] Shiladitya Banerjee, Kazage J. C. Utuje, and M. Cristina Marchetti. "Propagating Stress Waves During Epithelial Expansion." In: *Physical Review Letters* 114.22 (June 2015), p. 228101.

[78] D. Marenduzzo, E. Orlandini, M. E. Cates, and J. M. Yeomans. "Steady-state hydrodynamic instabilities of active liquid crystals: Hybrid lattice Boltzmann simulations." In: *Physical Review E* 76.3 (Sept. 2007), p. 031921.

[79] Personal communication with Dr. A. Doostmohammadi, The Rudolf Peierls Centre for Theoretical Physics, University of Oxford. A paper describing the findings is currently under review. Jan. 2017.

[80] P. Rosen and D. S. Misfeldt. "Cell density determines epithelial migration in culture." en. In: *Proceedings of the National Academy of Sciences* 77.8 (Aug. 1980), pp. 4760–4763.

[81] Rizwan Farooqui and Gabriel Fenteany. "Multiple rows of cells behind an epithelial wound edge extend cryptic lamellipodia to collectively drive cell-sheet movement." en. In: *Journal of Cell Science* 118.1 (Jan. 2005), pp. 51–63.

[82] M. Reffay, L. Petitjean, S. Coscoy, E. Grasland-Mongrain, F. Amblard, A. Buguin, and P. Silberzan. "Orientation and Polarity in Collectively Migrating Cell Structures: Statics and Dynamics." In: *Biophysical Journal* 100.11 (June 2011), pp. 2566–2575.

[83] J. S. Lowengrub, H. B. Frieboes, F. Jin, Y.-L. Chuang, X. Li, P. Macklin, S. M. Wise, and V. Cristini. "Nonlinear modelling of cancer: bridging the gap between cells and tumours." en. In: *Nonlinearity* 23.1 (2010), R1.

[84] Paul Macklin, Steven McDougall, Alexander R. A. Anderson, Mark A. J. Chaplain, Vittorio Cristini, and John Lowengrub. "Multiscale modelling and nonlinear simulation of vascular tumour growth." en. In: *Journal of Mathematical Biology* 58.4-5 (Apr. 2009), pp. 765–798.

[85] Michael Fasolka and Anne Mayes. "Block Copolymer Thin Films: Physics and Applications." In: *Annual Review of Materials Research* 31.1 (2001), pp. 323–355.

[86] Christopher Harrison, Zhengdong Cheng, Srinivasan Sethuraman, David A Huse, Paul M Chaikin, Daniel A Vega, John M Sebastian, Richard A Register, and Douglas H Adamson. "Dynamics of pattern coarsening in a two-dimensional smectic system." In: *Physical review E* 66.1 (2002), p. 011706.

[87] Vincent Pelletier, Koji Asakawa, Mingshaw Wu, Douglas H. Adamson, Richard A. Register, and Paul M. Chaikin. "Aluminum nanowire polarizing grids: Fabrication and analysis." In: *Applied Physics Letters* 88.21 (May 2006), p. 211114.

[88] Young-Rae Hong, Koji Asakawa, Douglas H. Adamson, Paul M. Chaikin, and Richard A. Register. "Silicon nanowire grid polarizer for very deep ultraviolet fabricated from a shear-aligned diblock copolymer template." EN. In: *Optics Letters* 32.21 (Nov. 2007), pp. 3125–3127.

[89] T. Thurn-Albrecht, J. Schotter, G. A. Kästle, N. Emley, T. Shibauchi, L. Krusin-Elbaum, K. Guarini, C. T. Black, M. T. Tuominen, and T. P. Russell. "Ultrahigh-Density Nanowire Arrays Grown in Self-Assembled Diblock Copolymer Templates." en. In: *Science* 290.5499 (Dec. 2000), pp. 2126–2129.

[90] Miri Park, Christopher Harrison, Paul M. Chaikin, Richard A. Register, and Douglas H. Adamson. "Block Copolymer Lithography: Periodic Arrays of ~1011 Holes in 1 Square Centimeter." en. In: *Science* 276.5317 (May 1997), pp. 1401–1404.

[91] Katsuyuki Naito, Hiroyuki Hieda, Masatoshi Sakurai, Yoshiyuki Kamata, and Koji Asakawa. "2.5-inch disk patterned media prepared by an artificially assisted self-assembling method." In: *IEEE Transactions on Magnetics* 38.5 (2002), pp. 1949–1951.

[92] Gretchen A DeVries, Markus Brunnbauer, Ying Hu, Alicia M Jackson, Brenda Long, Brian T Neltner, Oktay Uzun, Benjamin H Wunsch, and Francesco Stellacci. "Divalent metal nanoparticles." In: *Science* 315.5810 (2007), pp. 358–361.

[93] David R. Nelson. "Toward a Tetravalent Chemistry of Colloids." In: *Nano Letters* 2.10 (Oct. 2002), pp. 1125–1129.

[94] Aldo D. Pezzutti, Leopoldo R. Gomez, and Daniel A. Vega. "Smectic block copolymer thin films on corrugated substrates." en. In: *Soft Matter* 11.14 (Mar. 2015), pp. 2866–2873.

[95] Andrew P Marencic and Richard A Register. "Controlling order in block copolymer thin films for nanopatterning applications." In: *Annual review of chemical and biomolecular engineering* 1 (2010), pp. 277–297.

[96] R. A. Segalman, H. Yokoyama, and E. J. Kramer. "Graphoepitaxy of Spherical Domain Block Copolymer Films." en. In: *Advanced Materials* 13.15 (Aug. 2001), pp. 1152–1155.

[97] J. Y. Cheng, C. A. Ross, E. L. Thomas, Henry I. Smith, and G. J. Vancso. "Fabrication of nanostructures with long-range order using block copolymer lithography." In: *Applied Physics Letters* 81.19 (Oct. 2002), pp. 3657–3659.

[98] D. E. Angelescu, J. H. Waller, D. H. Adamson, P. Deshpande, S. Y. Chou, R. A. Register, and P. M. Chaikin. "Macroscopic Orientation of Block Copolymer Cylinders in Single-Layer Films by Shearing." en. In: *Advanced Materials* 16.19 (Oct. 2004), pp. 1736–1740.

[99] TL Morkved, M Lu, AM Urbas, EE Ehrichs, et al. "Local control of microdomain orientation in diblock copolymer thin films with electric fields." In: *Science* 273.5277 (1996), p. 931.

[100] Jeffrey Bodycomb, Yoshinori Funaki, Kohtaro Kimishima, and Takeji Hashimoto. "Single-Grain Lamellar Microdomain from a Diblock Copolymer." In: *Macromolecules* 32.6 (Mar. 1999), pp. 2075–2077.

[101] Alexander Hexemer. "Order and disorder of block copolymers and particles on surfaces with topology." PhD thesis. University of California, Santa Barbara, 2006.

[102] Daniel A. Vega, Leopoldo R. Gómez, Aldo D. Pezzutti, Flavio Pardo, Paul M. Chaikin, and Richard A. Register. "Coupling between mean curvature and textures in block copolymer thin films deposited on curved substrates." en. In: *Soft Matter* 9.39 (2013), p. 9385.

[103] Christian D. Santangelo, Vincenzo Vitelli, Randall D. Kamien, and David R. Nelson. "Geometric Theory of Columnar Phases on Curved Substrates." In: *Physical Review Letters* 99.1 (July 2007), p. 017801.

[104] Randall D. Kamien, David R. Nelson, Christian D. Santangelo, and Vincenzo Vitelli. "Extrinsic curvature, geometric optics, and lamellar order on curved substrates." In: *Physical Review E* 80.5 (Nov. 2009), p. 051703.

[105] Elisabetta A. Matsumoto, Daniel A. Vega, Aldo D. Pezzutti, Nicolas A. Garcia, Paul M. Chaikin, and Richard A. Register. "Wrinkles and splay conspire to give positive disclinations negative curvature." en. In: *Proceedings of the National Academy of Sciences* 112.41 (Oct. 2015), pp. 12639–12644.

[106] S. A. Brazovskiĭ. "Phase transition of an isotropic system to a nonuniform state." In: *Soviet Journal of Experimental and Theoretical Physics* 41 (Jan. 1975), p. 85.

[107] K. Yamada and S. Komura. "The dynamics of order–order phase separation." en. In: *Journal of Physics: Condensed Matter* 20.15 (2008), p. 155107.

[108] S. Villain-Guillot and D. Andelman. "The lamellar-disorder interface: one-dimensional modulated profiles." en. In: *The European Physical Journal B - Condensed Matter and Complex Systems* 4.1 (July 1998), pp. 95–101.

[109] Liangshun Zhang, Liquan Wang, and Jiaping Lin. "Defect structures and ordering behaviours of diblock copolymers self-assembling on spherical substrates." en. In: *Soft Matter* 10.35 (June 2014), p. 6713.

[110] J. Swift and P. C. Hohenberg. "Hydrodynamic fluctuations at the convective instability." In: *Physical Review A* 15.1 (Jan. 1977), pp. 319–328.

[111] K. R. Elder, Mark Katakowski, Mikko Haataja, and Martin Grant. "Modeling Elasticity in Crystal Growth." In: *Physical Review Letters* 88.24 (June 2002), p. 245701.

[112] K. R. Elder and Martin Grant. "Modeling elastic and plastic deformations in nonequilibrium processing using phase field crystals." In: *Physical Review E* 70.5 (Nov. 2004), p. 051605.

[113] Heike Emmerich, Hartmut Löwen, Raphael Wittkowski, Thomas Gruhn, Gyula I Tóth, György Tegze, and László Gránásy. "Phase-field-crystal models for condensed matter dynamics on atomic length and diffusive time scales: an overview." In: *Advances in Physics* 61.6 (2012), pp. 665–743.

[114] Rainer Backofen, Axel Voigt, and Thomas Witkowski. "Particles on curved surfaces: A dynamic approach by a phase-field-crystal model." In: *Physical Review E* 81.2 (Feb. 2010), p. 025701.

[115] Teresa Lopez-Leon, Alberto Fernandez-Nieves, Maurizio Nobili, and Christophe Blanc. "Nematic-Smectic Transition in Spherical Shells." In: *Physical Review Letters* 106.24 (June 2011), p. 247802.

[116] Markus Deserno. *Notes on Differential Geometry - with special emphasis on surfaces in* $\mathbb{R}^3$. Available online. See chapter 3 on Variation of Surfaces. Department of Chemistry and Biochemistry UCLA (USA), 2004.

[117] Tanya L Chantawansri, August W Bosse, Alexander Hexemer, Hector D Ceniceros, Carlos J García-Cervera, Edward J Kramer, and Glenn H Fredrickson. "Self-consistent field theory simulations of block copolymer assembly on a sphere." In: *Physical Review E* 75.3 (2007), p. 031802.

[118] JF Li, J Fan, HD Zhang, F Qiu, P Tang, and YL Yang. "Self-assembled pattern formation of block copolymers on the surface of the sphere using self-consistent field theory." In: *The European Physical Journal E* 20.4 (2006), pp. 449–457.

[119] Jacob J Christensen and Alan J Bray. "Pattern dynamics of Rayleigh-Bénard convective rolls and weakly segregated diblock copolymers." In: *Physical Review E* 58.5 (1998), p. 5364.

[120] Leopoldo R Gómez and Daniel A Vega. "Relaxational dynamics of smectic phases on a curved substrate." In: *Physical Review E* 79.3 (2009), p. 031701.

[121] Mark Meyer, Mathieu Desbrun, Peter Schröder, and Alan H. Barr. "Discrete Differential-Geometry Operators for Triangulated 2-Manifolds." In: *Visualization and Mathematics III*. Ed. by Hans-Christian Hege and Konrad Polthier. Mathematics and Visualization. Springer Berlin Heidelberg, 2003, pp. 35–57.

[122] Gaetano Napoli and Luigi Vergori. "Extrinsic Curvature Effects on Nematic Shells." In: *Physical Review Letters* 108.20 (May 2012), p. 207803.

[123] Gaetano Napoli and Luigi Vergori. "Surface free energies for nematic shells." In: *Physical Review E* 85.6 (June 2012), p. 061701.

[124] Badel L Mbanga, Gregory M Grason, and Christian D Santangelo. "Frustrated order on extrinsic geometries." In: *Physical review letters* 108.1 (2012), p. 017801.

[125] Antonio Segatti, Michael Snarski, and Marco Veneroni. "Equilibrium configurations of nematic liquid crystals on a torus." In: *Physical Review E* 90.1 (2014), p. 012501.

[126] Thomas L. Wright, Dallas L. Peck, and Herbert R. Shaw. "Kilauea Lava Lakes: Natural Laboratories for Study of Cooling, Crystallization, and Differentiation of Basaltic Magma." en. In: *The Geophysics of the Pacific Ocean Basin and Its Margin*. Ed. by George H. Sutton, Murli H. Manghnani, Ralph Moberly, and Ethel U. Mcafee. American Geophysical Union, 1976, pp. 375–390.

[127] William Thielicke and Eize Stamhuis. "PIVlab – Towards User-friendly, Affordable and Accurate Digital Particle Image Velocimetry in MATLAB." en. In: *Journal of Open Research Software* 2.1 (Oct. 2014).

[128] Pierre Saramito. *Complex fluids - Modeling and Algorithms*. Vol. 79. Mathématiques et Applications. Springer International Publishing, 2016.

[129] Ronald G Larson. *Constitutive Equations for Polymer Melts and Solutions: Butterworths Series in Chemical Engineering*. Butterworth-Heinemann, 1988.

[130] S.M. Cox and P.C. Matthews. "Exponential Time Differencing for Stiff Systems." In: *Journal of Computational Physics* 176.2 (Mar. 2002), pp. 430–455.